The Dissertation Committee for Jesse Scott Aaron certifies that this is the approved version of the following dissertation:

Plasmon Resonance Coupling as a Tool for Detecting Epidermal Growth Factor Receptor Expression in Cancer

Committee:

Konstantin Sokolov, Supervisor

Rebecca Richards-Kortum, Co-Supervisor

Wolfgang Frey

Ann Gillenwater

Walter Hittelman

Plasmon Resonance Coupling as a Tool for Detecting Epidermal Growth Factor Receptor Expression in Cancer

by

Jesse Scott Aaron, B.S., M.S.E.

Dissertation

Presented to the Faculty of the Graduate School of

The University of Texas at Austin

in Partial Fulfillment

of the Requirements

for the Degree of

Doctor of Philosophy

The University of Texas at Austin

May 2007

Dedication

To my wife, Julie –

The normal superlatives for expressing my thanks to you do not seem adequate. Suffice it to say, much of the time and energy spent in my various academic pursuits really belongs to you. I will always owe you a debt of gratitude for your patience, understanding, support, and love.

Acknowledgements

There are several colleagues whose insight, discussion, and help have been instrumental in bringing to fruition the work contained in this dissertation. First and foremost, I would like to thank my Supervisor, Dr. Konstantin Sokolov. In addition to generous financial support, he has provided me with invaluable advice, inspiration, and an endless supply of encouragement and enthusiasm, without which the successful completion of my studies would have been absolutely impossible. Secondly, I would like to thank my Co-Supervisor, Dr. Rebecca Richards-Kortum, who remains a supreme personal and professional role model to nearly everyone she comes in contact with (myself included). Her ideas, guidance, as well as generous support, both moral and otherwise, have always been appreciated and will not soon be forgotten. In addition I would like to thank the NSF IGERT program for generous financial support during my studies, as well as an opportunity to interact with a wide range of students and investigators. Also, to all of the former and current members of the Optical Spectroscopy and Imaging Lab, thank you for your support, advice, criticism, spirited discussion, late nights, early mornings, and general fun that permeated our time working together.

Finally, I would like to give my sincerest thanks to my parents, who imbued me with the good sense to never take yourself too seriously and to always "follow your bliss"…

Plasmon Resonance Coupling as a Tool for Detecting Epidermal Growth Factor Receptor Expression in Cancer

Publication No._____

Jesse Scott Aaron, Ph.D.

The University of Texas at Austin, 2007

Supervisor: Konstantin Sokolov

Co-Supervisor: Rebecca Richards-Kortum

Optical molecular imaging has burgeoned into a major field within biomedicine, and technologies that incorporate surface plasmon resonance effects have become a major focus within this field. Plasmon resonance has been defined as the collective oscillation of the conduction band electrons in certain metals (such as gold) in response to an electric field, such as an impinging wave of light. We show that elastic light scattering due to the plasmon resonance of nanometer-sized gold particles makes them powerful tools for optical imaging of epidermal growth factor receptor (EGFR) expression – a major biomarker for carcinogenesis. Optical technologies in general are poised as cheap, flexible ways to aid in diagnosis and treatment of disease. In addition to supplying a bright, stable optical scattering signal and a convenient conjugation platform for targeting molecules, these materials display a unique behavior termed "plasmon coupling". This term refers to the dramatic optical property changes brought about by the presence of other nearby nanoparticles. These changes include a dramatic red-shifting in their peak plasmon resonance wavelength, as well as a non-linear, *per-particle* increase in the overall scattered power. We show that such conditions exist in cells and are primarily due to intricate protein trafficking mechanisms as part of the EGFR life-cycle. The observed variations in

plasmon coupling can give clues as to the nanoscale organization of these important proteins. In addition, the resulting optical property changes result in a large, molecular-specific contrast enhancement due to the shifting of the resonance closer to the near infrared region, where biological tissues tend to be most transparent. Despite this enhancement, however, many tissues contain large endogenous signals, as well as barriers to delivery of both light and the nanoparticles. As such, we also show an example of a multifaceted approach for further increasing the apparent molecular-specific optical signals in imaging of EGFR expression by using an oscillating magnetic field. This serves to encode the signal from magnetically susceptible plasmonic nanoparticles, making their extraction from the background possible. Overall, the studies presented in this dissertation should serve to stimulate further investigations into a wide variety of technologies, techniques, and applications.

TABLE OF CONTENTS

LIST OF TABLES

LIST OF FIGURES

CHAPTER 1:

Introduction

1.1 THE AGE OF MOLECULAR MEDICINE

Historically, the method by which most physicians detected and treated disease was based on macroscopic observables of the patient's condition and his/her response to therapy. With the advent of microscopic techniques in medicine by Malpighi [2], Hooke [3], and Leeuwenhoek [4], the gradual adoption of adjuvant imaging systems in medical practice progressed. Through succeeding decades, the use of microscopy in medicine required resection of tissue from a patient for staining and examination in a compound-type microscope, and this is still standard practice for many diseases that must be identified histologically [5]. Throughout the 19^{th} and 20^{th} centuries, however, technologies such as X-ray imaging, computed tomography (CT), Ultrasound, positron emission tomography (PET) and magnetic resonance imaging (MRI) vastly expanded the repertoire of imaging methods used in medical practice, and allowed for an *in-vivo* evaluation of the patient, often with relatively good spatial and/or temporal resolutions [6] that allow for high confidence in predicting disease. Yet, the majority of information typically gleaned from current modalities (with notable exceptions such as fMRI and PET) remains *anatomical*. That is, the images are of tissue micro-structure and architecture, and do not necessarily contain detailed information about the genetic or proteomic makeup of the tissue. While structural information can be very useful, it may not directly relate to that tissue's *function*. Or, in the case of a pathophysiological condition, the anatomic manifestation of a functional abnormality may not appear until successful treatment has become considerably less likely. This is particularly true in the

case of cancerous or neoplastic lesions, where molecular changes usually precede anatomic abnormalities [7]. Because of this, the early detection and treatment of carcinogenesis remains an excellent strategy for prolonged survival.

Concomitantly with advances in *in-vivo* medical imaging techniques, molecular biological investigations throughout the latter half of the 20th century began to shed light onto the underlying molecular mechanisms responsible for many pathogenesis processes, particularly carcinogenesis [7]. Indeed, entire metabolic, catabolic, and signaling cascades have been elucidated with the aid of bioanalytical methods. This has led to a molecular characterization of many cancerous diseases and has resulted in a greater understanding of their molecular underpinnings and the resulting anatomical abnormalities normally observed by a physician or pathologist. Although the fields of medical imaging and molecular biology have made great strides in the last 50 years, the synthesis of these two disciplines is still in its infancy. However, the promises of success are attractive so say the least. Currently, there is, to a large degree, a disconnect remaining between minimally invasive imaging and molecular characterization of cancer. On the one hand, the presence of a myriad of biological markers can be ascertained from a patient, but only after removal of the diseased tissue and subsequent staining and microscopic examination [5]. This presents two problems: the removal of diseased tissue requires an invasive procedure, whose risks may not be negligible, depending on the organ site [8]. Second, the removal of a neoplastic growth implies that it can be detected, usually nested among normal tissue – a fact that may indicate that the disease has already progressed to a dangerously advanced state. Alternatively, the taking of biopsies before disease is visually apparent becomes a random point-sampling procedure that only has a

certain statistical chance of detecting cancer. On the other hand, conventional medical imaging can allow for rapid screening of a patient over a relatively large tissue volume. However, the molecular information currently available from such modalities is still rather limited, although emerging technology has begun to allow some molecular imaging in MRI [9-11], PET/CT [12-15], and ultrasound [16-20]. A persistent problem still exists, in that all of these techniques also have relatively limited spatial resolution [6], typically not sufficient to resolve very small lesions at a point where they are the most curable. As such, new paradigms may be needed to fully integrate the vast network of knowledge built up from the last 50 years of molecular biological investigation with the promising technical advances utilized in biomedical imaging.

1.2 NANOTECHNOLOGY AND BIOMEDICAL APPLICATIONS

In 1960, the celebrated physicist Richard P. Feynman was quoted as saying, "The problems of chemistry and biology can be greatly helped if our ability to see what we are doing, and to do things on an atomic level, is ultimately developed – a development which I think cannot be avoided." These sentiments underscored widely attended lectures by Feynman, entitled "*There's Plenty of Room at the Bottom*", in which he implored for the need to develop systems, techniques, or platforms that can interact on atomic/molecular level – i.e. the *nanoscale* [21]. Feynman seemed to sense the need for materials that could sense and report events happening far below the limits of human perception. Interrogation of endogenous sources of signal (whether it be via photonic excitation or otherwise) has great value, although it retains some limitations. Generally, the optical signature of most biomolecules is not specific enough to identify particular species, or, though specific, exists within the tissue milieu such that positive

identification remains difficult. A better overall strategy might be to access and intervene in the molecular world of living cells and their machinery using similarly-sized externally introduced materials. This scheme may be preferable whether the purpose is to merely "report" the presence or location of a particular molecular, or to "intervene" – i.e. to therapeutically change a particular process within the cell. While the exact size range of what constitutes the "nanoscale" is not clearly defined, perhaps a relatively forgiving range would be from 1-1000nm. A stricter definition might only include structures 10-100nm, historically named the *mesoscale* – literally, length scales *in the middle* – describing size ranges that are not always representative of the bulk material, but cannot be treated as single atoms either. This is the length range where quantum physics starts to become bulky, while classical physics cannot always be applicable. Materials of this length scale encompass a large range of technologies, whose application may be diagnostic, therapeutic, or both. Table 1.1, adapted from [21] , attempts to collect some examples of nanotechnology currently under development for biomedical applications, and represents a selected sampling of some of the more popular directions. Clearly, the overall field of bionanotechnology is growing rapidly, and the purview of applications is broadening at an equal rate. This ranges from experimental diagnostics, in the case of quantum dots [22-24], to therapeutic carriers [25-28], to therapeutic agents [29] to multifunctional agents that can both sense and treat, [30-35]. As stated above, nanomaterials are advantageous due to the comparable size scale as the biomolecules they interact with. In addition, a good nanotechnology platform should retain a large amount of flexibility in terms of its application, as well as be mass producible. At the

current stage, no single technology represents a panacea for cancer diagnostics or treatment.

Table 1.1. Selected Examples of nanotechnology in biomedical applications

Technology	Typical Size	Application(s)
Quantum Dots	1-10nm	Fluorescence-based molecular imaging, both *in-vitro* and *in-vivo* [22-24]
Plasmonic Nanoparticles	15-200nm	Reflectance-based molecular imaging, photothermal ablation of cells [30-35]
Magnetic Iron Oxide Nanoparticles (SPIO)	5-10nm	MRI contrast agents, often used to image blood flow and atherosclerotic plaques [36-42]
Nanodiamond	60-100nm	NIR fluorescence from NV^- defects, for use in fluorescence imaging [43-45]
Fullerene (C_{60})	2-20nm	Antioxidant [29]
Carbon nanotubes	1-100nm diam., 20-1000nm long	Fluorescent sensor [46-48], NIR Photoablation [49, 50]
Porous Silica	10-1000nm	Drug delivery [25-28]

1.3 OPTICAL TECHNOLOGY, NANOPARTICLES AND MEDICAL IMAGING

As shown in Table 1.1, there are a multitude of nano-scale technologies currently under development for biological/medical application. Of note is the fact that many of these technologies rely on an optical component for activation or interrogation. Quantum dots, nanoshells, nanorods, nanodiamond, carbon nanotubes, as well as porous silica are all optically active, reflecting the fact that optical-based technologies have become popular as possible cancer diagnostic aids and interventions. The reasons for this are multitude, and will be dealt with in more depth later. Briefly, however, optical methods are relatively cheap, as compared to MRI, CT, or even ultrasound [51]. Secondly, the practically achieved resolution limit of optical technologies is in the hundreds of nanometers to micron range. MRI, CT and ultrasound all fall within the hundreds of microns to millimeter range in medical practice [6]. The resolution improvement

available with optical technology makes identifying small lesions much easier, providing an inexpensive way to effectively screen, intervene, and monitor treatment. Optical techniques may also be used to provide visual cues during surgery, particularly via functional molecular imaging.

The ability to accurately visualize the three-dimensional tissue architecture is absolutely critical. MRI, CT, and ultrasound all have the ability to represent the imaging volume in a 3D manner. Optical imaging, too, can achieve this through the implementation of some type of "gating" or "sectioning" mechanism that rejects out-of-focus light. This is a relatively new development in optical imaging, one that recognizes the need to move beyond 2D imaging available with traditional optical microscopes. To date, there are two popular strategies for achieving this "gating" principle, while maintaining high resolution. The first to be developed physically blocks the out-of-focus light from entering the detection path of the microscope by placing an aperture at the conjugate image plane on the far side of the microscope's object lens. This is the so-called confocal principle that was proposed by Minsky in the 1950s [52]. The second main sectioning strategy is via the use of coherence gating, which spawned the invention of optical coherence tomography (OCT). This setup uses an interferometer to induce constructive interference at the conjugate image plane, thereby creating an optical sectioning effect this way [53]. In either case, the depth at which optical or near infrared photons can penetrate human tissues does not generally exceed the millimeter range [54]. It is important to note that there are also diffuse optical tomographic imaging techniques that are able to resolve optical signals in three-dimensions. However, resolution using these techniques is much larger that either confocal or OCT microscopies [55].

From this initial discussion, it can be seen that the combination of optical and nanoscale technologies may prove to be a powerful approach to solving certain biomedical problems, particularly detection of tumorigenesis that occurs in superficial tissues. Of the technologies listed in Table 1.1, the current two most popular strategies (as evidenced by number of publications) are molecular-specific fluorescence imaging using semiconductor quantum dots (qdots) and imaging using scattering/absorption from plasmonic nanoparticles (which include nanoshells, nanorods, spherical nanoparticles and all variations within). Both of these technologies have complementary features, and the best particular solution may remain application-dependent. On the one hand, quantum dots, in general, have a narrower emission profile, as compared to the plasmon resonance of gold nanoparticles, which makes them arguably more suitable for multiplexing applications by altering size and composition [24, 56-59]. However, they are also comprised of highly toxic components [60-62], and do suffer from photobleaching (albeit at a much lower rate than traditional fluorescent dyes) [23]. Plasmonic nanoparticles are also spectrally tunable (that is, their peak plasmon wavelength can be altered by changing the constituent material and geometry), but their plasmon resonance peak is usually wider than the emission peak of qdots [30, 63]. Plasmonic particles are, however, comprised of less toxic noble metals (gold and silver), with or without combinations of a dielectric material [30, 64]. Gold-based nanoparticles, in particular, have been shown to be non-cytotoxic, even at high dosage [65], and have been used as therapeutic carriers in one study with human subjects, with no reports of adverse effects due to the gold [66]. In addition, gold/silver nanoparticles have a greatly simplified conjugation strategy associated with them, as organo-gold interfacing chemistries are quite well characterized

via years of use as electron microscopy stains [67, 68], although conjugation strategies for qdots are also widely available [24, 59, 69]. Plasmonic particles, however, have higher optical cross-sections than qdots [70], do not photobleach [63], and display a very interesting phenomenon of "plasmon coupling", whereby their optical properties shift in response to the presence of other resonant scatterers in the near field [71-74]. This phenomenon does not have a clear analog in other modalities, although the FRET concept is somewhat similar in application [75], with several important drawbacks.

As will be explained further, plasmon coupling acts as a means by which molecular trafficking and interactions can be monitored, as well as a mechanism by which greatly increased optical signal and contrast is possible. It is this phenomenon which will act as the undercurrent for most of the work contained in this dissertation. The other unifying concept will be the use of epidermal growth factor receptor (EGFR) as a biomarker for carcinogenesis. As will be discussed further, this is a well characterized membrane-bound receptor [76], and has been the object of several recent molecular imaging studies using both plasmonic particles [77-81] and qdots [82-85].

1.4 OUTLINE OF SPECIFIC AIMS

The aims of this dissertation will provide insight into molecular imaging of EGFR using plasmonic particles and to explore the phenomenon of plasmon coupling with the intension of exploiting it to gain information that may not be attainable using other optical/nanotechnology methods. These studies were carried out in progressively more complex biological models. In addition, further studies will be shown that point to the utility of using hybrid nanoparticles and a multi-faceted approach to help further improve molecular-specific contrast. To that end, the four aims of this dissertation are as follows:

1. First, we study and characterize the phenomenon of plasmon resonance coupling in cell suspensions labeled with spherical gold nanoparticles targeted for EGFR expression. This work establishes some basic principles needed to evaluate the level of contrast enhancement that is possible, and to what degree plasmon coupling plays a role. It will be shown that plasmon coupling is centrally responsible for highly increased optical contrast when imaging epidermal growth factor receptor (EGFR) expression, as compared to normal or non-expressing samples, in the near-infrared region. This is due to the marked red-shifting of the plasmon resonance upon particle binding to cells, as well as a non-linear relationship between particle concentration on/in the cells and the overall scattering signal.
2. Second, the relationship between the plasmon coupling effect and the nanoscale arrangement of EGFR will be investigated. These studies focus on the labeling dynamics and EGFR trafficking patterns within living cells. It will be shown that gold nanoparticles are sensitive to the nanoscale arrangement of EGFR molecules both on the surface of the cell, as well as after endocytosis. We will show a progressive red-shifting of the plasmon resonance as gold nanoparticle-labeled EGFR molecules collect on the cell surface and internalize into endosomal (and later lysosomal) compartments, consistent with currently held mechanistic models. These observations are independently confirmed through electron microscopy and are evaluated quantitatively using hyperspectral imaging.
3. The principles developed in aims 1 and 2 can then be used to help explain labeling patterns seen in more complex biological models in an effort to further

evaluate gold nanoparticles' appropriateness as a means for early cancer detection. Aim 3 serves to extend the applicability of immuno-targeted gold nanoparticles from single cell suspensions to homogeneous and heterogeneous three-dimensional synthetic tissue constructs to *ex-vivo* human cervical tissue and animal xenografts, as well as to an *in-vivo* animal model. We will show that normal to abnormal signal ratio is higher than what would be expected using linearly behaving reporters. That is, we show signal enhancement in a variety of biological models far above the factor of EGFR over-expression. This is important in the case of molecules (such as EGFR) that are not necessarily *uniquely* expressed in neoplastic tissue, but experience *increased* expression, or modulate their nanoscale arrangement. Further, we show preliminary data to support the use of gold nanoparticles as a means to detect micrometastases in sentinel lymph nodes in oral cavity carcinoma.

4. Finally, a study is shown that indicates how hybrid plasmonic nanoparticles can be used to further increase optical contrast in EGFR imaging. Through the use of iron oxide/gold hybrid nanoparticles in an oscillating magnetic field, the molecular-specific signal can be modulated with a user-defined frequency. By capturing the time-varying signal, and applying simple Fourier-based filtering algorithms, the specific to non-specific signal ratio can be increased a further 3-4 fold over unlabeled cells, or those labeled pure-gold particles alone. We believe this study opens up further opportunities in multi-modal cellular monitoring and possible mechanical actuation of signaling cascades that are implicated in cancer and other diseases.

CHAPTER 2:

Background

2.1 MOTIVATION: CANCER STATISTICS

While optical molecular imaging with gold nanoparticles may be applicable in a number of health-related areas, the problem of cancer remains a formidable one that deserves application. The myriad of disease states that fall under the general category of "cancer" represent a staggering worldwide cost both in terms of material resources and human lives. Worldwide, more than 6 million people die from cancer each year and more than 10 million new cases are detected. In most developed countries, cancer is the second leading cause of death, behind only cardiovascular disease [1]. As figure 2.1 indicates, while the death rates due to many serious health threats such as heart disease, stroke, and respiratory infection have been dramatically reduced in the US over the past 50 years, the death rate due to cancer remains essentially unchanged.

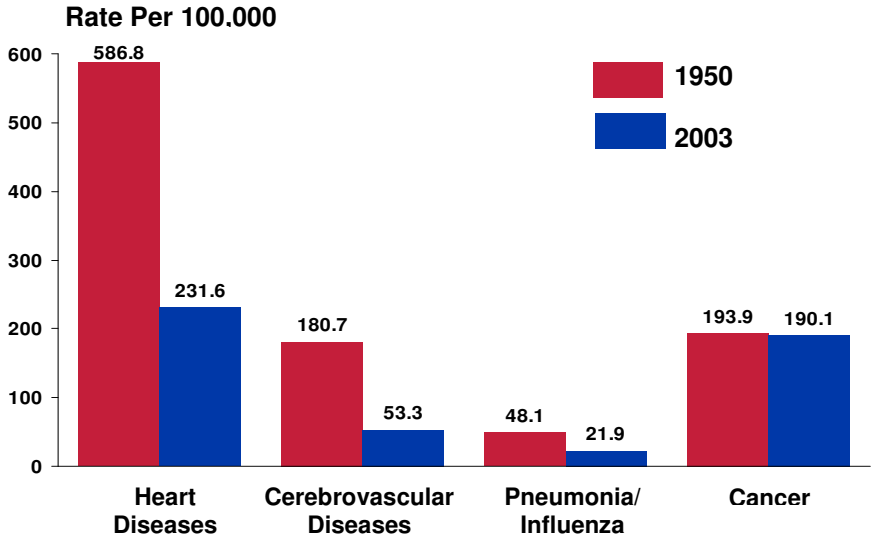

Figure 2.1 Death rate changes between 1950 and 2003 for the four leading causes of death. Note the large decreases, except from cancer. From [1]

The overall cancer survival rate in the US is about 65% - that is, nearly 2 in 5 cases of cancer are fatal [1]. It is also important to note that 85% of all malignant growths begin in the epithelial lining of organs such as lung, cervix, oral cavity, skin, colon, etc [86]. This is significant, as it points out that most cancers are initially superficial diseases, and can often be treated successfully when identified at this early stage. For example, the Pap smear for cervical cancer is considered one of the most successful implementations of such early screening strategies. Between 1955 and 1992, the number of deaths from cervical cancer declined by 74% in the United State [87]. Conversely, lesions in the oral cavity typically have a lower overall survival rate, due to the lack of widespread screening techniques in the US, which result in the lesions generally being detected at a much later stage. This leads to treatments that are more difficult, more expensive, and less successful. Overall five-year-survival rates for patients with advanced stage disease remain at 30-40% or less [1].

2.2 THE MOLECULAR CHARACTERISTICS OF CANCER

There are several widely-accepted features that most or all cancerous growths have in common, and have been put forth by Hanahan and Weinberg [7]. These include: (1) the ability to evade apoptosis, (2) sustained angiogenesis, (3) limitless replicative potential, (4) ability to invade and metastasize, and (5) insensitivity to growth regulatory signals. There are numerous specific proteomic and genomic biomarkers for each of these characteristics. For example, apoptosis is a critical process by which abnormal cell functioning is detected and results in programmed cell death. Both the insulin-like growth factor receptor (IGFR) [88] and receptors for transforming growth factor [89]

proteins modulate this process, and abnormalities in either of these biomarkers can result in abnormal cells being allowed to continue to live and replicate. Telomerase proteins are often responsible for the ability of cancer cells to replicate themselves indefinitely by maintaining telomere length during mitosis [90]. For a tumor to survive past the initial stages, it must be able to recruit blood vessels into its volume, and molecules such as vascular endothelial growth factor VEGF receptor can cause the growth of new capillaries in order to sustain the abnormal tissue [91]. Perhaps the most dangerous feature, metastasis, is regulated by numerous proteins, chief among them the metallomatrix protease (MMP) family (especially MMP-2 and -9) [92-94]. These enzymes catalyze the destruction of connective tissue within the epithelial stroma, allowing cells to enter the underlying vasculature or lymphatic tissue in order to spread to distant organ sites.

Of the five aforementioned characteristics, the insensitivity to growth regulatory signals was the first to be identified by molecular biologists and oncologists, and hence has the most complete literature treatment. This ability refers to the tendency of most cancer cells to either maintain a high growth rate despite low extracellular growth factor concentrations (through alterations in homeostasis), despite high amounts of anti-growth signaling molecules, or both. There are three main compartments in which this ability can rise (often simultaneously). The first is at the stage of growth factor production. For most cells in the body, growth factor signals are produced by other cells – termed heterotypic signaling [7]. Some cancer cells, however, attain the ability to synthesize their own growth factors, which can produce a positive feedback loop, or "autocrine" pattern in the cells' growth circuitry. A second point of disfunction can exist at the level

of effector molecules inside the cell. Disfunctions arising within the internal circuitry of a cell's transcription factor regulation pathways can cause a host of abnormalities resulting in insensitivity to signaling cascades. The protein p16 is a classic example [95].

The third compartment, and one of the first to be discovered, is at the growth factor receptor level. It is here that the growth factor signal is transduced to the effector molecules that initiate DNA synthesis, mitosis, and other processes. The growth factor receptor stage represents a logical starting point for optical molecular imaging. First, it is one of the most studied areas in molecular oncology, and thus its biology is relatively well-understood. Second, its presence on the cell surface represents an ideal area to target: unlike growth factors, receptor molecules are located (though often transiently) on the cell membrane. As such, cells that up-regulate or disregulate these molecules are relatively easy to recognize in an imaging scheme. Also, unlike the internal effector molecules, imaging labels need not be functionalized with additional cell membrane-entry or disrupting factors to permit introduction into the cell.

2.3 THE EPIDERMAL GROWTH FACTOR RECEPTOR (EGFR) FAMILY

Although there is a multitude of growth factor receptors, the epidermal growth factor receptor (EGFR) is perhaps the most studied receptor of its type [76, 96-106]. It has been placed within the erbB receptor family, (and is sometimes referred to as erbB-1), whose family consists of at least three other similarly structured receptor tyrosine kinases (together often named erbB-1 through -4), with various ligand specificities. These proteins are also often referred to in breast cancer contexts as belonging to the HER protein family (whereby each member is referred to as HER-1, HER-2, etc. [107]). For

the sake of clarity, EGFR will be referred to as belonging to the erbB family in this dissertation.

The erbB family represents the external to internal signal transduction point for many cellular processes, including proliferation, survival, migration, and differentiation [108]. Each of the four known erbB receptors has an extra-cellular portion, a single trans-membrane domain, and a cytoplasmic portion. Defining characteristic of all the erbB proteins include dimerization-dependent activation (either homo-dimerization [109], or hetero-dimerization [110]), usually with a 2:2 ligand:receptor stoichiometry (with the notable exception of erbB-2, which has no known ligand [110]). For a summary of the ligand specificities for each of the erbB receptors, refer to table 2.1, adapted from [111].

Table 2.1 Summary of each erbB member and known ligands, summarized from [111].

erbB Member	Known Ligands
erbB-1 (EGFR)	Epidermal growth factor (EGF), transforming growth factor α (TGF-α), amphiregulin, betacellulin, heparin-binding EGF, epiregulin
erbB-2	None
erbB-3	Neuregulin 1 and 2
erbB-4	Neuregulin 1-4, betacellulin, heparin-binding EGF, epiregulin, tomogregulin

Ligand binding and dimerization elicits cross-phosphorylation of various tyrosine residues on the cytoplasmic domains of both receptors. This allows binding of effector molecules including the MEK/MAPK cascade [112] , SoS [113], Ras [114], Grb2[114] and others [115-117], eliciting DNA transcription, and other results as described above.

This dissertation will focus primarily on imaging of the first member of the erbB family – erbB-1 or EGFR. The 175kD EGFR protein was first recognized as a possible receptor in fibroblast cells in 1973 by Hollenberg and Cuatrecasas [118], and later positively identified [119]. In subsequent studies, the structure [120], biophysical

properties [121, 122], as well as possible stimulating and inhibitory mechanisms [123-126] begun to be elucidated. Early on, it was recognized that EGFR molecules tended to cluster on the cell surface [127-131]. It was not until later that dimerization was found to be the activation "quanta" of this particular protein [132, 133], accompanied by higher-order aggregation in clathrin-coated pits on the cell surface [134-136]. It is this aggregation that forms the precursor of EGFR endocytosis and internalization in response to ligand binding, and represents a vital regulatory mechanism of EGFR signaling [97, 135, 137, 138]. The processing of internalized EGFR molecules is still an active area of research. Many basic internalization and processing mechanisms have been elucidated [139, 140], although a more nuanced view of the model is currently being developed. The basic mechanistic view postulates that upon ligand binding, dimerization, aggregation in clathrin-coated pits, and internalization, EGFR receptors are trafficked through the endocytotic pathway via microtubule-directed motion [135, 141] and tagged with the sorting/degradation marker ubiquitin before destruction in lysosomes. Of great interest currently is the hypothesis of EGFR "recycling" – that is, the tendency of some cells to reuse EGFR receptors by bypassing the lysosomal degradation pathway and up-regulating the re-fusion of EGFR-laden vesicles back into the plasma membrane. Though a number of studies have detected this effect indirectly [136, 142], this behavior seems to have been observed only in one limited study [143] based on fluorescence quenching of labeled EGFR molecules upon internalization.

2.4 OPTICAL IMAGING OF BIOLOGICAL TISSUE

This rich, well characterized network of downstream effectors, as well as elegant and nuanced regulatory mechanisms makes EGFR a fertile area to begin studying using

plasmonic nanoparticles. Using optical phenomena for this type of detection, however, begs the questions as to whether this type of technology could effectively be implemented in a clinical setting. As described previously, optical technologies are most adept at detection of *epithelial* cancers – which account for approximately 85% neoplastic growths seen in the clinic [1]. This is due to the fact that such lesions exist less than 1 mm from the organ surface, which can potentially be accessed by endoscopic probes [144]. Optical or near-infrared wavelength illumination can easily penetrate these thicknesses to reveal morphologic and/or chemical change [145-148]. This is advantageous because optical technologies are comparatively cheaper than most other imaging modalities such as MRI or CT, while at the same time allowing for resolutions down to sub-cellular levels *in-situ,* without the use of ionizing radiation. Light-based technologies such as optical coherence tomography (OCT) and confocal microscopy have shown the ability to diagnose early cancerous growths *in-vivo* with specificities and sensitivities that meet or exceed current clinical practices. For example, Collier et al. were able to distinguish high-grade cervical intra-epithelial lesions (those with a high probability for progression) from normal and low grade cases (those with a low probability for progression), with a sensitivity and specificity that exceeds that of the Pap smear [149]. The diagnostic parameters were based on cell nuclear morphometric measurements such as the nuclear to cytoplasmic ratio and average nuclear area. These features are currently clinically measured via costly and time-consuming histological analysis. This study indicated that, consistent with histological examinations, the average nuclear size and shape distribution increases markedly as pre-cancerous changes progress. In a pilot clinical study, the diagnostic performance of this technology was

evaluated against a conventional histopathologic diagnosis, and produced a sensitivity of 100% and specificity of 91% in detection of severe dysplasias. This is encouraging, when compared to the current clinical paradigm of Pap smear screening and colposcopic diagnosis, which have substantially lower overall specificities and only comparable sensitivities [150]. Similarly encouraging results have been attained using optical coherence tomography (OCT) in a variety of organ sites [147, 151], indicating that statistically significant signal intensity changes can accurately predict pathological changes. While the sources for these changes can be varied, in the case of epithelial cancers, the increase in signal seen with neoplastic changes seems to be due in large part to carcinogenesis-mediated increases in cell nucleus size, as well as nuclear texture and shape irregularities, as suggested by a number of studies [146, 152].

While the above examples indicates the level of information attainable using reflectance or scattering-based modalities, fluorescence confocal imaging and spectroscopic techniques can also provide valuable, clinically relevant information for a variety of diseases, including cancer [153-158]. In contrast to reflectance-based techniques, which derive signal sources from refractive index mismatches arising from cell nuclei and other microanatomical features [159], fluorescence based techniques derive their signals from specific chemical components within cells and connective tissues. There have been numerous fluorophors identified that are commonly present in living tissues [160-162], including several flavinoids, particularly the electron carrier FAD^+ [154], as well as NADH [160], porphyrins [163], as well as the formation of complex fiber cross-links in connective tissues, especially collagen [158]. In particular, the electron carriers FAD^+ and NADH have been shown to be positively correlated with

dysplastic state, while collagen-based fluorescence seems to be negatively correlated with disease [164].

Despite the multitude of promising results using endogenous sources of optical contrast in tissues, the number of chemical species that can be potentially identified using either scattering or fluorescence techniques is limited. More specificity can potentially be attained through the detection of endogenous Raman-type scattering from tissues [165, 166], due to the chemical sensitivity of this method. A lack of signal strength, however, as well as the highly complex mixture of thousands of chemical species in typical biological tissue seems to hinder this approach somewhat for identification of specific cancer-causing proteins, and rather seem to favor utilizing net differences in overall signals from healthy and diseased tissue.

2.5 MOLECULAR IMAGING: FLUORESCENT CONTRAST AGENTS

As an alternative to probing for endogenous sources of optical signal, another method may involve using *externally* derived optically active compounds that can be exposed to tissues in order to gain molecular specificity. Such materials are often termed "contrast agents". Organic fluorescent dyes are traditional contrast enhancing molecules for in vitro and in vivo optical imaging [167-170], and are widely used in many biological/biomedical investigations to determine expression level and localization of biomarkers, particularly in drug development [171], albeit often using fixed samples (although live cell molecular imaging is becoming more widespread [172-175]). Fluorescent dyes have been developed that exhibit increased photostability [176], as well as functional sensitivity to pH [177], membrane potential [178], or a particular ion such as Ca^{2+} [179], among other factors.

Recent advances, particularly in materials science, have also led to the development of semiconductor quantum dots [23, 60, 180-182]. Quantum dots have gained much popularity over the past 8-10 years after their initial report as effective biological imaging agents [23]. These 2-10nm diameter agents are comprised of semiconductor materials that (due to their small size) display a quantum confinement phenomenon, thereby creating a well-defined energy level band gap that can be exploited to produce luminescence with high quantum efficiency, narrow spectral bandwidth, and relatively increased photostability [22, 183]. Because of this, there has been widespread recognition that quantum dots provide a flexible platform for optical molecular imaging. However, there are some problematic issues with this technology. First, although quantum dots are more resistant to photobleaching than organic dyes, their signal does still degrade somewhat over time [23]. Further, they display a so-called "blinking" effect – discrete "on" and "off" states that could making their use in very sensitive assays questionable [184]. Most troubling, however, is the fact that quantum dots are typically synthesized using highly toxic metal/semiconductor materials. To date, relatively little work has been done in evaluating the possible biocompatibility issues surrounding this technology [62].

Beyond this, there is emerging realization that simply imaging the expression and location of a biomarker may not provide enough information to fully impact clinical practice. *Functional* molecular imaging is a term that could refer to the ability to image the presence, localization, and *behavior* of a proteomic biomarker on the molecular scale. Two main strategies have been developed, which are related, to gain this type of information though an optical imaging approach. By far the most popular is the

fluorescence resonance energy transfer (FRET) technique [75], which utilizes a pair of fluorophors; one fluorophor acts as a "donor", while the other acts as a "acceptor". The simplified mechanism is as follows: The donor is excited at near its optimal wavelength, whereby its relevant electrons are excited. If the proximity of the acceptor fluorophor is sufficient, a certain percentage of the energy contained in the donor's excited state electrons is non-radiatively transferred to the acceptor dye. Thus, the acceptor is indirectly excited, and emits luminescence only in close proximity to its donor fluorophor. While this technique has proved eminently useful, there are still drawbacks. First, the donor and acceptor fluorophors must have overlapping absorption/emission spectra – representing a limited number of fluorophor pairs. This also implies that the traditional FRET technique can only quantitatively detect co-localization of *two recognizably distinct* populations of molecules – and will not be easily applicable for situations such as EGFR homodimerization, which represents the association of two *identical* molecules. From a more technical point of view, FRET also suffers from relatively low energy transfer efficiencies that depend on the *sixth-power* of the donor-acceptor separation distance, typically less than 10nm [185], as well as a careful alignment of the donor-acceptor dipoles for stable energy transfer.

A second main strategy, although not as fully utilized as of yet, allows the probing of a single enzyme's function via energy transfer – not unlike FRET – but utilizes a fluorescent/quencher pair of moieties that are synthesized in the "off" state – that is, the fluorescent moiety is in close vicinity (less than 10nm) to a quenching material (i.e. prevents fluorescence) through a linker that has bioreactivity to the enzyme of interest. So far, this concept has elicited a number of interesting techniques that attempt to

selectively image the enzymatic activity of proteolytic enzymes, which are a critical component of a cancer cell's ability to extricate itself from its tissue of origin and to invade distant organ sites. Upon exposure to the enzyme, this linker is hydrolytically cleaved, thus releasing the fluorophor from proximity to the quencher, and allowing normal luminescence to occur under proper optical excitation. Such a strategy has incorporated organic fluorophors as both the emitter and quencher [170, 186], as well as quantum dots as the emitter [187]. These technologies have proven to provide interesting insights into the proteolytic behavior of cells, but their application to other proteomic studies seems limited. Of particular interest would be to optically image the nanoscale, long-term behavior of one or more of the innumerable *regulatory* proteins that control vital cell functions, and whose dysfunction can result in a diseased state.

2.6 PLASMONIC NANOPARTICLE CONTRAST AGENTS

2.6.1 Observations of Optical Properties

As early as 1857, Michael Faraday recognized the unique interactions between nanometer sized gold particles and light [188]. These interactions revolve around the excitation of conduction band electrons, called the surface plasmon. Mathematically, a plasmon resonance corresponds to a resonant scattering phenomenon whereby the real part of the dielectric function of the metal is negative and its magnitude is greater than that of the surrounding media. Figure 2.2 shows the total extinction spectra of 25 nm gold nanoparticles in aqueous solution, with a sharp plasmon peak at approximately 525 nm.

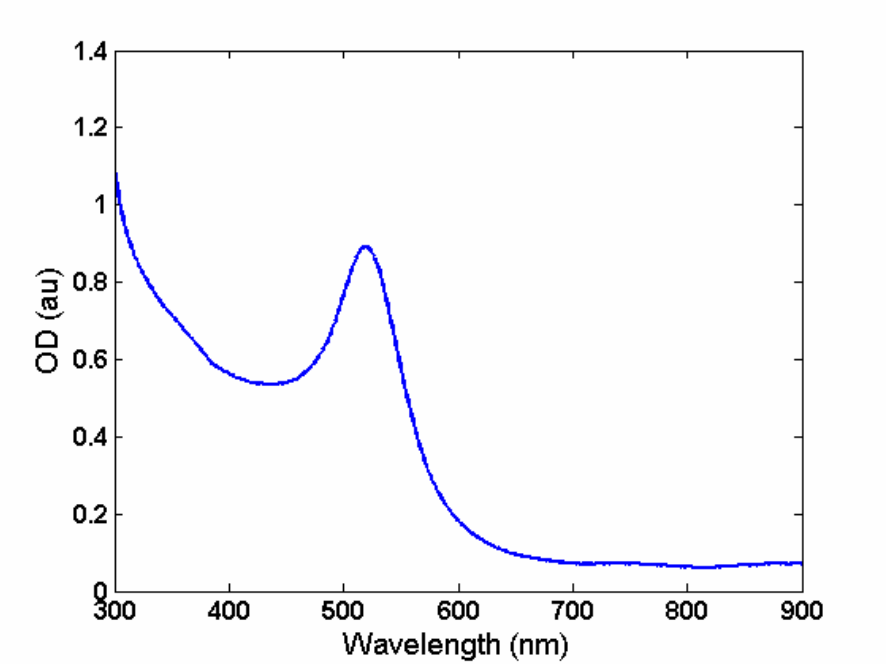

Figure 2.2. Optical extinction of 20 nm gold particles in aqueous solution [data unpublished].

As can be seen, this optical behavior produces a characteristic spectral signature, much in the same way a particular fluorophor would. One of the more attractive properties of gold nanoparticles, however, is a scattering cross-section (which is defined later) that greatly exceeds the analogous fluorescence cross-section of most common fluorescent dyes. Moreover, since the light interaction of interest is based on elastic scattering, photochemical reactions do not occur. Figure 2.3 graphically illustrates the relative optical cross sections of gold nanoparticles as compared to other common optically active materials. The scattering cross section of gold nanoparticles is significantly larger than the fluorescence cross section of conventional probes such as rhodamine-6G, FITC, a typical Alex Fluor dye, or enhanced green fluorescent protein (eGFP). Indeed, one 60 nm gold particle has the same cross section as 3×10^5 fluorescein molecules. This allows for much more sensitive detection schemes that are also more stable over time. It has been reported that gold nanoparticles can be detected down to a

concentration of 10^{-14} M in bulk spectroscopic measurements [189], and single particles can easily be detected under appropriate illumination conditions [190].

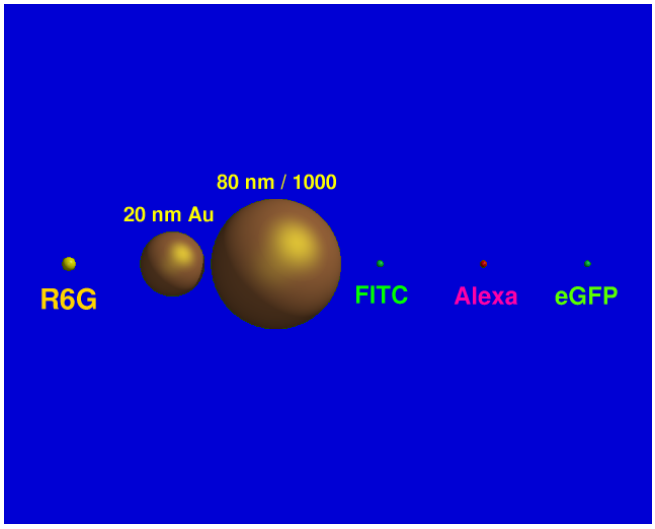

Figure 2.3. Relative efficiency factors of nanoparticles compared to fluorescent dyes [data unpublished].

As stated before, the peak wavelength of a particle's plasmon resonance is a function of particle size, shape, material, and surrounding media [159]. The theoretical reasons for this will be explained later, but its implication is that plasmonic nanoparticles can exist in differing "colors" – that is, their maximal scattering wavelength can be adjusted by changing size, shape, or constituent material. For example, figure 2.4 shows scattered light from a series of metal colloidal solutions of varying sizes (15-200nm) and varying materials (gold, silver, or alloy of both), indicating the range of colors possible.

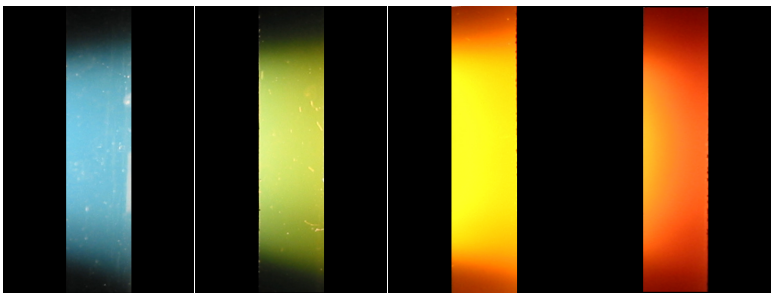

Figure 2.4. Scattering from colliodal solutions of varying compositions and sizes [data unpublished].

While these observations have attracted much attention, perhaps the most intriguing properties of plasmonic nanoparticles center around the optical property shifts seen in nanoparticle clusters. It has been observed that as the mean interparticle distance in a group of plasmonic nanoparticles decreases, the scattering efficiency *per particle* increases, along with a substantial red shift and broadening of the plasmon resonance peak [74, 191-194]. Figure 2.5 shows scattering spectra from a solution of isolated and antibodyaggregated 25nm gold nanoparticles [195], consistent with other studies [191, 196].

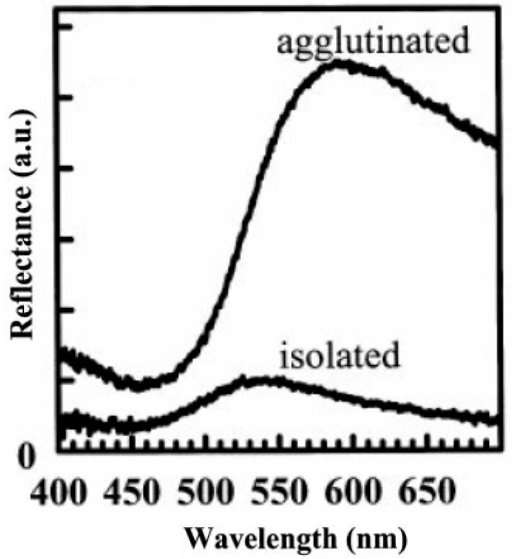

Figure 2.5. Scattering increase and red shift of aggregated particles.

2.6.2 Theoretical Descriptions

The theoretical treatment describing scattered light from a sub-wavelength particle has been developed in various forms since at least the time of Lord Rayleigh. This description is based on the presumption that the free electrons on the particle surface are induced to oscillate in a dipole at the same frequency as the impinging electromagnetic (EM) radiation. This, in turn, produces a secondary EM field with the same frequency

[159]. In the case of gold (and silver as well), the dielectric properties are such that an optimum wavelength exists, at the plasmon spectral peak (refer to figure 10), where the induced electric field will be the greatest. Thus, if a population of particles is illuminated with a broadband light source, the particle will preferentially scatter certain wavelengths more than others in the optical range. As stated before, this peak wavelength is a function of the particle material, size, shape, and the surrounding dielectric environment.

The theory put forth by Lord Rayleigh in the middle of the 19th century can accurately describe the dipole scattering of particles that are substantially smaller than the illumination wavelength. It assumes that the electrons oscillate in unison, or that the dipole shows no phase shift across the dimension of the particle. Although this is not a completely accurate description, the theory holds quite well for particles less than about 40 nm [159]. Specific cases can be made for differing polarization schemes, but for the general case of unpolarized light impinging on a particle with a corresponding detection direction (defined by spherical coordinates θ, φ, and *r*), the detected intensity of scattered light, I_U, at a distance r from the particle center is as follows:

$$I_U = \frac{8\pi^4 a^6 n_{med}^4 I_0}{r^2 \lambda_0^4} \left| \frac{m^2 - 1}{m^2 + 2} \right|^2 (1 + \cos^2 \theta).$$

Where *a* is the particle radius, n_{med} is the refractive index of the surrounding media, I_0 is the impinging light intensity, *r* is the distance from the particle to the detector, λ_0 is the impinging wavelength, and *m* is the *relative* refractive index of the particle (i.e. n_p/n_{med}). Since metal nanoparticles are both scatterers and absorbers, a complex refractive index is necessary to fully describe their interaction with light. Although Rayleigh theory was originally put forth to describe purely scattering particles, it also holds for the case of

complex refractive indices. And, if the dielectric function is large and negative, this indicates that the electric field in and around the particle will be greatly enhanced – thus pointing to the reason for the relatively large optical cross section. To calculate this value directly, the above expression is integrated over all angles θ, and r is set to unity, the resulting expression is defined in terms of area. This quantity is useful in describing the overall scattering efficiency of the particle, and its physical significance can be interpreted as an area surrounding the particle in which an impinging photon will be scattered.

$$C_{sca} = \frac{128\pi^5 a^6 n_{med}^4}{3\lambda_0^4}\left|\frac{m^2-1}{m^2+2}\right|^2$$

The expression indicates that the scattering cross section increases with the sixth power of the radius and decreases with the fourth power of the incident wavelength. This would indicate a monotonic change in scattering with wavelength, but another determining factor in the overall spectral shape is the refractive index, whose absolute value reaches a peak in the optical range – corresponding to the plasmon resonance wavelength. This wavelength indicates the frequency at which the electric field-induced oscillation of the conduction band electrons requires the least amount of energy to displace a given distance. In general, larger particles of a given material have a more red-shifted plasmon peak compared to smaller particles. The presence of a surrounding media with a high refractive index will also serve to decrease this resonant frequency. Finally, irregularly shaped particles may have multiple resonances corresponding to oscillations along different geometrical axes of the particles – and thus the effective dielectric function will have a polarization dependency.

While useful, the Rayleigh description does not fully describe light interactions with isolated metal nanoparticles. Besides its applicability to only a limited range of sizes, it also assumes that the only electric field perturbations experienced by the particles are caused by the incoming light. It does not take into account the secondary electric fields produced by other nearby particles. This would be needed if the aggregation effects are to be fully described theoretically. To accomplish this, a more robust theory must be utilized. In 1908, Gustav Mie put forth a rigorous solution to Maxwell's equations for perfectly spherical scatterers [159]. This theory takes into account the phase differences in oscillating electrons across the dimension of the particle as a result of the coherent electric field impinging on it, as well as more complex oscillation modes such as a quadropole, octopole, etc. This theory can be used to extrapolate the light scattering behavior from particles of a variety of geometries such as particles with concentric layers, aspherical particles, etc., although these treatments tend to be approximations. While a rigorous analysis of this theory is beyond the scope of this dissertation, the basic Mie expression for scattering cross-section C_{sca} of a spherical particle is given below:

$$C_{\text{sca}} = \frac{2\pi}{k^2} \sum_{n=1}^{\infty} (2n+1)(|a_n|^2 + |b_n|^2)$$

Where k is the wave number; n is the complex refractive index; and a_n and b_n are defined by Bessel and Ricatti functions [159]. For those particles less than approximately $1/20^{th}$ of the impinging wavelength, Mie theory can be simplified to the Rayleigh expression. Several good sources are available for an in-depth analysis of Mie theory, including [159, 197].As stated previously, Mie theory may be adapted to calculate the resulting scattered electric field from a collection of closely spaced nanoparticles, or

alternatively, irregular shaped particles. The discrete dipole approximations and T-matrix implementation are two widely used, but complex frameworks in which to address this phenomenon [198, 199]. An instructive exercise, however, can be made in the case of only two, small, interacting gold particles, as shown in figure 2.6.

Figure 2.6(A) shows that when the electric field is oscillating orthogonally to the long axis of the particle pair, the induced dipole is such that charges of the same sign from each particle are always nearest each other. This causes a charge repulsion effects between the two particles. These repulsion effects tend to make the optimum oscillation frequency higher (but with damped amplitude), which results in a blue shifting and overall decrease in intensity of the plasmon peak. In (B), the particle pair's long axis is parallel to the oscillating electric field. In this case, charges of opposite sign from each particle are nearest each other, resulting in a red-shifting and un-damping of the plasmon resonance, for the reasons explained above. This explains why the red-shifting portion is dominant, although both effects are present in aggregated particles [191, 197].

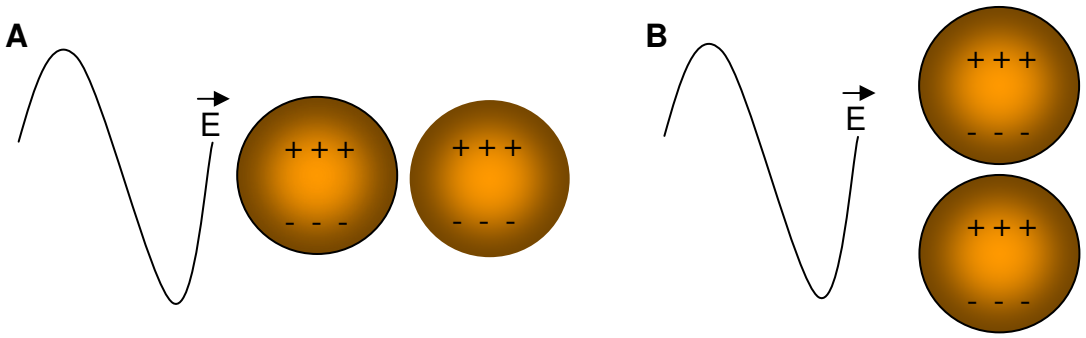

Figure 2.6. Plasmon coupling between two closely spaced gold nanoparticles. (A) When the electric field is oscillating orthogonally to the long axis of the particle pair, the induced dipole is such that charges of the same sign from each particle are nearest each other. This causes a blue shifting of overall plasmon resonance. (B) When the particle pair's long axis is parallel to the oscillating electric field, charges of opposite sign from each particle are nearest each other, resulting in a red-shifting of the plasmon resonance.

While this can explain the red and blue-shifting of plasmons and their relative intensities, it does not fully account for the large, non-linear increase in scattering cross section seen gold nanoparticle aggregates. To answer this, one must turn to coherent backscattering theory [200], which explains that for particles in dense clusters produce an effect, arising from the coherent constructive addition of the backscattered light, that results in a second-order increase in scattering cross-section with number of particles (for a given distance). This means that the scattered light will increase as the square of the number of particles in an aggregate. Both the overall red-shifting and increase in overall scattering cross-section serve as powerful contrast enhancing mechanisms for molecular imaging.

2.6.3 Synthesis and Bioconjugation

The synthesis of nanometer-sized gold particles has been performed in a controlled environment since the 1950s, although the process was refined by Frens in the 1970s [201] and was believed to be performed by Faraday in the 1850s. By far the most common approach to synthesis in solution has been the chemical reduction of a gold salt – usually $HAuCl_4$ – to metallic gold in colloid form. Various reducing agents have been utilized, the most common being citrate [201], although ascorbate [202], sodium borohydrate [203], and pure hydrogen among others. In addition, other methods employing ultrasonication [204], electrochemical techniques [205], as well as lithographic strategies [206] have also been used in certain applications. The chief concern when synthesizing *colloidal* gold is the control of size and size distribution. This can be altered by the relative concentration of gold ions to reducing agents, as was shown by Frens [201]. The mechanism for this is presumed to be simple: In the Frens study,

citrate is hypothesized to act as a nucleating agent, as well as the reducer. By lowering the citrate to gold ratio, there are fewer nucleation sites available for particle synthesis, and thus a given amount of gold must be reduced into larger particles at completion. A larger number of nucleation sites translate to more, but smaller particles. Of critical importance is the ability of the reducing agent to also stabilize the particles in solution from aggregation. Polymers such as poly ethylene glycol (PEG) and poly vinyl pyrrolidone (PVP) have been used as adjuvant stabilizers to create longer-lasting colloidal solutions.

Stabilization becomes particularly important when synthesizing other metal nanoparticle geometries. To date, a dizzying array of nanoparticle shapes has been synthesized through a wide variety of methods to modulate and optimize particular optical properties. Popular materials include nanorods [207], triangles [208], nanoshells [30, 209, 210], cubes/cages [211], and stellated nanoparticles [212].

Clearly, in order to target gold nanoparticles to a biological sample, conjugation of a biomolecular recognition molecule is essential. The attachment of biomolecules to gold nanoparticle surfaces has been studied extensively, primarily as a means for molecular tagging in electron microscopy applications [67, 213-215]. It was shown that various proteins would physically absorb to the gold surface in a pH dependent manner, where the highest efficiency absorption occurred at or near that protein's isoelectric point (pI) [68] . Simple centrifugation enabled the separation of conjugated and unconjugated proteins. More recently, it has been found that a stable bond between a thiol moiety and gold surfaces is formed under most conditions. This was first reported as a method for preparing self-assembled monolayers (SAMs) onto planar gold surfaces [216], and was

adapted for conjugation to particle surfaces [217]. The gold-thiol reaction represents a flexible and powerful method for bioconjugation, producing bonds that are considered covalent in their strength. In either case, it is important to ensure that the bioconjugation of targeting molecules not interfere with their native function. Fortunately, antibodies, which represent a powerful means of targeting, do not show this tendency. Care must be taken, however, in the case of smaller peptides or nucleic acid sequences such that their conformation does not change to affect their utility.

2.6.4 Optical Interrogation

While the synthesis and bioconjugation of gold nanostructures remains an active area of research, their optical detection in a biological environment remains a paramount consideration. Several modalities exist which are suitable for this purpose, and the selection of a particular method is often application specific. Perhaps the simplest and first to be developed is darkfield microscopy. This is an adaptation of brightfield microscopy which allows the detection of scattered light, while rejecting the primary illumination. It involves illuminating the sample with an oblique cone of light such that the incident numerical aperture (as defined by the angle at which it is focused onto the sample) that is higher than the detection numerical aperture. Thus, only higher diffraction orders are allowed to pass to the detection path of the microscope. This can be accomplished either via a transmitted or epi-illuminated geometry, although the later requires a specialized objective that has a separate illumination and collection compartments. The transmitted case is illustrated in figure 2.7. Note the use of a dark field patch stop, which is essentially an absorbing annulus in the illumination path, in order to create a hollow cone of light that is focused at high NA.

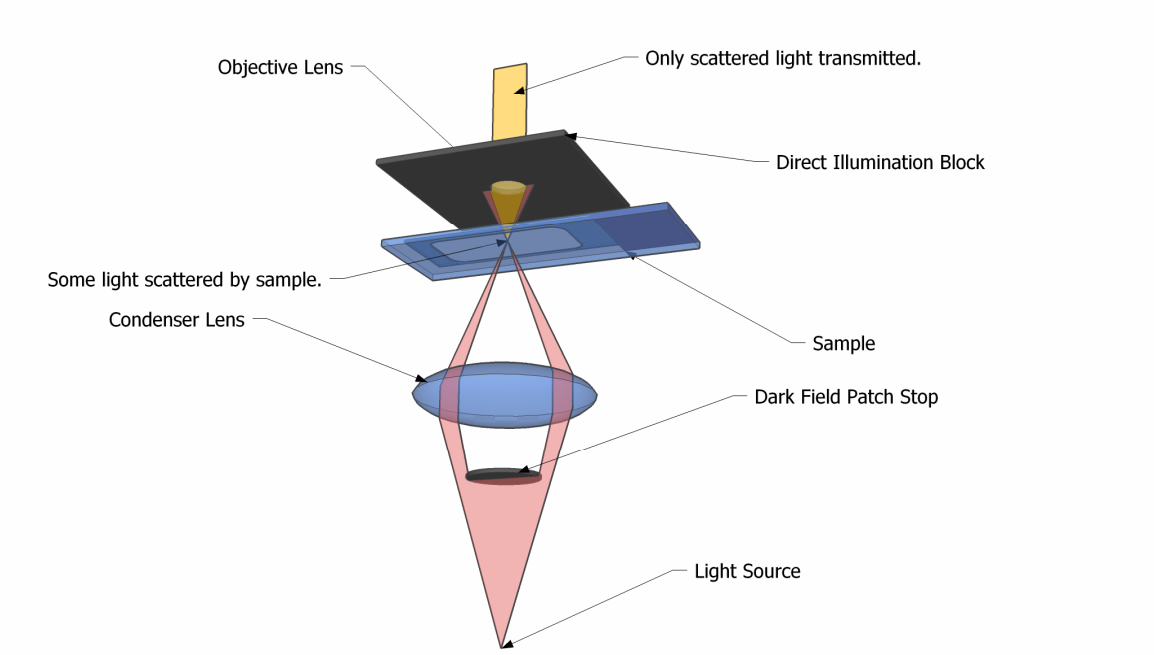

Figure 2.7. Optical setup required for transmitted darkfield microscopy. Note the dark field patch stop, which is essentially an absorbing annulus placed in the illumination path. This creates a hollow cone of light that is focused onto the sample at high NA. (Copyright 2006 by Richard Wheeler, used with permission.)

This keeps the primary light from entering the objective, allowing only higher-order scattered light from being detected. A similar setup is used in the epi-illuminated case, whereby light is focused through an outer annulus in a specialized objective, and collected through an inner annulus.Darkfield microscopy is useful, in that it allows excitation of the sample with a broadband light source. However, the axial resolution attainable through this setup is determined by the focal volume of the objective, and as such, out-of-focus light is detectable. For simple samples consisting of a single cell layer, this is generally sufficient to produce high-quality images. However, for thicker samples, an optical sectioning modality is preferable. As discussed previously, reflectance confocal microscopy or OCT can be used for this purpose. Confocal microscopy is capable of optical sectioning with submicron resolution of samples that are

several hundred microns to millimeters thick, under ideal conditions [145, 218, 219]. However, most systems use laser illumination, and thus do not provide spectrally sensitive information in reflectance mode. OCT systems can often penetrate deeper into tissues than confocal, but generally suffer from lower resolutions [53, 151].

To gain more detailed spectral information, traditional spectroscopy is an obvious option. However, the lack of spatial information attainable in traditional spectroscopy begs the question as to whether a modality can be developed that will deliver both detailed spatial and spectral information. As such, the emergence of hyperspectral imaging systems has been an exciting development [220]. This method refers to a set of instruments that are capable of collecting a three-dimensional data set of a sample of interest – i.e. two spatial and a spectral dimension.

There are two commonly used setups that are used to achieve this. The first utilizes Fourier spectroscopy concepts, adapted for imaging. At its core, this type of system is an interferometer spectrometer, much like conventional FTIR spectrophotometers. However, while in the latter case, a single beam of light is passed through the sample and projected through the interferometer, the hyperspectral imaging device projects the sample *image* through the interferometer. By modulating the path length difference (PLD), an interferogram is constructed and imaged using a CCD camera. Simple FFT algorithms then extract the spectrum at each pixel [221]. Another, more direct method of hyperspectral imaging relies on simply segmenting a two-dimensional image into one-dimensional components, and spectrally dispersing each in series. In a typical setup, a slit is placed in the detection path of a microscope, which is projected through the detection path onto a dispersive prism or grating. At this point, the one-dimensional

"slice" is dispersed into a two-dimensional spectrum onto a CCD detector. This process can be repeated by serially scanning the sample across the slit using a controllable translation stage, building a three-dimensional data set [222].

The relevant considerations in utilizing hyperspectral imaging include acquisition times, as well as spatial and spectral resolutions. In the past, Fourier based systems offered better signal-to-noise as compared to dispersive systems, mainly due to the fact that the entire spectral bandwidth of the sample is imaged at once, and repeated for different interferometer path length differences. However, the drawback remains that these systems tend to necessitate many acquisitions to produce a data set, and suffer from limited spectral resolution. More recently, however, CCD technology has advanced sufficiently that dispersive instruments can now offer comparable SNR, with superior spectral resolution. In either case, this modality remains a powerful technique. Indeed, with the combination of confocal microscopy, hyperspectral imaging can produce images with x, y, z, and wavelength resolved signal for a complete four dimensional characterization of a sample [223]. Such advanced imaging systems may in the future provide a complete characterization of nanoparticle labeled biological tissues for diagnostic and screening purposes by giving invaluable insight into the nanoscale arrangement of biomolecules within the cellular architecture.

2.7 RELEVANT LITERATURE SYNOPSIS

Though a relatively recent area of active research, the use of metal nanoparticles for optical molecular imaging has been proposed since the 1970s, due to their characteristic interactions with light, and favorable conjugation properties [224]. The first wide-spread uses of gold nanoparticles as optical detection tools were not, in fact, aimed at exploiting

their scattering properties, but rather the enormous multiplication of Raman signals due to the electric field enhancement apparent at the particle surface [225]. Their enhanced elastic scattering properties were not fully explored for biological detection until beginning in the late 1990s. Yguerabide et al. were able to demonstrate this approach convincingly in several landmark studies [70, 189, 226] whereby gold nanoparticles were shown to be effective reporters in DNA assays, cell surface protein detection assays, as well as *in-situ* hybridization studies. Schultz, et al., also showed the utility of this concept in similar studies (published nearly simultaneously), and demonstrated the multi-color, spectral tuning capabilities of this technique in similar model biological assays [63]. It is also important to note that it had previously been shown that DNA-directed nanoparticle binding could detect DNA mismatches via temperature cycling down to a single nucleotide base pair in a simple, non-microscopic colorimetric assays [73, 227], which indirectly showed the powerful possibilities of exploiting the distance-dependent optical properties of gold nanoparticles. This has spawned a plethora of studies utilizing gold nanoparticles as powerful agents for various studies of nucleic acid detection [228-241]. Of particular note is the is the work by Soennichsen, et al. who quantitatively demonstrated the phenomenon of plasmon coupling for determining DNA sequence length, to nanometer resolution [71].

For proteomic based studies, work by Sokolov, et al. showed the ability to image EGFR expression in a variety of vital biological samples, including live cells, tissue phantoms, and live *ex-vivo* tissue samples [195]. Since then, similar studies have followed using similar technologies for EGFR imaging [79, 81].

As an alternative to pure gold nanoparticles, Liz-Marzan, et al. were first able to successfully synthesize gold-silica core-shell nanoparticles, followed by work by the others [30, 209, 210]. These particles (termed nanoshells) are attractive, as the dielectric inclusion within the noble metal shell causes a marked and controllable red-shift of the plasmon resonance into the NIR region, making detection into deeper tissues easier. Since then, growth factor receptor imaging has been accomplished by Loo, et al. in breast cancer cell lines [32, 33]. These studies have also shown the possibility to exploit the light *absorption* properties of nanoshells. This absorption causes a local heating affect near the particle surface which can be harnessed to cause photothermal destruction of cellular tissue [242]. Because of this, a combined detection and therapy approach using plasmonic nanoparticles has become an intense area of interest, utilizing other particle geometries [243]. The work described above serves to illustrate the emerging breadth of the field of optical nano-biotechnology.

2.8 ACKNOWLEDGEMENTS

The author would like to thank Kort Travis for generating cross section data, and for numerous helpful discussions on nanoparticle scattering theory.

CHAPTER 3

Single Cell Studies of EGFR Detection Using Gold Nanoparticles*

3.1 ABSTRACT

The use of metal nanoparticles has been recognized as a potential tool for molecular imaging, particularly in detection of carcinogenesis, as well as concurrent photothermal therapy of the same tissue. In the last several years, studies have shown that the remitted optical signal from cells can be enhanced with the use of plasmonic nanoparticles, and with the addition of antibody targeting, molecular-specificity can be achieved. However, the concept of plasmon coupling has been ill-explored as a mechanism for this enhancement. While plasmon coupling has been utilized in some studies of DNA hybridization and enzymatic cleavage [71, 72], its implications have not been fully elucidated. Further, plasmon coupling has not been utilized previously for molecular imaging in living cells. The contents of this chapter serve to provide foundational studies and observations for satisfactorily characterizing plasmon coupling for detection of epidermal growth factor receptor (EGFR) in suspensions of single cells. These results show that labeling EGFR with immuno-targeted gold nanoparticles results in protein-mediated clustering of the particles on the cell surface. This, in turn, produces a more than 100nm shift in the plasmon resonance wavelength as compared to isolated particles, as well as a non-linear increase in scattering intensity with respect to the number of

* The contents of this chapter have been published in *Cancer Res.* **63**, 1999-2004, (2003), and *J. Biomed. Opt. (2007),* (in press).

clustered particles. The result is highly enhanced optical signals (up to an order of magnitude increase) in the red and NIR spectral regions. In addition, the spectral information contained in these signals can potentially yield information not only about EGFR over expression, but also the nanoscale relationship among these receptors in the cell membrane. These observations serve to prompt further questions as to the specific molecular trafficking and interaction events that are responsible for nanoparticle clustering, as well as providing critical insight for later use in more complex biological models of carcinogenesis.

3.2 INTRODUCTION

A number of different types of nanoparticles have recently been proposed for use as optical imaging agents to aid in cancer detection, including quantum dots (qdots) [180-182], nanoshells [244], and metal nanoparticles [70]. The use of nanoparticles for molecular imaging of cancer has several important advantages. Their surface chemistry is well understood, so that they can be easily targeted using antibodies or aptamers to bind to cancer biomarkers. By adjusting the particle geometry, the optical properties can be tuned over a large spectral region to provide multi-color labeling. The bright reflectance or luminescence of nanoparticles provides a strong source of signal for in vivo imaging. Finally, multiplexing different types of particles and targeting molecules provides a common platform for multiple applications with a high degree of flexibility [181].

Each nanoparticle type has inherent merits, and the selection of an appropriate tool will certainly be application-dependent. As discussed previously, metal nanoparticles have several advantages for a number of applications. These include large plasmon-dependent signal and absorption cross-section, photostability, ease of synthesis, non-

toxicity, ease of conjugation, and most importantly, the tendency to shift their optical properties in the presence of other particles. In this way, metal nanoparticles offer an intriguing opportunity to probe and monitor the molecular and cellular events of tumorigenesis in real time via light scattering [34, 81, 195, 245], as well as the ability to therapeutically impact diseased tissue via light absorption [32, 77, 242]. Gold nanoparticles have been extensively used as molecular specific stains in electron microscopy, as well. As a result, the fundamental principles of interactions between gold particles and biomolecules have been thoroughly studied for more than 20 years [68, 224]. The ability to resonantly scatter visible and NIR light, however, has not been extensively explored for vital microscopy in living specimens.

In particular, the focus of these studies is to establish the principles of metal nanoparticle plasmon coupling as a tool for molecular imaging. The main tool in these studies are bioconjugates of gold nanoparticles with monoclonal antibodies against EGFR, a transmembrane 170 kDa glycoprotein that is overexpressed in epithelial pre-cancers [100, 102, 113, 246-251] for molecular specific optical imaging. A high level of EGFR expression is often associated with enhanced aggressiveness of epithelial cancers and poor prognosis [102, 252, 253]. In these studies we used *c.* 20-25 nm diameter gold nanoparticles. This size is approximately the same as the size of antibodies, which are routinely used for molecular specific labeling and targeting. However, there are a number of barriers to achieve robust use in a clinical, *in-vivo* application, including development of: (1) molecular-specific bioconjugates that can be safely used in humans; (2) delivery formulations for these contrast agents in vivo; and (3) cheap, flexible imaging tools. It seems likely that such a comprehensive strategy requires that a step-

wise approach, using increasingly complex models, be used in evaluating the utility of such a strategy. To that end, the contents of this chapter will be limited to studies using the simplest living eukaryotic model – cell suspensions. This relatively simple, reproducible, and highly flexible model represents a reasonable position in which to begin studies.

This chapter enumerates several important developments, observations and implications of using immuno-targeted gold nanoparticles on simple cell suspension models as a first testing ground for exploring plasmon coupling in living systems. Initially, the conjugation strategies used to link metal nanoparticles to the targeting monoclonal antibody are discussed in detail. In addition, the strengths and weaknesses of the various optical modalities used in this chapter's studies are also enumerated. Later, darkfield and confocal images of labeled and unlabeled cells are shown to qualitatively indicate the scattering intensity and spectral changes that occur when labeling cancer cells, particularly as a result of the aggregation of particles on and near the cell membrane. These aggregation-dependant changes are quantified on a cell-by-cell basis using hyperspectral imaging. The presence of particle aggregation on the cell surface is confirmed by electron microscopy imaging.

3.3 MATERIALS AND METHODS

3.3.1 Conjugation of Anti-EGFR Antibodies to Gold Nanoparticles

Two main antibody clones were used in these studies as targeting molecules. The first, anti-EGFR clone 225 is widely available as a therapeutic agent which blocks EGF and other ligand binding sites [254] on the extracellular domain of the receptor. The

other clone, 29.1, similarly targets the extracellular portion, but localizes to a glycol-moiety such that it does not block ligand binding [255], and was chosen to minimize any biological modulation from antibody binding.

There were two main strategies used for linking the antibodies to the gold nanoparticle surface: (1) Physical absorption and (2) covalent linkage. Traditionally, physical absorption of antibodies has been by far the simplest and most widespread strategy used, particularly when preparing immuno-targeted gold particles for electron microscopy applications [68, 97]. A typical protocol involved the following steps: 0.1 mg/mL of anti-EGFR antibodies in a 40 mM HEPES buffer, pH 7.4, were mixed for 20-30 minutes with an equal volume of 25nm gold nanoparticles (which were prepared using the aforementioned citrate reduction method [201]. Conjugates were centrifuged at 3000 rcf for 1-1.5 hours in the presence of 1% PEG and re-suspended in a PBS buffer, pH 7.4 containing 1% BSA and 0.2% PEG as stabilizers.

More recently, covalent strategies have been developed to improve the conjugation of proteins to noble metal surfaces. In particular, the gold-thiol reaction has been widely exploited as a means for creating self-assembled monolayers (SAMs) [256], and can be adapted for conjugating antibodies to gold nanoparticles. For experiments using covalently conjugated particles, the following protocol was used: Antibodies were attached to gold nanoparticles via a conjugation linker that consists of a short polyethylene glycol (PEG) chain terminated at one end by a hydrazide moiety, and at the other end by two thiol groups. First, antibodies at a concentration of 1mg/mL were exposed to 10mM $NaIO_4$ in a 40mM HEPES pH 7.4 solution for 30-40 minutes at room temperature, thereby oxidizing the hydroxyl moieties on the antibodies' Fc region to

aldehyde groups. The formation of the aldehyde groups was colorimetrically confirmed using a standard assay with an alkaline Purpald solution (Sigma). Then, excess hydrazide-PEG-thiol linker was added to the oxidized antibodies and allowed to react for 20 minutes. The hydrazide portion of the PEG linker interacts with aldehyde groups on the antibodies to form a stable linkage. In this procedure a potential loss of antibody function is avoided because the linker can not interact with the antibody's target-binding region, which contains no glycosylation. The unreacted linker was removed by filtration through a 100,000 MWCO filter (Millipore). After purification, the modified antibodies were mixed with gold nanoparticles in 40mM HEPES (pH 7.4) for 20 minutes at room temperature. During this step a stable bond is formed between the gold surface and the linker's thiol groups. Afterward, monofunctional PEG-thiol molecules were added to passivate the remaining nanoparticle surface. Finally, the conjugates were centrifuged at 2800 rcf for 45 minutes and resuspended in 1x PBS, producing a solution containing approximately 10^{12} particles per mL. In either case, conjugation of biomolecules to gold nanoparticles can be independently detected using UV-Vis spectroscopy by a 3-5nm red-shift in the plasmon peak position between bare and conjugated particles. This is due to a increase in the effective refractive index surrounding the particle [159]. Bifunctional contrast agents were synthesized via a monoclonal antibody labeling kit (Molecular Probes) to attach Alexa Fluor 488 dye to purified antibodies. Then, fluorescently labeled antibodies were conjugated with gold nanoparticles as described previously.

3.3.2 Cell Cultures

All cells were cultured in DMEM or MEM plus 10% FBS and grown at 37ºC in 5% CO_2. There were three main EGFR over-expressing cell lines used in the various studies:

(1) A-431 cells are an epidermoid keratinocyte, which expresses on the order of 10^6 EGFR molecules per cell, (2) MDA-MB-468 cells, which are a breast epithelial line derived from a ductal carcinoma and also express c. 10^6 EGFR/cell, and (3) SiHa, a line derived from a squamous epithelial carcinoma of the cervix, expressing c. 10^5 EGFR/cell. Cells were harvested using exposure to conventional buffered trypsin-EDTA, containing Phenol-red (Gibco) for 5 minutes at 37°C. After washing in phenol-free media, cell suspensions were labeled in a 50:50 (v/v) mixture of phenol/serum free DMEM and contrast agents for 30 minutes at room temperature, before being washed and resuspended in pure phenol-free media.

3.3.3 Optical Imaging

Reflectance confocal images of cells were acquired using a Leica TCS-4D confocal microscope using with 647 nm illumination under 40x objective magnification, with NA of 0.8. Darkfield and fluorescence imaging of cells was performed using a Leica DM6000 upright microscope configured with a 20X, 0.5/0.95 collection/illumination NA darkfield objective, fluorescence filter cubes (Chroma), and a 75W Xe light source. RGB images were captured using a Q-Imaging Retiga EXi CCD camera with color LCD attachment. Hyperspectral images were captured with either a SpectraCube® spectral imaging camera (Applied Spectral Imaging), using a Fourier spectroscopy based approach or a PARISS® hyperspectral imaging device (LightForm, Inc.), which uses a prism dispersion based technique. Bifunctional contrast agents were imaged with 633 nm excitation and 650-700 nm emission bandwidth. Imaging of hamsters *in vivo* was carried out using a portable reflectance confocal microscope which is described in.

3.3.4 Scanning Transmission Electron Microscopy

Labeled A-431 cells were absorbed onto a gold/carbon film grid and dehydrated in a 5-part water/ethanol series for 50 minutes. After light fixation in 2% glutaraldehyde for an additional 10 minutes, samples were then subjected to a 5-part ethanol/acetone exchange for another 50 minutes at room temperature. This allowed for the sample to be placed in an automated CO_2/acetone critical point drying apparatus (Samdri-790, Tousimis, Corp.) which makes it possible to avoid surface tension-induced disturbances of the cell surface [257]. Cells were imaged with a JEOL 2010F STEM equipped to image in Z-contrast mode. A HAADF detector (50 – 110 mrad) was used for image acquisition with a probe size of 0.2 nm. In addition, the JEOL STEM system contains atom-level probes connected to an Oxford INCA Energy Dispersive Spectrometer (EDS) to positively identify the presence of gold on the cellular surface.

3.3.5 Image Analysis

All images were analyzed using NIH ImageJ. Regions of interest were manually segmented; background signal was evaluated from an area that contained no cells, and was subtracted; then, the non-zero pixel values were isolated and the mean was evaluated to calculate average intensity and contrast values.

3.4 RESULTS

3.4.1 Confocal Imaging of Cells Labeled with Anti-EGFR Conjugates

Confocal microscopy is a widely used optical imaging modality, [258-260], as its high resolution, both in the lateral and axial directions, renders it attractive in biological studies [219] . The improved axial resolution is a result of a pinhole located at the conjugate image plane, as well as the scanning action of the illumination/excitation laser [261], which allows for an “optical sectioning” ability that gives three-dimensional

information. To evaluate whether confocal reflectance imaging can be used to detect differences in scattering due to EGFR-labeling using gold nanoparticles, Figure 3.1 (A-D) shows confocal reflectance images (left column) and combined transmittance/reflectance images (right column) of SiHa cervical cancer cells labeled with anti-EGFR/gold conjugates for 45 minutes at room temperature. In a series of through focus confocal reflectance images of labeled cells, the bound conjugates first appear as randomly distributed bright spots at the top of the cells (A and B), then bright rings can be seen in the optical cross-sections through the middle of the cells (C and D). The labeling pattern is consistent with the fact that the monoclonal antibodies have molecular specificity to the extracellular domain of EGFR. The intensity of light scattering from the labeled SiHa cells is *ca.* 50 times higher than from unlabeled cells, as determined by image analysis. Therefore unlabeled cells cannot be resolved on the dark background. Similar results were observed when gold conjugates with bovine serum albumin (BSA) were added to the cells (Figure 3.1, E and F), further bolstering the contention that the conjugates are bound specifically to the EGFR contained in the cell membrane. These negative controls also displayed 30-50 fold less signal than labeled cells.

We also conducted reflectance imaging before and after the unbound gold conjugates were washed from the cell suspension (data not shown). The unbound gold particles were not detectable in confocal either before or after washing. This is an important observation, as it indicates that in the red optical region, the particles on the cell surface are considerably brighter than any that might exists in the extracellular space, consistent with the aggregation-dependent red-shift in plasmon peak position and coherence-based

scattering efficiency increases described in the previous chapter. However, broadband illumination would be necessary to further establish this fact.

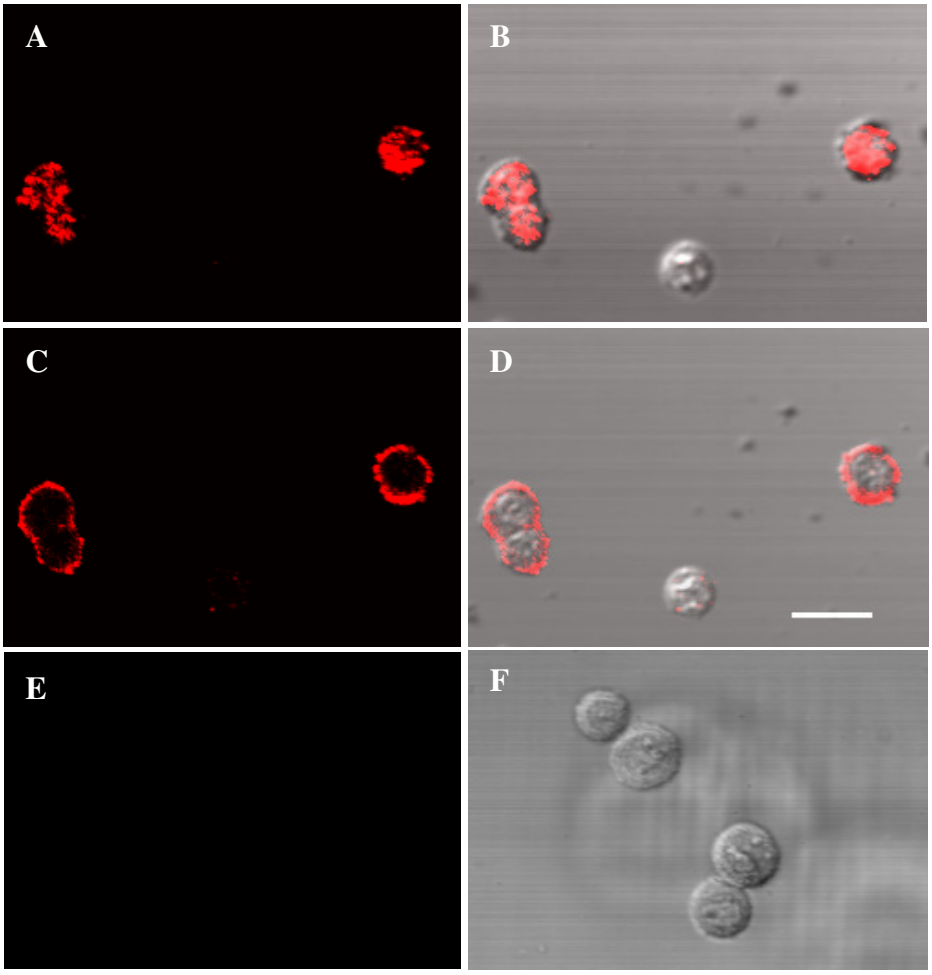

Figure 3.1 Laser scanning confocal reflectance (A, C, and E) and combined confocal reflectance/transmittance (B, D, and F) images of the labeled SiHa cells obtained with 40X objective. In (A) and (B) the focal plane is at the top of the cells. In (C) and (D) the middle cross-section of the cells is in focus. The confocal reflectance and transmittance images were obtained independently and then overlaid. Non-specific labeling using gold conjugates with BSA is shown in E and F. Note the absence of cell labeling after exposure to non-specific conjugates. The scattering from gold conjugates is false-colored in red. Images were obtained with 647 nm laser excitation. The scale bar is *ca.* 20 μm (A-F).

3.4.2 Darkfield Imaging of Cells Labeled with Anti-EGFR Conjugates

To better illustrate this effect on the cell surface, SiHa cells were labeled with 25nm anti-EGFR gold nanoparticles as before, and subjected to darkfield imaging under white

light illumination with a 75W Xenon source. Because of the broad-band nature of this illumination, the resonant scattering behavior of nanoparticles is much more apparent relative to laser illumination. Figure 3.2A shows the natural scattering appearance of SiHa cells, while figure 3.2B shows the same cell line after labeling with anti-EGFR gold conjugates. This figure illustrates two important phenomena. First, the gold nanoparticles dramatically increase the overall optical scattering signal from cells. Figure 3.2A was acquired at 3 times the exposure time as figure 3.2B in order for both cell populations to be visible above the background in the images. Secondly, the gold nanoparticles produce a marked color change in the SiHa cells. As is indicated by the green arrow, portions of the cell appear green, consistent with the plasmon peak of approximately 530nm seen in UV-Vis measurements of isolated particle solutions.

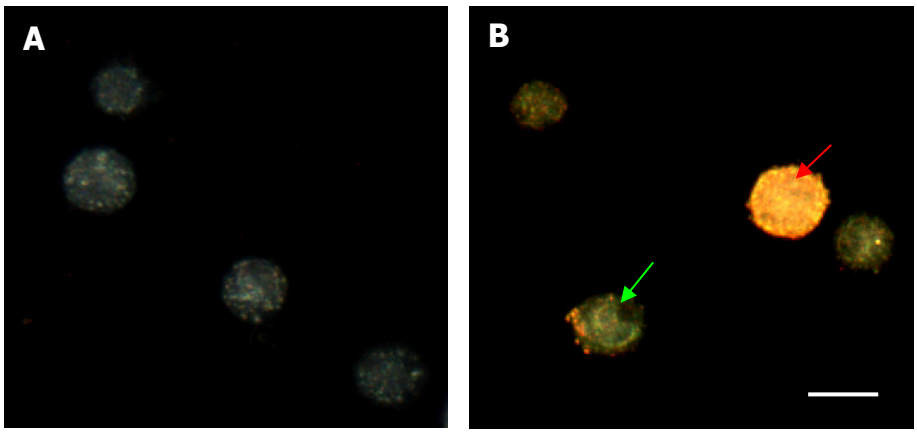

Figure 3.2 (A) unlabeled SiHa cells and (B) SiHa cells labeled with contrast agents for 45 minutes at room temperature. Darkfield images under white light illumination show the color change associated with gold nanoparticle labeling of EGFR on SiHa cervical cancer cells. In (B), Note that some portions of cells are green in color, consistent with the optical properties of a relatively disperse population of nanoparticles (indicated by green arrow). However, other portions of cells appear orange-red, indicative denser aggregation of particles, which produces a red-shift in the plasmon peak, as well as increased per-particle scattering efficiencies. It is important to note that (A) was acquired at 3 times the exposure time as (B). Scale bar is c. 20μm.

In addition, however, other portions of the cells appear a distinct orange-red (indicated by red arrow). This is highly consistent with measurements taken of solutions of aggregated gold nanoparticles, whose plasmon peak is broadened and shifted to the 600-650nm range (relative to isolated particles).

3.4.3 Hyperspectral Imaging of Labeled and Unlabeled Cells

These observations, however, are better supported by a spectral analysis of the optical signals from labeled cells. To do this, however, requires an increased level of sophistication. To that end, we coupled a hyperspectral imaging device (SpectraCube, Applied Spectral Imaging, Inc.) to the darkfield microscope. This Fourier-based imaging spectrometer enables a precise intensity vs. wavelength relationship to be measured at each 2D pixel position in the darkfield image, thus creating a three-dimensional data set for each field of view. In this way, a very detailed description of the scattering signal (localized within a single cell) can be shown. Figure 3.3 shows a typical comparison between scattering spectra from a labeled cell and compared with spectra from a cell not exposed to contrastagnets, shown by the red and green curves, respectively. Note that in the case of the unlabeled cell, the scattering profile shows a monotonic decrease in scattered light vs. wavelength, which is predicted in the case of light scattered from a dielectric sphere [159], and has been also observed in living cells [152]. Spectra from labeled cells (shown in red) display a prominent resonance peak at approximately 650nm. This is highly consistent with independent bulk UV-Vis measurements of aggregated nanoparticles [195], and represents a more than 100nm red-shift in the peak scattering wavelength for these particles.

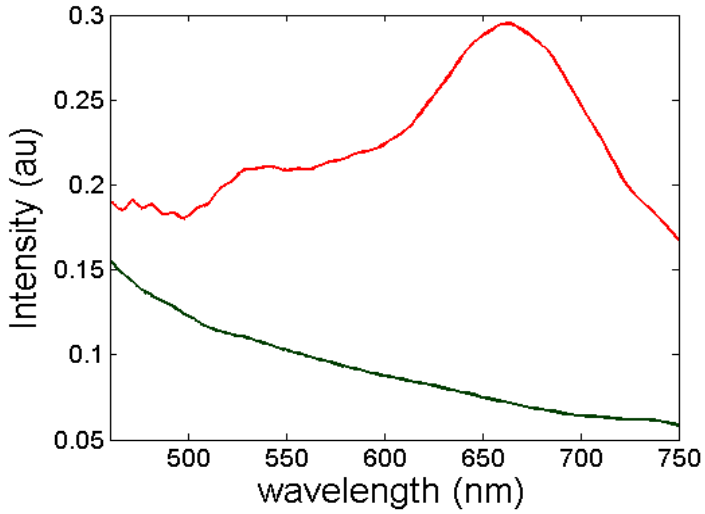

Figure 3.3 Hyperspectral data taken from a labeled cell (red line) and unlabeled cell (green line) under darkfield illumination. Note that the scattering signal from the unlabeled cell follows a characteristic inverse-power type profile indicative of scattering from a dielectric particle. The labeled cell, however, displays a prominent peak at approximately 650nm, consistant with bulk UV-Vis measurements of aggregated gold nanoparticles.

3.4.4 Quadratic Dependence of Scattering Efficiency on Aggregate Size

While the dramatic color changes associated with plasmon coupling on the cell surface serve to act as a powerful contrast enhancing mechanism, the increase in overall scattering efficiency per particle is equally important. As stated before, the wavelength-integrated scattering cross section can be shown to be proportional to the number of particles in an aggregate squared [262]. To characterize this non-linear scattering intensity increase associated with metal nanoparticle plasmon coupling, the following experiment was devised: EGFR-over expressing A-431 epidermoid keratinocytes were labeled with bifunctional contrast agents, consisting of a fluorescently-tagged antibody which was then conjugated to the gold nanoparticle. Thus, the contrast agent will produce both a relatively strong fluorescence signal and a characteristic scattering profile. To a very good approximation, the fluorescence signal will be proportional to the number

of gold nanoparticles in a given imaging volume, as the degree of fluorescence labeling of the antibody is a highly controlled reaction. Cells are then imaged in both darkfield and fluorescence modes in an identical field of view. These two images were then compared on a pixel-by-pixel basis. The Leica DM6000 was used both both modalities, as the illumination turrent has been evaluated to produce a zero-pixel shift when switching between illumination modes. It was assumed that the fluorescence image pixel value was proportional to the number of fluorophors in that imaging volume, as thus also the number of nanoparticles in that volume. The darkfield image pixel intensity is proportional to the total scattering cross-section of particles in the same volume. This assumption provides a way to compare the scattering intensity of nanoparticle aggregates as a function of the number of particles in that aggregate. The results are plotted in figure 3.4 below, and show a range of fluorescence and darkfield pixel values from an image of A-431 cells labeled with bifunctional contrast agents (see inset).

The range of fluorescent pixel values is due to a range of particle concentrations from pixel to pixel, while the range of darkfield values (which is taken as a sum of the three RGB channels) indicates a corresponding range of degree of aggregation. Each pixel, with an area of 0.1 μm^2 at 20x magnification, can potentially contain nearly 100 particles if closely packed, thereby allowing a wide range of possible aggregation states in each pixel. The resulting pixel-by-pixel plot shows a non-linear increase in scattering as a function of number of nanoparticles, which agrees with the theoretically predicted quadratic increase with a R^2 value of 0.85.

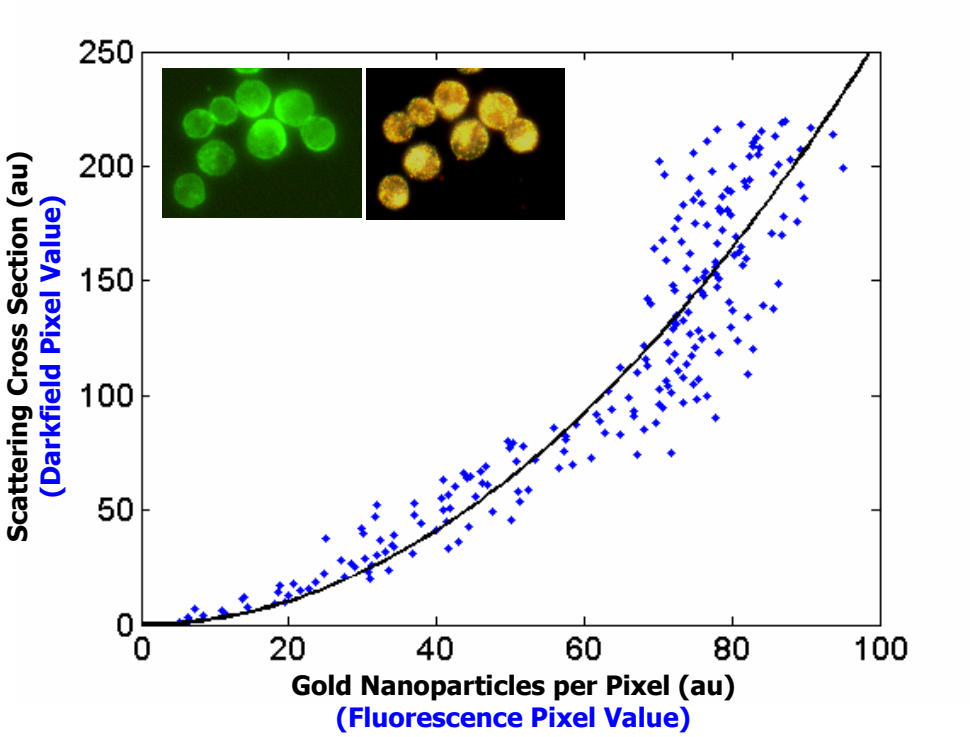

Figure 3.4 Labeling of cancer cells: quadratic dependence of total scattering cross section on the number of anti-EGFR gold conjugates. The inset displays fluorescence (left) and darkfield reflectance (right) images of A431 cells labeled with anti-EGFR antibodies conjugated to a fluorescein derivative and gold nanoparticles. The plot shows the relationship between the reflectance intensity from each pixel in the darkfield image and the fluorescence intensity from exactly the same pixel in the fluorescence image (•). The experimental data agree well with the theoretically predicted quadratic dependence of scattering cross-section on number of nanoparticle (R^2 = 0.85; solid curve). The observed variations in the intensity of the darkfield pixel values can be explained by the accuracy of the optical measurements with 8 bit CCD camera.

3.4.5 Electron Microscopy of Labeled Cells

The results shown in figures 3.1-3.4 are highly consistent with a nanoscale aggregation of gold particles on the cell surface. However, to independently confirm that this phenomenon is occurring, A-431 cells were labeled, dehydrated, fixed, and subjected to a critical point drying procedure, as outlined in the Materials and Methods. The critical point drying procedure occurs in a CO_2/Acetone system whereby acetone is converted from liquid to gas without a large change in surface tension. This allows for the cells to dry intact, without any surface tension-induced disturbances of the cell

surface [257]. After drying, the cells were imaged using a high angle annular dark field scanning electron microscope (HAADF STEM). This imaging modality detects scattered electrons (rather than the conventional transmitted component), and can 'tune' its detection angle for increased sensitivity to electron scattering from specific atomic species. This allows an image that has a heightened contribution from electrons scattered by gold atoms only, often referred to as Z-contrast [263]. A representative image is shown in figure 3.5. It shows the surface of A-431 cells labeled with 25nm gold particles conjugated to anti-EGFR antibodies (clone 29.1), as described in section 2.1. The particles appear as white circles, while the cell membrane appears as a more diffuse background. Note that some of the particles display a distinct "pairing" tendency, highly suggestive of the EGFR dimerization model of activation, although more definitive assays would be needed to convincingly determine the dimerization state.

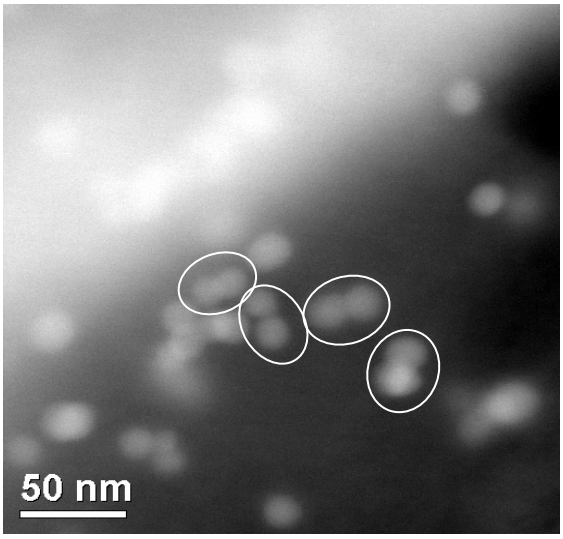

Figure 3.5 Z-contrast scanning transmission electron microscopy (STEM) of whole cancer cells labeled with anti-EGFR gold nanoparticles (A and B). Gold conjugates appear as white spheres. White circles in (*A)* highlight dimers of gold nanoparticles which reflect dimerization of EGFR molecules.

3.5 DISCUSSION

It is known that the optical properties of metal nanoparticles undergo dramatic changes when two or more particles are in close vicinity [191] to each other. These include an increase in scattering cross-section per particle and a red shift in the plasmon resonance frequency (color change). Recently, these properties were exploited to develop ultrasensitive assays *in vitro* [70, 71, 73, 264-266], as well as a mechanism for increased photothermolysis efficiency [267]. Some of the most promising directions in this area focus on exploiting plasmon resonance coupling between adjacent nanoparticles for DNA probe assays [71, 73, 266]. However, these phenomena have yet to be fully exploited for use in molecular imaging in living tissue. In an attempt to study the principles involved in the detection of EGFR on the cell surface, we used cancer cells labeled with anti-EGFR gold conjugates to demonstrate how these non-linear optical properties can translate into high contrast molecular imaging of cancer biomarkers in living cells.

As shown by electron microscopy, EGFR-bound gold nanoparticles on the cell surface display an aggregation effect suggestive of pre-endocytotic trafficking of EGFR into clathrin-coated pits [268], although more precise determinations of particle localization are investigated further in the next chapter. Overall, the protein-mediated nanoparticle aggregation results in plasmon coupling between gold bioconjugates, producing a spectral shift of more than 100 nm in light scattering of the nanoparticles. In addition, coherent scattering effects result in a quadratic increase in the total scattering cross-section of closely spaced nanoparticles. This occurs because an assembly of nanoparticles manifests an electric polarization in response to the incident electric field. The magnitude of this polarization is proportional to the magnitude of the incident field and also to the total number of nanoparticles. The scattered electric field is proportional

to this polarization, and therefore the scattered power and the scattering cross-section are proportional to the square of the number of the particles in the aggregate.

The combination of the plasmon red shift and the non-linear increase in the total scattering cross section of aggregates leads to a large increase in the scattering signal from labeled cells in the red optical region, with limits of resolution in the range of 100-500nm, depending on the magnification. This allows simple optimization of the excitation wavelength for detection of highly EGFR-overexpressing cells, even in the presence of isolated gold bioconjugates, resulting in more than an order of magnitude increase in remitted signal. Additionally, the large red optical shift in the plasmon resonances provides the possibility to decrease the contribution from the endogenous scattering of cells which is predominant in the blue spectral region. These results can serve as a basis for further investigations using more complex biological models that more closely resemble *in-vivo* tissue. Critical questions remain, however, as to the specific mechanisms by which the protein-induced plasmon coupling occurs within living cells. These include the role of EGFR dimerization, aggregation, endocytosis, as well as other trafficking events.

3.6 ACKNOWLEDGEMENTS

The author would like to thank Sonia Kumar for her excellent work in development and adaptation of the hydrazide conjugation protocol. Also, assistance from Dr. Miguel José-Yacamán's group for electron microscopy imaging is gratefully appreciated. Finally, the author would like to greatfully acknowledge funding from the NSF IGERT program, as well as from the National Cancer Institute.

CHAPTER 4:

EGFR Trafficking and Mechanisms of Nanoparticle Aggregation

4.1 ABSTRACT

We show that immuno-targeted gold nanoparticles are exquisitely sensitive to the nanoscale spatial arrangement of EGFR molecules in cultured A-431 cells. Darkfield imaging of cells maintained in a live imaging chamber show a clear spectral shift in scattering properties (easily visible in a color CCD camera) upon contrast agent binding to the cell surface. Interestingly, red-shifting of the nanoparticles' plasmon resonance occurs over a longer period of time (on the order of 30-60 minutes, depending on particle concentration and temperature), even after removal of excess particles from the surrounding solution. This likely indicates that endocytotic internalization of EGFR molecules is responsible for shifting nanoparticle aggregate plasmon resonance into the near infrared spectral regions. Transmission electron microscopy supports this claim. Finally, through temperature modulation, the aggregation state of EGFR-bound nanoparticles can be controlled for detailed spectral measurements. Statistical distributions of peak wavelengths from hyperspectral imaging data delineate different localization states, from primarily on the cell membrane, to early endosomal formation, and finally entry to mature lysosomes. These states are independently controlled via temperature.

4.2 INTRODUCTION

As the results from previous chapters indicate, the phenomenon of surface plasmon coupling is central to understanding the contrast enhancement properties of gold nanoparticles as EGFR-specific labels. These studies show a clear red-shifting of the

plasmon resonance on the cell surface relative to particles in solution. This, together with coherent scattering effects [200], produces optical signatures from cells which are redder and brighter than those seen in solution. This is supported by several highly controlled studies of particle *pairs*, whereby spectral shifts are measured as a function of particle size and spacing [71, 72, 191, 269].

The aforementioned data in cells are indicative of higher-order aggregation – i.e. many particles in close proximity to each other, not isolated particle pairs, as evidenced by the large spectral red-shift. Pairs of gold particles typically display spectral shifts of less than 10nm, while aggregates on the cell surface can show as much as a 100nm shift. While the discrete dipole approximation and T-matrix theory can give us good inferences as to what can be expected in these highly complex arrangements [194, 198, 199], a fully robust and generalized optical behavior theory of arbitrarily aggregated nanoparticle is still under development. As such, we must rely on experimental measurements to correlate the observed optical property shifts with the behavior of EGFR molecules in and on the cell.

This affords a good opportunity, however, to postulate causal relationships between what is known of EGFR signaling and trafficking behavior and the resulting optical signatures seen in the data. As has been elucidated over 25 years of molecular biological studies, EGFR can undergo several stages of compartmentalization during its life-cycle, depending on the cell type in question. Early studies found that clusters of EGFR formed on proliferating cells, and this clustering could be controlled by external parameters, such as temperature [129, 131]. While homo- and hetero-dimerization has since been found to be a mode by which tyrosine phosphorylation generally occurs [105], the role of receptor

clustering has been postulated to act as an organizational event closely tied to endosomal uptake, and eventual lysosomal degradation or recycling as an important part of the EGFR signaling and regulatory process [97, 135, 137, 138, 270-272].

4.3 MATERIALS AND METHODS

4.3.1 Anti-EGFR Contrast Agents

25nm gold nanoparticles were synthesized according the method by Frens [201], and conjugated using the dithiol-hydrazide bifunctional PEG linker (Sensopath Technologies, Inc.) described in the previous chapter. Briefly, anti-EGFR antibodies (clone 29.1.1, Sigma) were purified and oxidized for 30 minutes in 100mM $NaIO_4$, before being exposed to an excess of the bifunctional linker for an additional 30 minutes. This clone has been shown to not block ligand binding [255]. Non-reacted linker was removed via centrifugal reverse osmosis in a 100kD MWCO filter (Centricon). Gold nanoparticle conjugates were stored in 1x PBS at a particle concentration equal to twice that at which the original particles were synthesized at (approximately 2×10^{12} particles per mL).

4.3.2 Cell Culture and Labeling Procedure

EGFR overexpressing A-431 epidermoid carcinoma cells were grown in Dulbecco's Modified Eagle Media (DMEM), plus 10% FBS at 37°C in a 5% CO_2 atmosphere. This cell line has been extensively studied with regards to the behavior of EGFR both on the plasma membrane, and within the cytosol [83, 97, 133, 273, 274]. Adherent cells were cultured on 22mm square coverslips, and washed in phenolphthalein-free and serum-free serum prior to labeling to minimize receptor activation before labeling. Exposure to conjugates occurred for 30 minutes under mild agitation at 4°C, 25°C, and 37°C. To preserve the temperature-mediated EGFR organization, after labeling, cells were

immediately fixed in 10% buffered formalin for 15-20 minutes, and then extensively washed and stored in 1x PBS.

Cells labeled adherently in the imaging chamber were cultured on sterilized 40mm circular glass coverslips (Bioptechs, Inc.), and affixed in a custom designed imaging chamber. Adherent cells were labeled with a 1:4 mixture of 1x PBS/contrast agent and serum- and phenolphthalein-free media at 25°C that was injected into the chamber. The lower concentration was used to help reduce the background signal from unbound conjugates. Pure DMEM was subsequently injected in excess to clear unbound conjugates from the chamber volume.

4.3.3 Live Cell Imaging Chamber

A custom live cell imaging chamber was designed and machined out of 302-grade stainless steel. The system is shown in exploded form in figure 4.1. The assembly is comprised of three pieces: a central chamber, which contains the inlet and outlet ports, and two clamping pieces (upper and lower) that serve to compress the system, creating a water-tight chamber within. The perfusing fluid is allowed to flow through these small inlet and outlet channels, which are adapted on the outside of the central chamber to be compatible with a general Luer-type fitting for easy connect/disconnect. Two 40mm diameter coverslips (Bioptechs, Inc.) are placed in contact with the central chamber. To maintain a water-tight seal, O-rings (not shown) are placed in grooves, between the coverslips and the central chamber. To compress the O-rings, the top and bottom clamping pieces are attached to the central chamber via a set of 8 radial-symmetric screws on each face. Thus, the system can be easily closed to the outside environment. The addition of a sterile filter in the inlet stream prevents introduction of any microbial

contamination. A simple peristaltic pump (not shown) can provide fluid perfusion at very low flow rates (less than 0.1 mL per minute). The system can also incorporate a separate in-line heater (not shown) to increase the temperature of the perfusing fluid to 37°C. In addition, a set of four, 20Ω resistors are installed onto central chamber piece, which are controlled via a dual channel temperature controller. These allow the entire system to maintain elevated temperature for a closer approximation to *in-vivo* conditions. It is important to note, however, that pH control is not currently implemented, although the volume of fluid in the chamber results in relative stability for several hours, as evidenced by healthy cell appearance. For machinists drawings, including dimensions, refer to the Appendix.

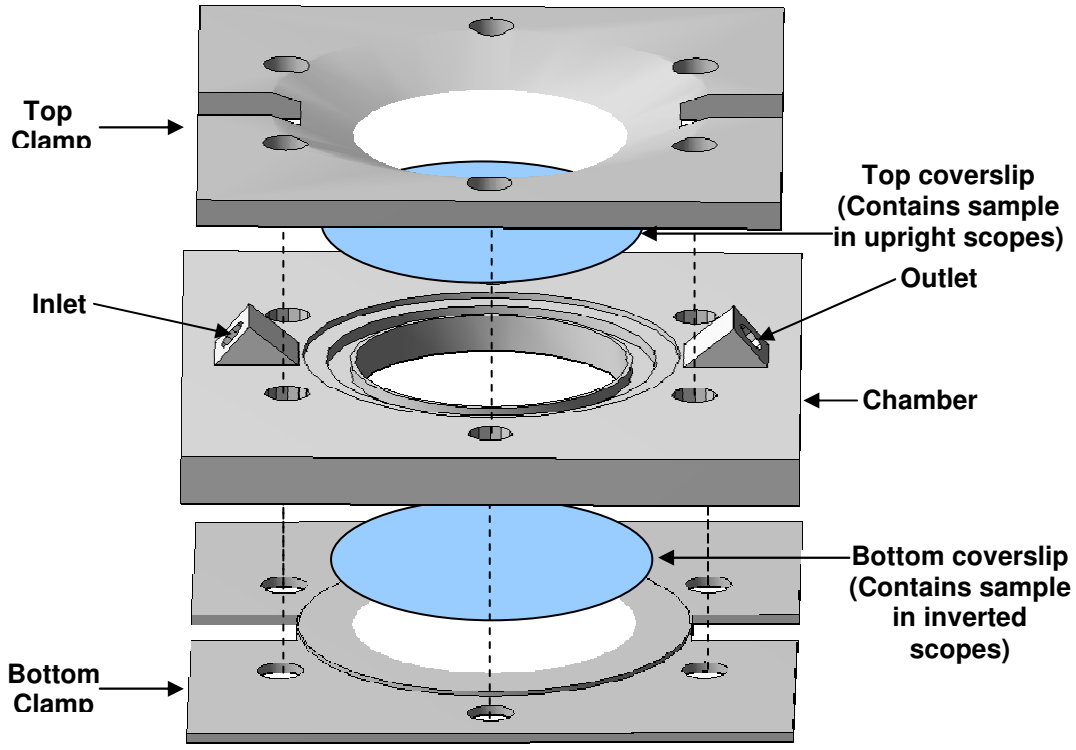

Figure 4.1. Exploded view of the custom imaging chamber used for live cell imaging experiments. The assembly contains three pieces machined from 302 grade stainless steel: (1) middle chamber, which contains the perfusing fluid with inlet and outlet ports, and two clamps (top and bottom) that serve to secure two 40mm coverslips in place. A water-tight seal is maintained by O-rings (not shown) placed between each coverslip and the central chamber assembly. The top and bottom clamps are also beveled for easier access of objectives and/or condenser lenses.

4.3.4 Darkfield Imaging

Imaging was performed using a Leica DM6000 upright microscope, equipped to image in brightfield (both transmitted and reflected), phase, darkfield (transmitted and reflected), and fluorescence modes, with an option for polarization sensitivity in all modes. Images of cells at low magnification (20x), were acquired using epi-illuminated darkfield imaging. In this setup, a 75W Xe light source illuminated the sample through a specialized Darkfield/Brightfield objective (Leica), with outer annular NA of 0.90-0.95, and images were collected through the inner annulus of the same objective, with a collection NA of 0.5. As stated previously, the separation of illumination and collection light allows the detection of only higher diffraction orders, and suppresses any specular reflections.

All darkfield images were acquired using a 12-bit ultra-sensitive CCD camera (Q-imaging, Retiga EXi), equipped with an RGB automated LCD filter wheel for color capability. This camera has a pixel resolution of 1360x1036, corresponding to approximately 3 pixels/μm, which is within the diffractin limitied regime.

4.3.5 Transmission Electron Microscopy

Adherent cells were cultured on sterilized discs of Aclar polymer. After labeling, cells were fixed in 10% buffered formaldehyde, followed by cold 2% glutaraldehyde, and then dehydrated in separate ethanol and acetone series. Samples were then embedded in a matrix of epoxy (Embed® 812), and sectioned in a Leica Ultracut UCT cryotome into *c.* 100nm slices. Samples were imaged using a Philips EM 208 Transmission Electron Microscope.

4.3.6 PARISS Hyperspectral Imaging Device

In order to evaluate the full spectral profile at each pixel in the darkfield images, hyperspectral imaging was performed on cells using a slit/dispersion system (Lightform, Inc. PARISS®), as described in section 2.6.4. Briefly, the sample is placed on a computer-controlled stage which is laterally translated with precise piezo-control. Successive "slices" of the sample are then projected through a 25µm slit located in the detection path, and focused through a series of curved mirrors and a patented dispersive element. This produces a two dimensional image onto a CCD chip, whereby the y-direction contains spatial information, and the x-direction contains spectral information [222]. This process is repeated for each "slice" in the image. The basic operation principle is shown in figure 4.2

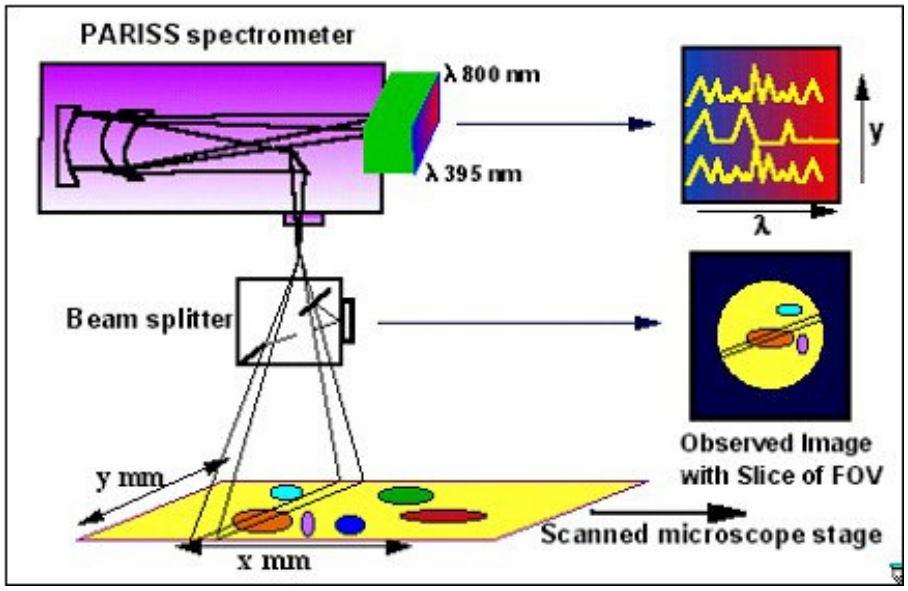

Figure 4.2 Operation of the PARISS® hyperspectral imaging device. The sample is translated laterally under an objective, and a slit allows serial passage of thin "slices" of the image through to a dispersive element, which projects a 2D data set onto a CCD. The y-direction contains spatial information, and the x-direction contains the spectral data. A beamsplitter below the dispersion elements also allows conventional 2D spatial imaging of the field of view to assist in orienting the sample.

The PARISS system utilized in these studies has a spectral range of 350-850nm, although the optical components in the Leica Microscope, as well as the light sources limit practical performance to between 425 and 775nm. The spatial resolution of the system is determined by the optical slit in the detection path, which was set to 25µm. At 20x magnification, this corresponds to a pixel resolution of 1.25µm. Current progress is underway to introduce a smaller slit for improved resolution, although care must be taken to optimize this against overall signal intensity. The collection of scattering spectra requires the normalization of the acquired data with the illumination spectrum of the lamp. We used either a microscopically clean electroplated aluminum mirror, imaged in brightfield reflected mode, or a calibrated lambertian substrate (Labsphere, Spectralon®), imaged in darkfield mode under de-focused conditions, to capture the xenon lamp spectra.

4.3.7 Data Analysis

Because of the three-dimensional nature of hyperspectral data, the method used for analysis of images becomes important. There is no single way to visualize the sample imaged using this system, so a set of algorithms was developed to maximize flexibility in extracting various relevant information. These were implemented in Matlab (see Appendix). The aim of the algorithms in general is to reduce the dimensionality of the data from three to two dimensions for easier visualization. There are three main ways to do this. First, the intensity of the sample at a given wavelength can be viewed. While instructive, this is mainly used to gauge the relative intensities of a sample vs. the background, or a labeled vs. unlabeled samples at a particular wavelength. This representation is akin to simply imaging the sample with a narrow illumination bandpass

filter. Conversely, the data can also be partitioned such that spectra from a particular pixel (or group of pixels) are displayed. This is useful in evaluating the precise spectral profile of part of the sample, but clearly the loss of spatial information over the entire image is limiting.

A third method used for representing the data involves creating an image of the sample that contains a characteristic piece of information about the spectra at each pixel. Most relevant to evaluating plasmon resonance coupling would be to display the extent of the plasmon resonance red-shift at each point in the image. As such, an algorithm has been developed that identifies a peak in each pixel's spectra (indicative of a nanoparticle contained within the spectra), and at what wavelength the peak occurs. This "peak wavelength image" can give valuable information as to the extent of plasmon coupling with sub-cellular resolution.

4.4 RESULTS

4.4.1 Monitoring Nanoparticle Binding and Aggregation Dynamics

EGFR over-expressing A-431 epidermoid carcinoma cells were cultured on 40mm diameter coverslips (Bioptechs), and placed in the imaging chamber at 25°C. A 1:4 mixture of contrast agents in 1x PBS and phenolphthalein-free DMEM was perfused into the chamber, and darkfield reflectance images were acquired at approximately 4 frames per minute for 40 minutes. This supplies ample sampling to gauge the overall signal intensity/chromatic changes on cells (although may not be sufficient to measure the movements of single particles or aggregates within the cell. Figure 4.3 indicates the dynamic change seen in the field of view over time as the anti-EGFR gold nanoparticles are allowed to bind to the adherent cells. In (A), cells are shown immediately following

injection of the contrast agent – media mixture. The signal was observed to be primarily blue, consistent with the natural scattering properties of cells. Close inspection does reveal isolated areas of green – which may indicate some initial particle binding before image acquisition began. However, in (B), images are shown 20 minutes after initial exposure to contrast agents, and in (C), images are shown 40 minutes after exposure.

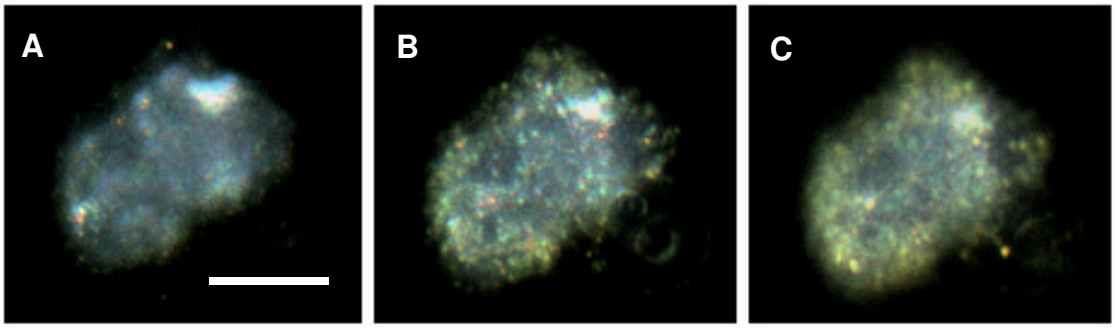

Figure 4.3 Darkfield images of A-431 cells during the labeling process captured using the live imaging chamber. In (A), the native scattering from the cells are seen immediately following contrast agent injection. In (B), a significant increase in the overall green signal is seen 20 minutes later. Part (C) shows a more complete labeling pattern, approximately 40 minutes after contrast agent application. Images were acquired at 20x objective magnification. Scale bar is c. 10μm.

As can be seen, the scattering properties change markedly, with a progressive shift in the detected signal to the green spectral region. This result was highly repeatable, observed in greater than 50% of cells in the field of view. Due to the large background from unbound nanoparticles in solution it was necessary to subtract the background from each image using a rolling ball image processing algorithm to optimize signal-to-background (which originally was 3-4). It is interesting to note that, at least initially, darkfield imaging of cells does not reveal the pronounced red-shift seen in previous samples. Inspection of the above images seems to suggest that the most of the particles are present on the cell surface. In addition, it is apparent that the labeling dynamics are somewhat slower due to the fact that the cells are affixed to a surface, and not in suspension. Also, the contrast agent was introduced at approximately 25% of the

concentration used in the previously described studies. However, upon longer-term imaging, the bound nanoparticles show a progressive red shifting, as shown in figure 4.4. At left (A) shows cells after labeling for 60 minutes and subsequent clearance of excess unbound conjugates. Note that the scattering signal attributable to nanoparticles is green to yellow, consistent with images shown in figure 4.3. At right (B), another image was acquired after a further 60 minutes had transpired. The scattering signal attributable to nanoparticles displays a prominent red-shift over this relatively lengthy period of time. Cells appeared to remain healthy, as evidenced by the presence of filopodia, although future experiments will need to confirm cell viability more rigorously. The red-shifting effect was highly reproducible, and further characterization and modulation will serve to elucidate the specifics of this process.

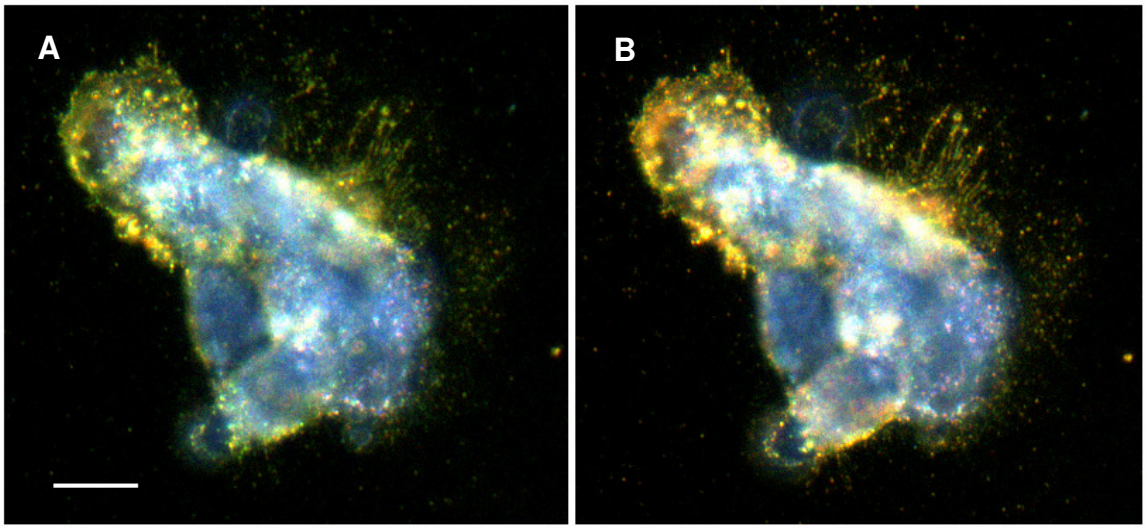

Figure 4.4 Longer term aggregation of anti-EGFR gold nanoparticles. At left, (A) shows a reflected darkfield image of A-431 cells, acquired after initial labeling and subsequent clearing of unbound conjugates from the imaging chamber. Note the predominantly green-yellow character of the nanoparticle signal. The image at right (B) shows the same field of view after an additional 60 minutes, displaying a noticeable, longer-term red shift in the overall signal. Scale bar is 20μm.

4.4.2 Transmission Electron Microscopy

Of critical importance is determining what causes this red shift over time. As has been previously described, the compartmentalization of EGFR generally follows two distinct aggregation steps: First, EGFR clusters into clathrin-coated pits on the cell surface [134], as a precursor to the secondary step of endocytosis, and lysosomal sequestration and degradation [137] in a cell-cycle dependent manner. To independently evaluate the nanoscale arrangement of nanoparticles within the sample, cells were grown on Aclar polymer discs, labeled as described, fixed and prepared for transmission electron microscopy (TEM).

Figure 4.5 illustrates representative TEM images of A-431 cells labeled with anti-EGFR contrast agents at 10^{12} particles per mL at room temperature. At left (A), the plasma membrane is shown of a cell exposed to conjugates for 10-15 minutes before immediate washing and fixation. The image shows that most of the nanoparticles are at or near the plasma membrane, and appear to be organized into mainly two-dimensional aggregates, as evidenced by particle "chains" seen in cryosections image projections. In contrast, the image at right (B) shows the plasma membrane boundary for another A-431 cell exposed to contrast agents for 60-70 minutes before washing and fixation. In this case, nanoparticle arrangements appear to include endosomal vesicles, and are organized into three-dimensional aggregates, with particles lining the inner surface of the endosomes. This data seem to suggest that longer-term reorganization of EGFR-bound nanoparticles does result in optical property shifts.

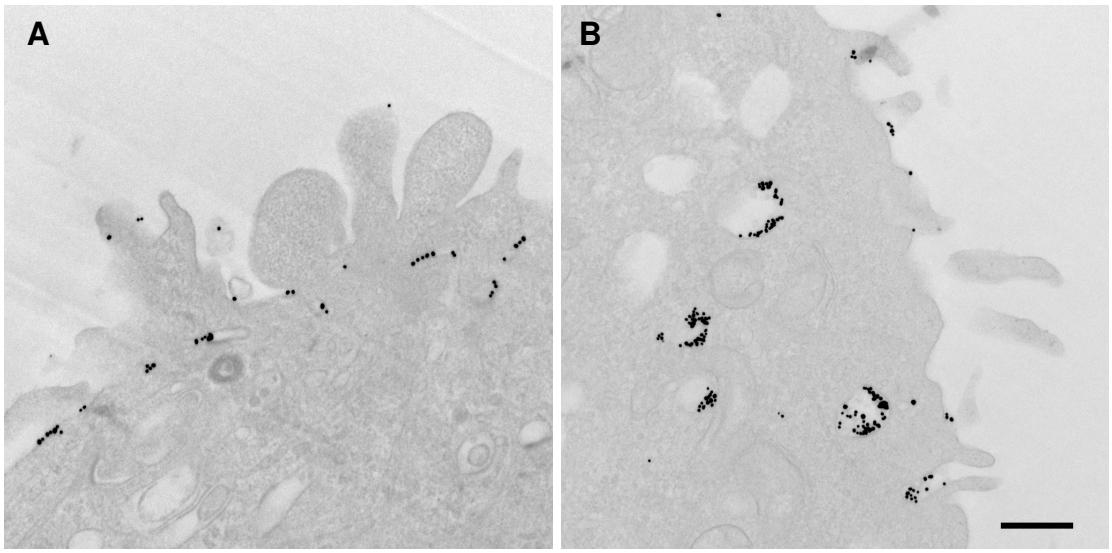

Figure 4.5 Transmission Electron Microscopy (TEM) images of A-431 cells labeled with anti-EGFR contrast agents for 10 minutes (A), and 75 minutes (B) before being immediately fixed in 10% buffered formalin. Note that in (A), particles are concentrated on or near the surface, largely in "planar" or two-dimensional aggregates. In (B), particles are mainly concentrated in endocytotic vesicles in a three-dimensional aggregate. Scale bar is 200 nm. The author would like to gratefully acknowledge Nathan Harrison for sectioning and imaging of these samples. Scale bar is c. 500nm.

4.4.3 Modulating Labeling Temperature to Control Aggregation State

To evaluate this effect under more controlled conditions, the process of endocytosis in labeled A-431 cells was modulated by manipulating the temperature at which cells were labeled. It has been observed that endocytosis of EGFR molecules is significantly inhibited at 4°C, proceeds incompletely at or near room temperature, and forms mature lysosomal vesicles only at 37°C [97]. As such, 3 cell samples were exposed to anti-EGFR contrast agents (10^{12} particles per mL) for at 4°C, 25°, and 37°C, respectively, for 60 minutes. After this time period, cells were immediately washed in cold 1x PBS and fixed in 10% buffered formalin to preserve the temperature-mediated nanoparticle arrangement. Additional observations may be necessary to evaluate if fixation alters the particle arrangement on the cells, but initially only relative changes with temperature are considered. Figure 4.6 shows examples of darkfield imaging of each of these three

samples. Single cells are shown in the field of view to emphasize the sub-cellular appearance and localization of the nanoparticles, but results were highly repeatable from cell to cell (more than 10 cells from each temperature were analyzed). In (A), at left, a cell is shown that was exposed to contrast agents for 60 minutes at 4°C. Notice that the signal attributable to nanoparticles is localized almost wholly to the cell periphery, and does not display a dramatic red shift relative to isolated particles. In (B), however, a cell is shown that was exposed to conjugates for the same period of time, but at 25°C. In this case, a marked scattering signal shift as well as noticeable increase in overall signal is observed both on the cell exterior and interior. Finally, the image at right (C) indicates the overall appearance of cells labeled at 37°C. The signal in this sample is clearly red shifted relative to both lower temperature samples. In addition, the particles appear mainly localized away from the cell periphery, and are concentrated in the areas surrounding the nucleus, consistent with lysosomal degradation (although confocal

imaging would confirm this more rigorously). Identical results were seen in >90% of cells in the field of view at each temperature.

4.4.4 Hyperspectral Imaging of Cells Labeled at Different Temperatures

In addition to conventional RGB image capture, hyperspectral imaging, using the PARISS® system (Lightform, Inc.), was performed on each of the samples to quantitatively evaluate the temperature-induced plasmon coupling trend. Refer to section 4.3.6 for principles of operation for this instrument. Complete spectral profiles were captured of 2-3 fields of view for each temperature point, each containing 5-15 cells. The data was then analyzed in a pixel-by-pixel fashion to identify peaks in each pixel's spectrum. The spectra were first filtered by using a moving average algorithm, with a window size of 3nm to remove high frequency noise in the signal. Peaks were identified using a well-known algorithm of finding local maxima (refer to Appendix for details). Peaks between 515nm and 750nm were considered, to avoid noise artifacts. If the peak identified was above a threshold value (set to 10% higher than the measured background

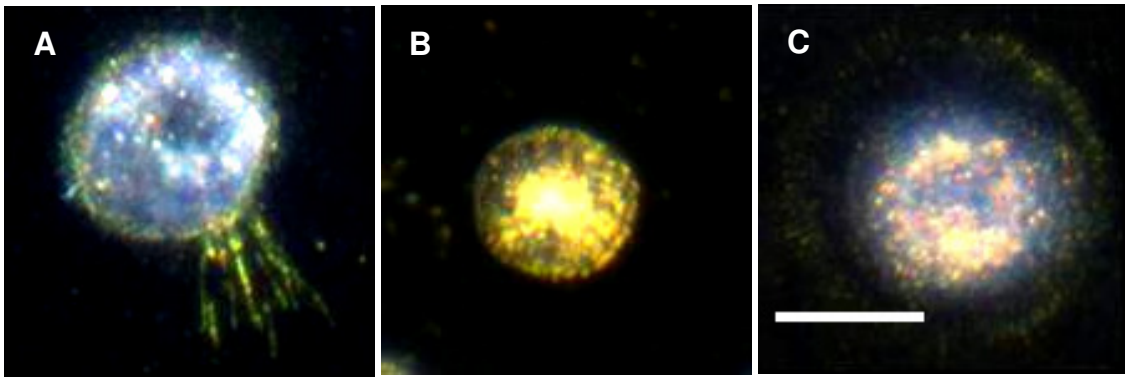

Figure 4.6 Darkfield imaging of A-431 cells labeled with EGFR contrast agents at 4°C (A), 25°C (B), and 37°C (C), each for 60 minutes. At 4°C (A), nanoparticles appear to be localized near the cell membrane, and display a mainly green scattering profile. At 25°C (B), particles appear yellow, with some evidence of internalization. Finally, at 37°C (C), particles appear mainly within the peri-nuclear areas of the cell, and display a red shifted scattering profile relative to samples shown in (A) and (B).

scattering level), that pixel's position is given a peak wavelength value. If no peak was found within the given wavelength range, the spectrum was assumed to be essentially monotonically decreasing, in accordance with accepted intrinsic scattering behavior for cellular components [152], and given a peak scattering value of 400nm (the shortest reliable wavelength limit of the instrument). If a particular pixel's spectrum did not exceed the threshold value, it was assumed to be background signal, and identified by a black (RGB = 0,0,0) pixel value. Extensive previous testing and comparison of the algorithm against manual inspection of the data established its reliability. Representative example peak wavelength images of single cells are shown in Figure 4.7 (A), (B), and (C), corresponding to cells labeled for 1 hour at 4°C, 25°C, and 37°C, respectively. These images indicate an increase in plasmon resonance red-shifting seen as a function of labeling temperature. Also note that signals attributable to particles are mainly confined to the cell periphery for those cells labeled at 4°C – as the green signal is seen as a ring around the cell. These signals seem to occupy most or all of the cells labeled at 25°C, and seem to be primarily internalized in the 37°C case – although confocal imaging or similar sectioning technique will prove this more conclusively. Similar analysis was done for 10-20 cells from each of the three labeling temperatures, and the results were organized into a histogram, seen in Figure 4.7(D). This reveals a clear shift in the peak wavelength distribution as a function of temperature. Also of note is the dramatic increase in distribution width seen when labeling at 37°C. A biological explanation for this behavior is not entirely clear, but it has been shown that the endocytosis to lysosomal pathway is only fully functional at 37°C [97], so the wide distribution of peak wavelengths may indicate a wide distribution of endosomal vesicles within the cell.

Quixotically, however, there seems to be a larger population of spectra with far red-shifted spectra a 4°C than at 25°C – although this is not immediately apparent in the RGB images or hyperspectral images. Future work will attempt to assign biological/physical meaning to this apparent inconsistency. The average and median wavelengths are summarized for each temperature in Table 4.1 below, and illustrate the overall red shifting trend.

Table 4.1 Average and median peak wavelengths for each labeling temperature.

	Labeling Temperature		
	4℃	25℃	37℃
Average Peak (nm)	566	573	607
Median Peak (nm)	551	573	585

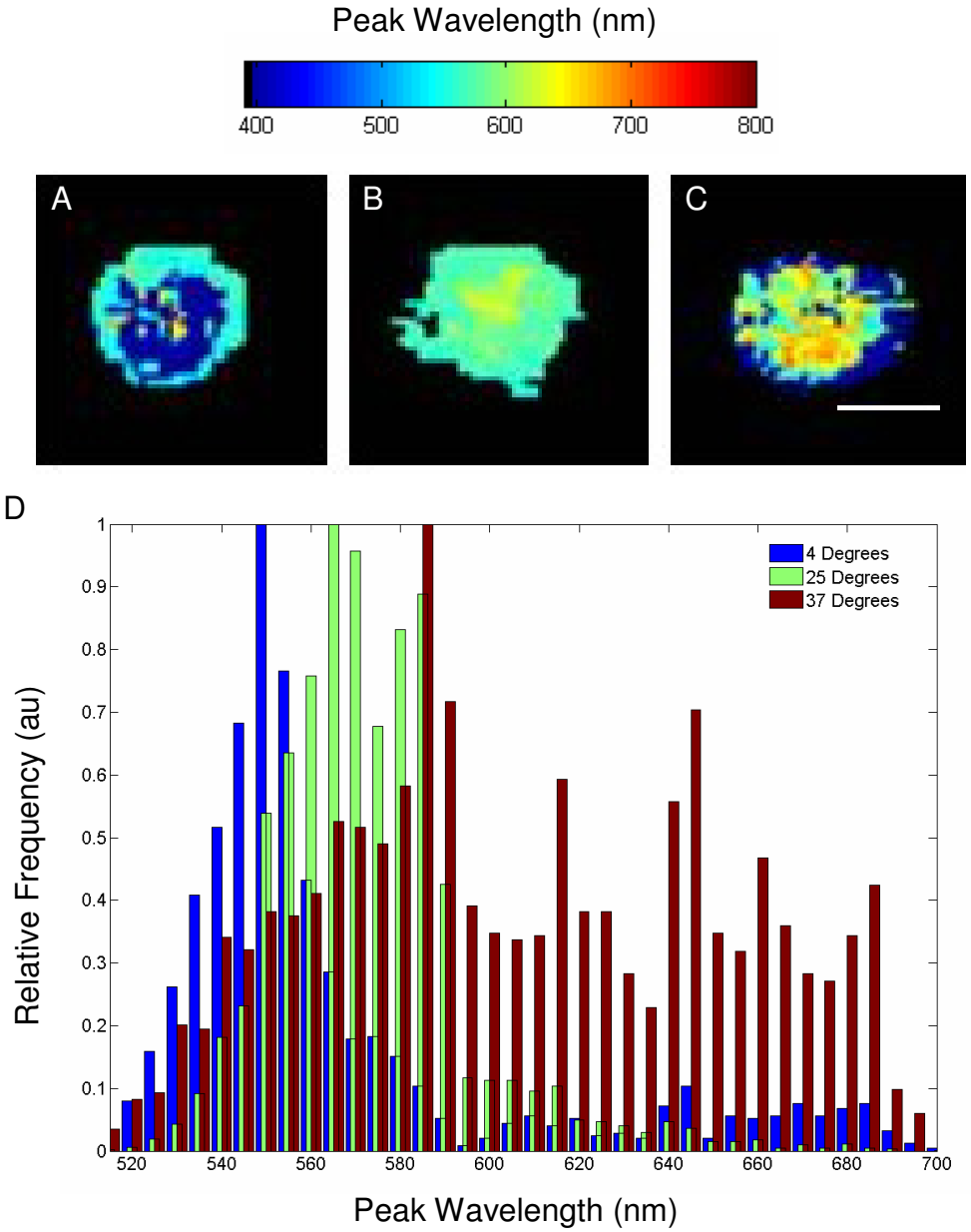

Figure 4.7. Hyperspectral imaging of cells labeled at different temperatures. Peak wavelength images (A-C), of representative cells are shown, labeled at 4°C, 25°C, and 37°C, respectively. In these images, each pixel value corresponds to the detected peak scattering wavelength at that pixel. Images clearly show increased red shifting of plasmon resonances concomitant with increases in temperature. Also, peaks between 500-700nm are seen mainly on the cell periphery in (A), throughout the cell in (B) and mainly in the peri-nuclear areas in (C). Scale bar is 10μm. Histograms of 10-20 cells, labeled at each of the three temperatures are shown in (D). Note the distribution shifts between each temperature, and also the distinct broadening of the distribution seen at

4.5 DISCUSSION

It is clear from these studies and previous that immuno-targeted gold nanoparticles are quite sensitive to the nanoscale arrangement of the EGFR molecules to which they are attached. This arrangement – in reality a dynamic *rearrangement* of biomolecules – and the resulting optical property changes opens up further possibilities for immuno-targeted gold nanoparticles. On the one hand, biologically directed clustering and movement of EGFR-conjugate complexes can allow the imaging of *in-situ* molecular trafficking in real time with a simple optical setup. While many imaging studies to date have elucidated EGFR trafficking mechanisms [83, 143, 272], there is a dearth of methods that are sensitive to nanometer level organization in living cells. At the same time, these molecular mechanisms give greater insight into the contrast enhancing potentials and limitations for application to clinical uses of this technology.

As was discussed in Chapter 3, plasmon coupling is a major contributing factor for enhancing contrast when imaging EGFR expression in cell cultures. However, it seems clear from the studies contained in this chapter that the extent of plasmon coupling is intricately entwined with the trafficking patterns of EGFR. As was seen when monitoring the shorter-term labeling dynamics, extensive plasmon coupling does not occur immediately upon nanoparticle binding to the cell surface. Even when using A431 cells, whose EGFR expression level is greater than 10^6 molecules per cell [274], extensive plasmon resonance shifting is not seen on the cell surface. This expression level corresponds to an average EGFR-EGFR distance of less than 40nm – however data has shown that less than half of receptors are ultimately labeled (data not shown), and this is a highly time- and concentration-dependent process. Rather, it it appears the endocytotic pathway which creates conditions for much higher order aggregation [135,

138, 143, 271], as well as aggregation in three dimensions, as evidenced by optical imaging, and more rigorously shown via TEM images. From an electrodynamic point of view, this would be expected: nanoparticles in a two-dimensional aggregate do not have the same number of nearest neighbors as do an equal number of equally spaced particles arranged in three dimensions. Hyperspectral imaging shows quantitatively that plasmon red-shifting can indirectly be controlled by temperature modulation – a controller of the endocytosis pathway.

From a biological and clinical point of view, the detection of EGFR dimerization and activation remains an attractive goal, but as the data suggests, EGFR activation and trafficking events are dynamic processes that serve to modulate cell regulatory mechanisms [271]. Future work with immuno-targeted gold nanoparticles may include efforts to isolate membrane vs. endocytotic aggregation more clearly via interference with cell cytoskeletal properties. Two-dimensional clustering has been observed in membrane preparations without actin or microtubule components [131]. This will aid in ongoing theoretical studies whereby spectral data and spatial arrangement of particles can be related in both a forward and backward model. In the end, a holistic view of the EGFR life cycle should be attainable using metal nanoparticles.

4.6 ACKNOWLEDGEMENTS

The author would like to thank Kyle Chai for his hard work in helping design and fabricate the custom imaging chamber. In addition, sample preparation and TEM imaging by Nathan Harrison is gratefully acknowledged. Also, thanks go to Dr. Jeremy Lerner (Lightform, Inc.) for helpful discussions, as well as aid in pre-processing

hyperspectral imaging data. Finally, the author would like to acknowledge funding from the NSF IGERT program, as well as from the National Cancer Institute.

CHAPTER 5

Detection of EGFR Expression in Complex *In-Vitro, Ex-Vivo* and *In-Vivo* Biological Models*

5.1 ABSTRACT

Results from the previous two chapters aim to identify the basic principles and mechanisms for establishing the feasibility of using immuno-targeted gold nanoparticles as molecular specific labels for EGFR over-expressing cells. In this chapter, these results are expanded upon by applying the same scheme in more complex biological models. The approach for this work relies upon testing nanoparticle imaging in models of progressively increasing complexity to identify possible strategies for, and barriers against, eventual clinical implementation.

We show that, with the aid of the tissue permeabilizer dimethyl sulfoxide (DMSO), immuno-targeted gold nanoparticles can be delivered through homogeneous and heterogeneous three-dimensional tissue phantoms, to a depth of at least 300μm. The heterogeneous tissue phantoms serve to indicate that the contrast agents retain their molecular specificity in a highly dense biological environment. Further, gold nanoparticle conjugates are effectively delivered in abnormal *ex-vivo* cervical cancer biopsies, although delivery was reduced to the superficial *c.* 100-150μm in normal samples, presumably due to the increased tissue permeability seen with progression of carcinogenesis. Overall, we show an increased normal to abnormal signal intensity ratio between paired biopsy samples as the clinical grade of dysplasia worsens. As a good indicator of the efficiency of nanoparticle delivery, we also show an increase in overall

* Contents of this chapter have been published in *Cancer Res.* **63**, pp. 1999-2004 (2003) and *J. Biomed. Opt.* ***13*** *(2007), (in press).*

scattering in confocal images as a function of increasing depth in the epithelium – consistent with literature paradigms that indicate highest EGFR expression nearest the basal layers. We show examples of *in-vivo* EGFR imaging in the hamster cheek pouch model of oral carcinogenesis. Although results were not always repeatable, we demonstrate that a *c.* 10-fold increase in confocal image signal between normal and abnormal tissue is possible, dramatically improving on values previously reported for EGFR imaging in the same oral cavity model [250]. Finally, preliminary data is shown that indicates that gold nanoparticles may be used to identify metastatic neoplasms found in cervical sentinel lymph nodes in advanced cases of oral cavity cancer. EGFR over-expressing cells were detected using confocal reflectance microscopy in a test case of metastatic oral cavity carcinoma, and confirmed by pathological diagnosis. This opens new avenues for medical applications of immuno-targeted gold nanoparticles.

5.2 INTRODUCTION

The *in-vivo* molecular characterization of disease, especially cancer, remains a critical task in bringing to fruition the concept of "individualized medicine" [275]. Determining key elements of a patient's genetic and proteomic profile, especially in abnormal tissues, holds the promise of vastly improved treatment regimens and better overall patient outcome. While a multitude of comprehensive strategies are being explored, the utilization of nanomaterials in conjunction with optical imaging is proving to be a powerful approach [245, 264, 276-280]. This generalized strategy relies on four basic components: (1) optically active nanomaterials, (2) cheap, portable, three-dimensional, real-time imaging tools, (3) effective targeting and delivering capability and (4) realistic,

reproducible, and highly characterized biological models in which to test various approaches. Figure 5.1 graphically illustrates this multi-component approach.

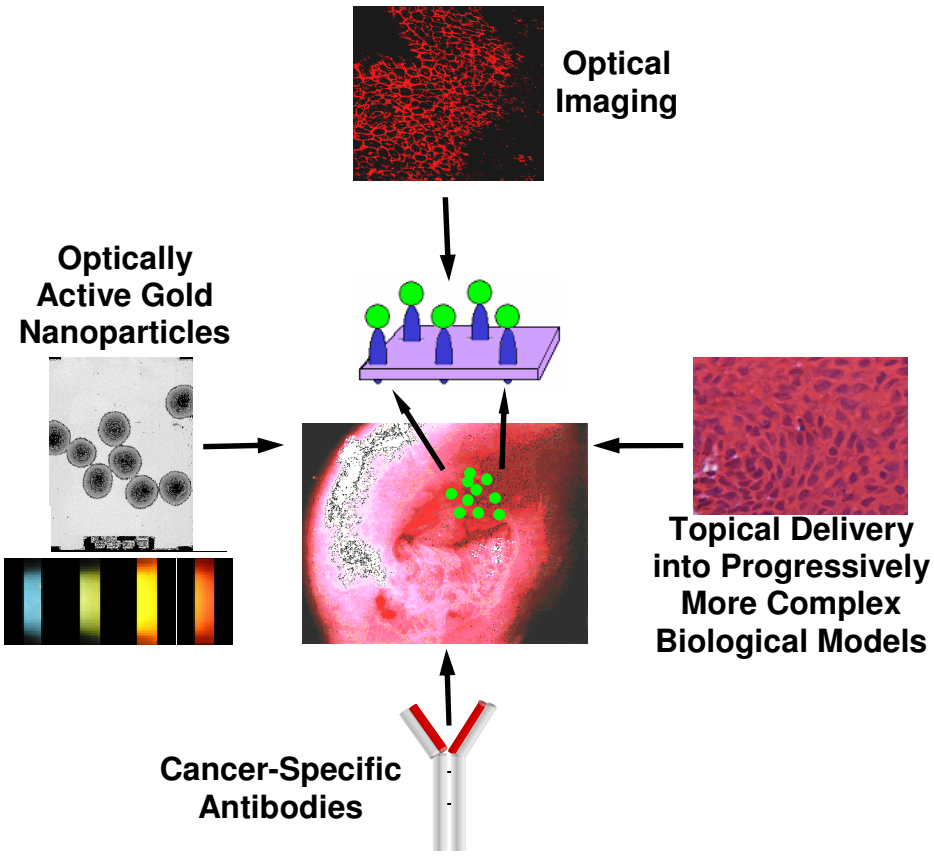

Figure 5.1 Conceptual approach to development of non-invasive molecular imaging of epithelial carcinogenesis is based on synergy of: optically active gold nanoparticles; cancer specific probe molecules; real-time optical imaging; and topical delivery formulations.

Numerous varieties of optically active nanomaterials have already been described in the case of quantum dots (qdots) [22-24, 82, 83, 180, 181] and plasmonic particles [30, 32, 63, 70, 71, 242, 281], and demonstrate the intense interest in development and application of mesoscopic materials for molecular-based bioimaging applications. While utilizing different mechanisms for signal generation, both qdots and plasmonic nanoparticles can be used to produce high-quality molecular-specific information in real time. In addition, the past decade has seen the development of a number of optical

microscopic techniques to image living tissue with sub-cellular resolution. Vital microscopies, such as optical coherence tomography (OCT) and reflectance confocal microscopy (RCM) image reflected light, thereby providing a detailed three-dimensional picture of tissue microanatomy without the need for physical sectioning [53, 145]. These technologies provide excellent spatial resolution (1 - 10 microns) with penetration depth ranging from 300 microns to 1-2 mm, depending on tissue composition, illumination wavelength, and detection scheme. These systems are portable and inexpensive compared to other high resolution imaging technologies such as MRI or micro-CT; as such they are well-suited for early screening and diagnosis of superficial disease. By themselves, however, OCT and RCM mainly provide images of tissue microanatomy, and their ability to image molecular changes associated with carcinogenesis is limited.

In an effort to develop a means for molecular specificity to be used in *in-vivo* reflected light microscopy (such as OCT and RCM), this chapter demonstrates the use of gold nanoparticles targeted to EGFR and applied in several biological models of pre-cancer and cancer. As noted previously, gold nanoparticles have been extensively used as molecular specific stains in electron microscopy [68, 282]. As result, the fundamental principles of interactions between gold particles and biomolecules have been thoroughly studied. Using this knowledge, as well as results and principles developed from the previous two chapters, the application of immuno-targeted gold nanoparticles is presented and discussed. We demonstrate the application of gold bioconjugates in several biologically relevant models of cancer with increasing complexity. Homogeneous and heterogeneous engineered tissue constructs, three-dimensional cell cultures that mimic major features of epithelial tissue [283, 284], were explored. We

prepared engineered tissue constructs consisting of densely packed, multiple layers of EGFR-positive and negative cells atop a collagen stroma. Following this, we show the application of contrast agents in normal and neoplastic fresh *ex-vivo* cervical biopsies, subcutaneously injected tumors in an immuno-deficient mouse model, human cervical lymph nodes of the head and neck as well as an *in-vivo* hamster check pouch model.

5.3 MATERIALS AND METHODS

5.3.1 Anti-EGFR Contrast Agents

25 nm gold nanoparticles were synthesized via sodium citrate reduction of gold tetrachloride (Sigma), as described in [201]. The conjugates of gold nanoparticles with anti-EGFR monoclonal antibodies were prepared using the method that was originally developed for preparation of gold immunostains for electron microscopy (18, 19). Briefly, 0.1 mg/mL of anti-EGFR antibodies (clone 225, Neomarkers or clone 29.1, Sigma), in a 40 mM HEPES buffer, pH 7.4, were mixed for 20-30 minutes with an equal volume of gold nanoparticles at approximately 10^{12} particles per mL. Conjugates were centrifuged at 3000 x rcf for 1-1.5 hours in the presence of 1% PEG and re-suspended at *ca.* 2 x 10^{12} particle concentration in a PBS buffer, pH 7.4 containing 1% BSA and 0.2% PEG. Bifunctional contrast agents were synthesized via a monoclonal antibody labeling kit (Molecular Probes) to attach fluorescein or Alexa Fluor 647 dye to purified antibodies via a succinimidyl ester reaction that forms linkages between the dye and primary amines on the antibody. Then, fluorescently labeled antibodies were conjugated with gold nanoparticles as described above.

5.3.2 Cell Cultures

Cells were cultured in Dulbecco's Modified Eagle Media (DMEM) (SiHa, MDA-MB-435) or MEM (MDA-MB-468) plus 10% FBS and grown at 37ºC in 5% CO_2. Cells were harvested via exposure to EDTA-trypsin for 5-10 minutes at 37°C, collected, centrifuged at c. 200 x rcf for 3-5 minutes, aspirated, and re-suspended in phenolphthalein-free media before imaging so as to reduce optical absorption artifacts.

5.3.3 Preparation of Three Dimensional Epithelial Tissue Constructs

For the homogeneous epithelial tissue constructs (tissue phantoms), SiHa cervical cancer cells were harvested as described and re-suspended in a 1mg/mL buffered (pH 7.4) collagen solution (Roche) at a concentration of approximately 80-100x10^6 cells per mL. A 200-500μm thick disk of the cell/collagen mixture was coated onto a permeable membrane 24-well insert (Transwell, Corning) and left to proliferate overnight in the incubator [284]. For the heterogeneous tissue phantoms, MDA-MB-468 and MDA-MB-435 cells were first cultured, harvested, and incubated with membrane permeable derivatives of fluorescein and seminaphthorhodafluors (SNARF) (Molecular Probes, Invitrogen), respectively, in DMEM for 1 hour and washed. The dyes serve to independently confirm each cell's identity.. The dyes are rendered membrane permeable via a chloromethyl group that is enzymatically cleaved upon entering a viable cell. Thus, once in the cytosol, the dye becomes membrane impermeable, and does not exit the cell. These two cell lines were chosen due to their similarity in organ site and morphology, but extreme difference in EGFR expression level A 1:1 (v/v) mixture of the two cell lines was suspended in a collagen solution as described above, and the phantom was prepared as before. In general, phantoms were topically exposed to 100μL of contrast agents (at *ca.* 10^{12} particles per mL) in a 1x PBS solution containing 10% DMSO for 30 minutes,

briefly washed in media, and transversely sectioned using a Krumdieck slicer before imaging.

5.3.4 Balb/c Nude Mouse Model

Adapting the protocol in [285], immuno-deficient Balb/c nude mice were anesthetized in ketamine, and intraperitoneally injected with approximately 2 aliquots of 0.1 mL of a suspension of SiHa cells in matrigel (BD Biosciences) at a concentration of c. 10^6 cells/mL in both sides of the mammary fat pad.. Mice were then housed for up to 6 weeks while tumors proliferated. When tumors reached a nominal diameter of approximately 5mm, mice were sacrificed via ketamine overdose and cervical dislocation and a skin flap was exposed in the mammary fat pad to reveal both tumors, and tumors were surgically removed. One tumor was placed in a solution of 25nm gold nanoparticles conjugated to anti-EGFR monoclonal antibodies (clone 29.1.1, Sigma) which were suspended in a 10% DMSO in 1x PBS solution for 45 minutes at room temperature. The other, control tumor, was placed in a 10% DMSO in 1x PBS solution only, and then both were imaged.

5.3.5 Human Cervical Biopsies

Clinically normal and abnormal cervical biopsies were obtained from consenting women seen at the Department of Gynecologic Oncology, M.D. Anderson Cancer Center. Biopsies were placed in chilled DMEM and later embedded in a 3% agarose gel such that only the epithelial surface was exposed. 200μL of contrast agents (at ca. 10^{12} particles per mL) in 1x PBS containing 10% DMSO (v/v) were applied to the surface for 45 minutes at room temperature. Then, biopsies were transversely sectioned and imaged.

After imaging, samples were placed in 10% formalin and submitted for histological evaluation.

5.3.6 Hamster Cheek Pouch Model

The Hamster check pouch model remains a well characterized model of oral cavity carcinogenesis [286]. 10 Golden Syrian Hamsters were treated 2-3 times weekly with a 0.5% solution of dimethyl benz(α)anthracene (DMBA) in mineral oil on the right mucosal side of the cheek pouch under the supervision of a small animal veterinarian. Two non-treated, separately housed animals functioned as normal controls. After anesthetization with ketamine, the cheek pouch was inverted and 200-400μL of contrast agent (at ca. 10^{12} particles per mL) was applied topically in 1x PBS containing 10% DMSO (v/v) for 15-20 minutes. Contrast agent exposure times were shorter than those used for biopsies due to the relatively short anesthetization times that are safely attained used ketamine. After washing, the hamsters were imaged using a portable reflectance confocal microscope [149]. Immediately following, biopsies were taken from the imaged area of the cheek pouch, and submitted for histological analysis. All animals were treated under the guidance from the institutionally-approved IACUC protocol study standards.

5.3.7 Ex-Vivo Lymph Node Biopsies

A patient seen at the M.D. Anderson Cancer Center Head and Neck Clinic who was scheduled for surgical resection of oral cavity carcinoma(s) and lymph node dissection was consensually recruited into an institutionally-sponsored patient protocol. The tumor, surrounding epithelial tissue, as well as the associated lymph nodes were removed by a head and neck surgeon. Care was taken during surgery to preserve the integrity of the tumor and associated lymphatic tissues, ensuring that the lymphatic drainage remained

unaffected. 1mL EGFR specific conjugates (using anti-EGFR mAb clone 225), at 10^{12} particles per mL in 10% DMSO in 1x PBS were injected into the primary tumor site and allowed to drain through the lymphatic ducts into the cervical lymph node basins. Then, a board-certified pathologist palpated each lymph node to determine the presence of metastatic growth. Both clinically normal and abnormal lymph nodes were taken for analysis, sectioned in the Krumdieck slicer, and imaged.

5.3.8 Optical Imaging

Homogeneous and heterogeneous tissue phantoms, as well as lymph node biopsies were imaged using a Leica TCS-4D confocal microscope using 488 nm excitation and 515/10 nm band pass filter and 514 nm excitation for the Fluorescein-labeled cells, as well as to collect autofluorescence of non-tagged samples. A 660 nm long pass filter was used to detect SNARF-labeled cells. Reflectance was acquired with 647 nm excitation. Balb/c nude mouse tumors were imaged using a Vivascope 2000 (Lucid, Inc.) portable laser scanning reflectance confocal microscope, with diode illumination at 830nm. Cervical biopsies were imaged using a Leica SP2 AOBS confocal microscope. Reflectance images were obtained with 594 nm and 633 nm illumination. Imaging of hamsters *in vivo* was carried out using a portable reflectance confocal microscope which is described in [149], and uses an 810nm diode illumination source.

5.4 RESULTS

5.4.1 Three-Dimensional Tissue Phantoms

In vivo molecular imaging requires development of efficient delivery systems of contrast agents to their targets. We used dimethyl sulfoxide (DMSO) to promote topical delivery of anti-EGFR gold conjugates. DMSO was chosen because of its permeation

efficiency, high aqueous solubility and because it is already FDA approved for human use [287] in certain applications.

We fabricated two types of 3D tissue constructs: (1) Homogeneous phantoms containing a high density of SiHa cervical cells and (2) heterogeneous constructs which consisted of a high-density mixture of EGFR(+) MDA-MB-468 and EGFR(-) MDA-MB-435 breast cancer cells in a 1:1 ratio. In the homogeneous case, phantoms were fabricated in transwell inserts (Corning), as described using SiHa cancer cells. Phantoms were labeled with anti-EGFR contrast agents in either a 10% DMSO in 1x PBS solution, or in 1x PBS only. They were subsequently removed and transversely sliced using a Krumdieck slicer. Figure 5.2A and B show transmitted and reflectance confocal images, respectively, of a transversely sectioned phantom labeled with the aid of DMSO. Note the presence of scattering signal (with a pixel count above the nose floor of 25) throughout the c. 400μm thickness of the slice. Figures 5.2C and D, however, show confocal transmittance and reflectance images, respectively, after an identical phantom is labeled *without* the use of DMSO as a delivery enhancing agent. Note that labeling is only apparent in a thin layer on one side of the phantom. An arrow indicates the surface from which contrast agents were applied. Figure 5E includes a higher magnification transmitted image of the homogeneous phantom, and indicates the high density appearance of cell growth attainable in this model.

In the heterogeneous case, EGFR(+) and EGFR(-) cell lines were labeled with membrane permeable derivatives of fluorescein and seminaphthorhodafluors (SNARF), respectively, which fluoresce only when they are inside the cells, as shown in low magnification in Figure 5.3A.

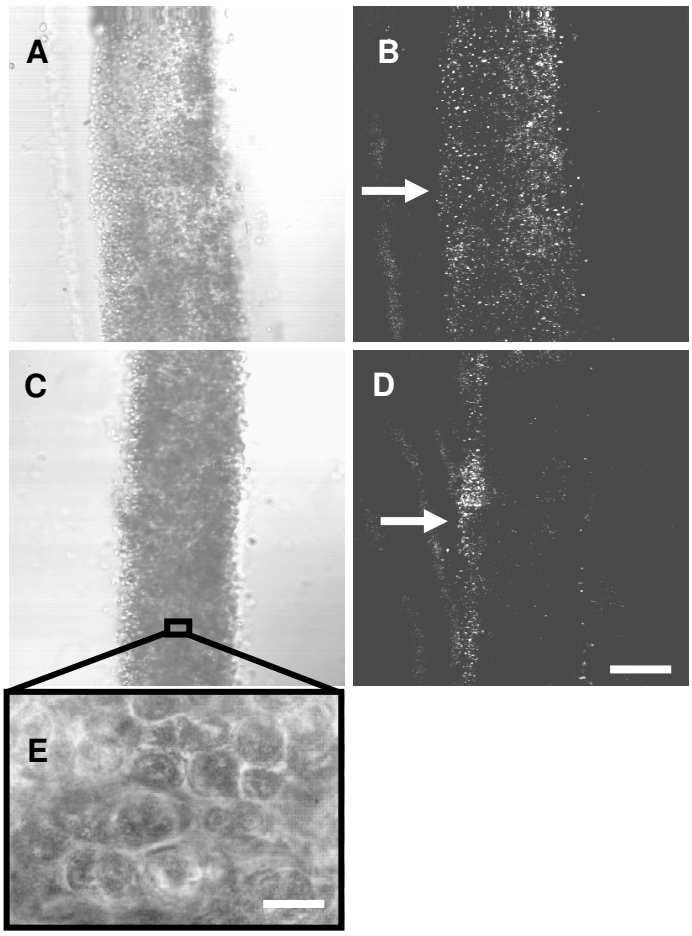

Figure 5.2 Transmittance (A, C, and E) and confocal reflectance (B and D) images of engineered tissue constructs labeled with anti-EGFR/gold conjugates. The contrast agents were added on top (indicated by arrows) of the tissue phantoms in 10% dimethyl sulfoxide (DMSO) solution in PBS (A and B) or in pure PBS (C and D). Phantoms were transversely sliced and imaged with a reflectance confocal microscope. Note the increased depth of penetration when using DMSO. Imaging at higher magnification (40X) shows the high density of the epithelial cells in the phantom (E). Reflectance images were obtained with 647 nm excitation. Arrows show the surfaces exposed to the contrast agents. The scale bars are ca. 200 μm (A-D) and ca. 20 μm (E).

Note the relatively random distribution of each cell type within the phantom. Some yellow signal is seen in the orange cells, and was deemed to be due to contributions from autofluorescence (and not dye cross-contamination). Figure 5.3B shows transverse sections of topically labeled heterogeneous tissue phantoms which indicate that the reflectance signal (white) is localized to the periphery of the green EGFR(+) cells. Little

to no reflectance signal is associated with red EGFR(-) cells, and in fact the average signal ratio between expressing and non-expressing cells was found to be c. 10. These results were repeated twice, and demonstrate that DMSO-mediated delivery does not adversely alter molecular specificity of the contrast agents and enables penetration through a thickness that corresponds to a typical epithelial layer.

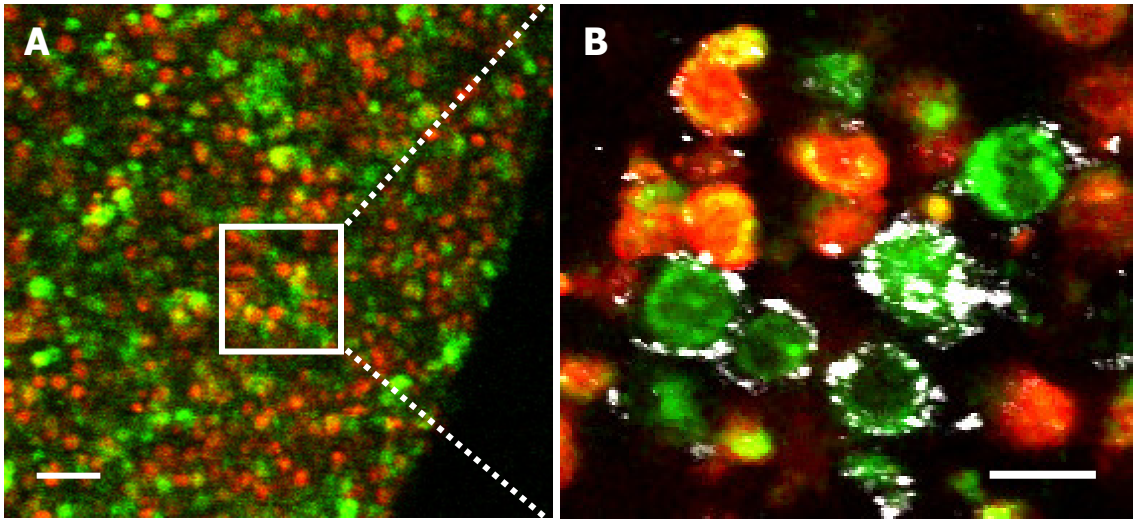

Figure 5.3 Heterogeneous three-dimensional tissue cultures. (A) Low magnification fluorescence confocal image of a transverse section, showing distribution of EGFR(+) cells in green and EGFR(-) cells in red. (B) High magnification image of the area indicated showing overlay of fluorescence image with corresponding reflectance image. Reflectance signal is shown in white. Scale bars are *ca*. 50 µm (A) and *ca*. 15 µm (B).

5.4.2 Balb/c Nude Mouse Model

While 3D tissue constructs represent an easily reproducible *in-vitro* biological model, the cell density of these phantoms is not quite as high as is achieved in an *in-vivo* system. The Balb/c nude mouse model represents another highly reproducible model of carcinogenesis whereby one or more tumors are created within the subcutaneous space within immuno-deficient, athymic mice [288]. In this model, multiple tumors are easily producible in one or more regions of the subcutaneous space, thereby providing for easy internal controls. After 1-6 weeks of tumor growth, the mice were sacrificed, tumors

resected, and placed in a solution of anti-EGFR gold conjugates in 10% DMSO in 1x PBS for up to 45 minutes at room temperature. The tumor was then sliced with a scalpel, exposing the inner necrotic core and imaged using the Vivascope portable confocal microscope. Figure 5.4 summarizes the results of this experiment. At left, (Figure 5.4A), a confocal reflectance image is shown of a labeled mouse tumor. At right (Figure 5.4B), a similar image is shown of an un-labeled tumor. Note that while there is significant signal present in both images, the labeled sample displays clear cell-membrane type morphology in the image. This is clearly consistent with labeling EGFR – a membrane-bound protein.

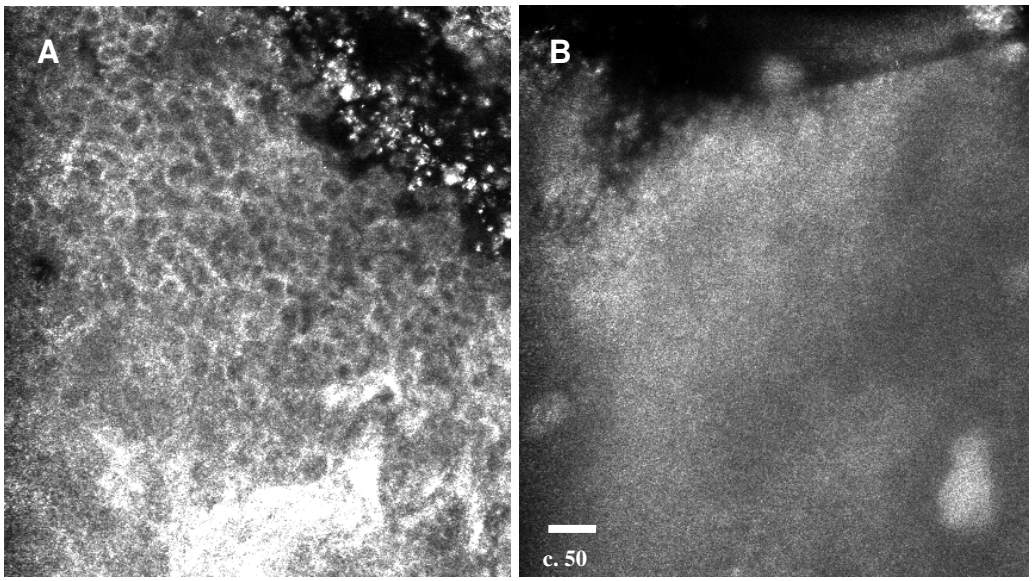

Figure 5.4. Confocal images (taken at 830nm) of subcutaneous tumors introduced into Balb/c nude mice. At left (A), the outline of the xenograft epithelial cells are clearly present, consistent with EGFR labeled cells. At right, (B), no such morphology is apparent, although a diffuse background is clearly present.

The presence of significant signal from the unlabeled sample, however, is troubling. We believe that the primary reason for this relatively poor contrast (in comparison with the heterogeneous phantoms) may be due to the very high levels of connective tissue

within the tumor, although this remains to be confirmed. After excision of the tumors, a hard layer of fibrous tissue was found to surround and permeate the tumors. This fibrous component is further supported by the fact that while vascularization of the tumor was evident surrounding the tumor, no blood vessels were found inside the core, producing a necrotic zone in the middle of the tumor. A second factor may be the illumination source in the Lucid Vivascope, which operates at 830nm – significantly removed from the optimal range for nanoparticles in the 600-650nm. From these limited observations, we conclude that, while potentially useful, the athymic mouse model may have some limitations in use for molecular imaging studies that render tumors whose morphology is significantly different than those seen in pre-cancerous and early cancerous lesions in stratified human epithelia.

5.4.3 Ex-Vivo Human Cervical Tissue

While 3D tissue cultures and ectopic animal tumors remain a useful, reproducible pre-clinical tool, the use of human *ex-vivo* epithelial tissue represents a more realistic model. We analyzed a total of four colposcopically normal/abnormal biopsy pairs. Table 5.1 summarizes the histopathologic diagnoses and the abnormal to normal reflectance intensity ratios of images of epithelial cells after labeling. The reflectance intensity was integrated over the entire epithelial thickness. The histopathologic diagnoses range from changes associated with human papillomavirus infection to CIN 3, and represents several important steps in the progression of pre-cancerous changes in the cervix. The reflectance intensity ratio increases with progression of carcinogenesis (Table 5.1); this correlates well with the increase of overall EGFR expression throughout the epithelial lining seen in pre-cancer progression in the cervix [102].

Table 5.1. The average signal intensity ratios between abnormal and normal biopsies from four different pairs. Note that the abnormal/normal signal ratio increase with pathological severity.

Histopathology of the abnormal sample	Reflectance intensity ratio of abnormal to normal samples after labeling with anti-EGFR gold nanoparticles
HPV associated changes	1.7
CIN 1	4.2
CIN 2	11.6
CIN 3	21

Figures 5.5A and B show representative confocal reflectance images of a biopsy with severe dysplasia (CIN 3), and a paired normal biopsy respectively, each labeled with anti-EGFR gold contrast agents. The abnormal specimen clearly shows a distinct "honeycomb" structure characteristic of EGFR labeling on cellular membranes. No distinct structures are visible in the normal biopsy. We observed signal intensity differences of up to 21 fold between normal and abnormal cases. Figures 5.5C and D show the corresponding H&E staining of the abnormal and normal biopsies, respectively, which corroborate the clinical diagnosis with a reading from a trained pathologist.

As further corroboration that the image morphology seen in figure 5.5 is indicative of EGFR expression, the relative signal strength as a function of depth below the epithelial surface was calculated for 10 different abnormal sites within each abnormal biopsy, and the average profile plotted in figure 5.6 (blue line). Alongside this data are plotted findings from the literature (green dots) [102], which show a similar overall increase. The data plotted in the blue line represents 10 measurements taken from different points in images of the case shown in figure 5.5 that was deemed by a pathologist to contain CIN III.

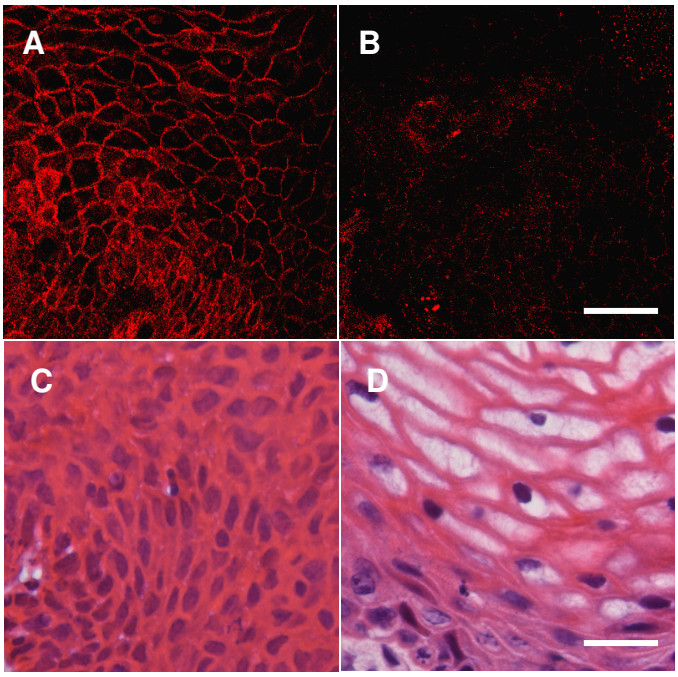

Figure 5.5. Confocal reflectance images of transverse sections of abnormal (A) and normal (B) cervical biopsies labeled with anti-EGFR gold conjugates. The image of the abnormal biopsy was obtained just above the basement membrane. Images of tissue intrinsic fluorescence were also collected (not shown) to independently confirm the presence of epithelial cells in the same field of view. Corresponding H&E staining of the abnormal (C) and normal (D) biopsies. Excitation wavelength of 647 nm was used in (A) and (B). Scale bars are *ca.* 25 μm.

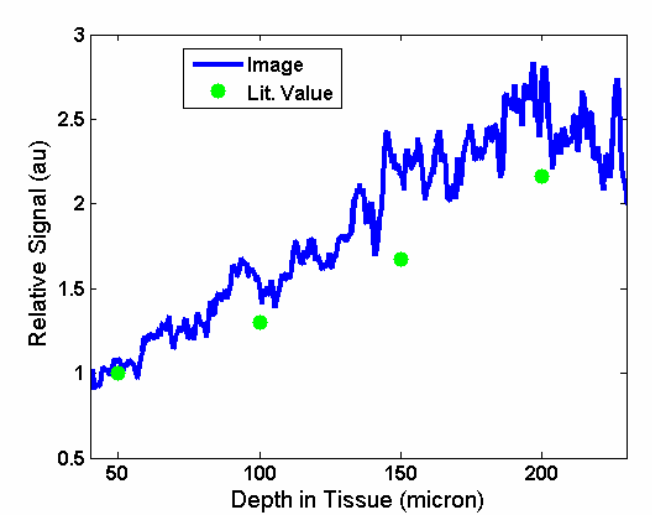

Figure 5.6. Relative signal strength measured in abnormal biopsies (averaged over 10 sites) as a function of depth below the surface (blue line). Note the overall increase in signal as a function of tissue thickness, consistent with values found in the literature.

Further, treatment of biopsies with non-specific contrast agents resulted in no apparent signal. A remaining question, however, concerns the effect on nanoparticle delivery of the naturally occurring permeability increases due to the decrease in cell to cell junctions seen in dysplastic tissue [289]. To begin to address this, an abnormal/normal cervical biopsy pair was labeled fluorescently-tagged gold nanoparticle conjugates. Subsequent fluorescence imaging revealed that while delivery through the abnormal biopsy extended past 300μm, penetration of only 100-150μm was seen with in the normal biopsy. Further spectroscopic analysis (using a ball lens probe, described in [148], data not shown) revealed that 40% less conjugate was delivered overall to the normal sample. This result seems to suggest that the carcinogenesis actually promotes the delivery of gold nanoparticle conjugates, though the extent of this result is better evaluated through a more careful study.

5.4.4 Hamster Cheek Pouch Model

We also demonstrated the efficacy of molecular specific imaging with gold bioconjugates *in vivo* in the hamster cheek pouch carcinogenesis model. Histologically, the 16-week treatment with dimethyl benz[α]anthracene (DMBA) pushes the epithelial lining of the cheek pouch through progressive dysplastic changes and ultimately carcinoma *in-situ* [286]. Anesthetized hamsters were imaged with a portable reflectance confocal microscope described in [149] right before and after topical application of anti-EGFR gold nanoparticles. Figure 5.7 shows results of *in vivo* imaging of the cheek pouch of the same hamster at different points of the study. Images in Figure 5.7A were obtained before the beginning of treatment with DMBA and images in Figure 5.7B shows the results after 3 weeks of treatment with the carcinogen. Images on the left indicate before

application of contrast agents, while those on the right are taken after 30 minutes of application. Although the contrast agents were applied in both imaging sessions (before and after initiation of carcinogenesis), cell-membrane morphology characteristic for labeling of EGF receptors and a significant increase in scattering intensity after the application of gold bioconjugates were observed only after the animal was treated with DMBA (Figure 5.7B right). The contrast in the images between the normal animal (Figure 5.7A right) and the animal with early neoplastic changes (Figure 5.7B right) after the application of the contrast agents exceeds 10 times. Figures 5.7A and B at left indicate appearance before application of contrast agents. Figure 5.7C shows that imaging results were confirmed using EGFR immuno-histochemical staining of cheek pouch biopsies taken from the areas which were imaged *in vivo*. Figure 5.7C, left shows normal tissue, and abnormal tissue is shown in 5.7C, right. These results suggest the possibility of molecular specific imaging with topically delivered gold bioconjugates. However, they were not always repeatable. We attribute the difficulty in topical delivery of the nanoparticles to extremely high levels of superficial keratin expressed in the hamster buccal mucosa.

The thick layer of keratin represents a significant barrier against topical delivery of not only nanoparticles and macromolecules but even small molecules like acetic acid. Fortunately, such elevated levels of surface keratin are not characteristic for human epithelial tissues, save for extremely advanced cases of keratosis. Therefore, future pre-clinical evaluation of topical delivery of contrast agents should be focused on animal models with levels of keratin expression that are more representative of human epithelium.

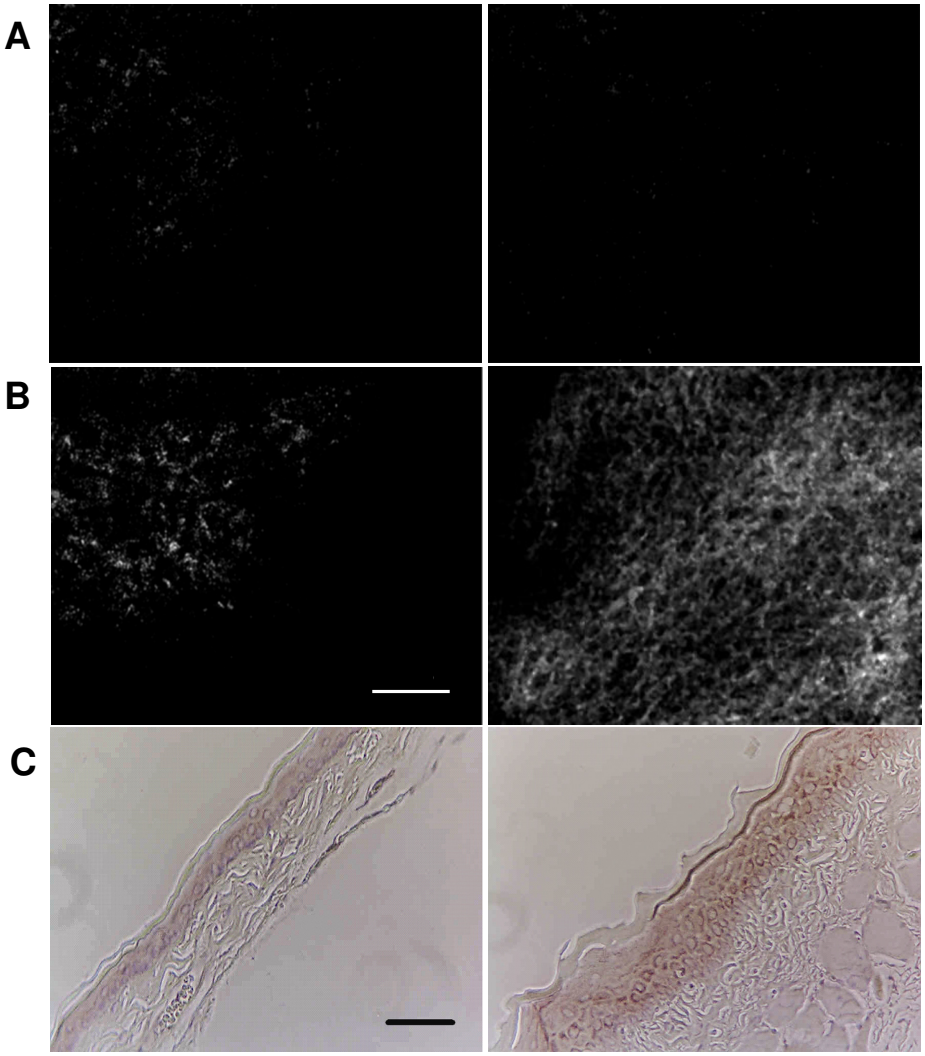

Figure 5.7. ***In vivo*** **confocal reflectance imaging of EGFR overexpression in a hamster model. Images shown are obtained from the same hamster before the beginning of the treatment with carcinogen – DMBA (A) and after 3 weeks of DMBA treatment (B). The images were taken immediately before (A, left and B, left) and after (A, right and B, right) topical application of the anti-EGFR gold conjugates. EGFR immuno-histochemical staining (C) reveals elevated EGFR levels in the DMBA-treated animal (C, right) and very low levels of EGFR expression before DMBA treatment (C, left). The scale bars are** ***ca.*** **50 μm.**

5.4.5 Resected Human Head and Neck Lymph Nodes

While the previous results have shown that optical interrogation of immuno-conjugated gold nanoparticles can be used to detect pre-cancerous epithelial lesions, there

certainly remains other vital clinical needs for this type of molecular imaging. It is particularly important to be able to stage more advanced cases in terms of the degree of metastatic spread that often occurs through the lymphatic system. There is a plethora of current work focused on developing better lymph node metastasis detection in the breast [290], lung [291], and oral cavity [292], among others. The use of optical techniques for "sentinel lymph node" detection – that is, detection of small metastases in the primary draining lymph node for a particular tumor – has become quite popular [61, 293-296], particularly via the use of fluorescent tracers. To better understand the anatomy in question, refer to figure 5.8 from [297] which shows the relatively complex anatomy of the head and neck lymphatic system. As such, this organ site in particular would benefit from a method that could accurately detect metastatic spread to a particular node among the many surrounding the oral cavity.

To determine the feasibility of using immuno-targeted nanoparticles for micro-metastasis detection, a patient undergoing radical dissection of an advanced oral cavity tumor and associated lymph nodes at the U.T. M.D. Anderson Cancer Center Head and Neck Clinic was enrolled in a patient protocol. The terms of the protocol were such that during the surgical procedure, the tumor was resected, along with the associated lymphatics attached. The sample was brought to a dedicated pathology suite where the primary tumor was injected with a solution of EGFR-targeted (clone 225, Neomarkers) gold nanoparticles suspended in a solution of 1x PBS plus 10% DMSO. Clone 225 is often used for *in-vivo* applications, due to its being humanized [298]. A total of 2-3mL was injected into several positions on the tumor. After 45-60 minutes, a board-certified pathologist palpated the individual lymph nodes within the sample to determine the

presence of metastases. The clinically abnormal lymph nodes, along with clinically normal nodes were taken for imaging using the Leica TCS-4D confocal microscope.

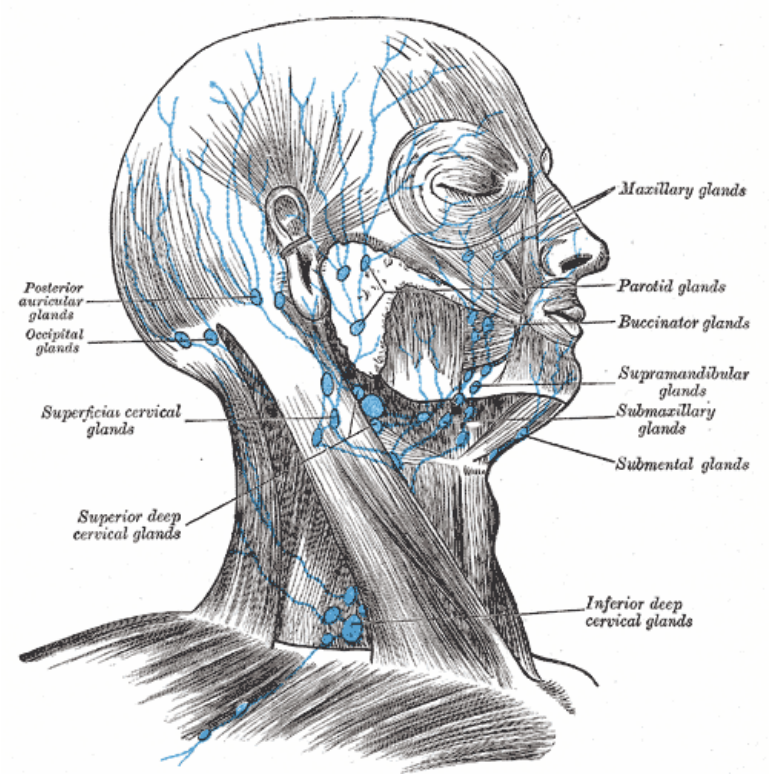

Figure 5.8. Anatomy of human cervical lymph nodes. Note that depending on where in the oral cavity a tumor arises, the primary draining lymph node (i.e. the "sentinel" lymph node) will be different.

Figure 5.9 shows the results from imaging a clinically normal and abnormal lymph node from the above mentioned patient. In (A), the confocal reflectance at 647nm is shown for the abnormal, while in (B) it is shown for the normal. Immediately obvious is the overall increase in scattering seen in the abnormal image. However, to more convincingly postulate that this is due to the presence of EGFR expressing cells within the lymph node, a confocal image was also taken of the same fields of view in fluorescence mode, under 488nm excitation and 500nm long-pass emission. This excitation/emission pair is well suited to imaging the autofluorescence in cells due to

NADH [164], and is a good way to determine the morphological state and relative position of cells in a field of view. These images are shown in figure 5.9(C) and (D) for the abnormal and normal, respectively. Note that cells are discernable above the background level in the abnormal case, but not in the abnormal case. Finally, in (E) and (F), the reflectance and fluorescence images are overlaid to give a more complete picture of the sample. Figure 5.9(E) shows the characteristic cell periphery morphology under reflectance imaging, with a bright cytoplasmic autofluorescence overlaid. This morphology is highly consistent with the presence of EGFR over-expressing cells within the lymph node matrix. No such morphology is seen in (F). Both of these results were confirmed with conventional H&E staining of the same samples, which tested positive for metastasis in the abnormal node, and an absence in the normal node. While these results are encouraging, they are also preliminary, and certainly a more thorough study will be necessary to more fully explore the use of immuno-targeted gold nanoparticles for this application.

5.5 DISCUSSION

We believe that the data summarized in this chapter serves as a beginning point in order to posit the potential advantages and challenges of implementation of gold nanoparticles in the clinic. From a toxicological point of view, it is attractive that the bioreactivity and toxicity of metallic gold has long been established as low, as evidenced by the use of metallic gold implants, the exploration of gold nanoparticles as gene therapy carriers for HIV patients with up to 500 mg of gold applied during treatment [66]; and pre-clinical studies of a new minimally invasive thermal treatment of cancer using gold nanoshells [242].

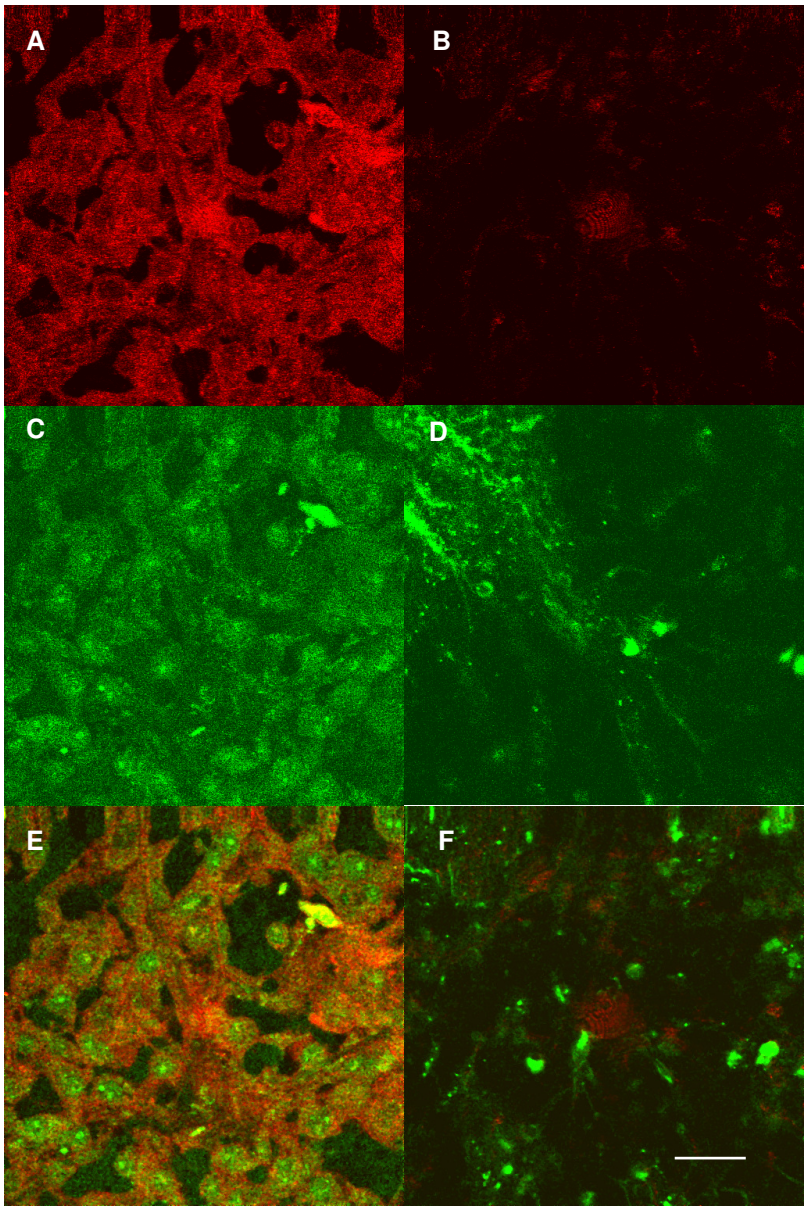

Figure 5.9. Imaging of clinically abnormal (left column) and clinically normal (right column) lymph nodes in resected human tissue after injection of anti-EGFR contrast agents into the primary tumor. First row (A & B): confocal reflectance. Second row (C & D): auto-fluorescence. Third row (E & F): reflectance and fluorescence overlaid. Scale bar is ~20μm [data unpublished].

However, it is important to note that metallic gold is not metabolized. In some cases a premalignant lesion can require a long patient follow up, therefore potential interference between the initial labeling with gold nanoparticles and subsequent imaging should be

considered. It is well known that EGFR is regularly internalized and degraded within the cell [299]. The degraded receptors are replaced with newly synthesized EGFR that can be targeted by the contrast agents. The fate of the gold nanoparticles internalized is unclear, although uptake by macrophages has been observed *in-vitro* with no cytotoxic effects [65].

Delivery of nanoparticulates through mucosal boundaries has been demonstrated in a number of studies for a variety of size ranges. For example, 150-300 nm diameter chitosan derivative-based nanoparticles have been successfully used as therapeutic carriers for peanut allergy immunization in the intestinal epithelium [300]. DMSO has been shown to facilitate trans-mucosal transport of several materials such as antibodies [301], anti-cancer drugs [302], and photosensitizers [303]. The FDA has approved DMSO as a treatment for interstitial cystitis via bladder instillation [287], and the toxicity of DMSO has been shown to be quite low, with an LD_{50} of 17,400 mg/kg. Further, there are several other compounds that have been shown to promote transmucosal permeability such as polyvinyl pyrrolidone (PVP) [304], chitosan [300], and lipid surfactants [305] that may be utilized for promoting topical delivery of gold nanoparticle contrast agents.

From an imaging point of view, it is clear that gold nanoparticles can produce high quality, molecular specific images under many circumstances. The abnormal to normal signal intensity ratio was shown far higher than the actual level of EGFR over-expression in both the cervical biopsy and the *in-vivo* hamster cheek pouch. There are, however, challenges as well, including the presence of high endogenous scattering sources, such as keratin, which also act as a transport barrier to both photons and nanoparticles. As was mentioned, the delivery of nanoparticles was found to be significantly reduced in a

normal cervical biopsy. While this may be viewed advantageously, it would certainly be worthwhile to study further the effect of carcinogenesis-enabled tissue permeability, and tight junction reduction as a facilitator of contrast agent delivery. The preceding data will, hopefully, act as a guide for a number of future studies.

5.6 ACKNOWLEDGEMENTS

The author would like to thank Ms. Vivian Mack for help in fabricating heterogeneous tissue phantoms, as well as the sub-cutaneous mouse tumor model. Also, thanks go to Drs. Michele Follen and Andrea Milbourne for cervical biopsies, as well as Dr. Ann Gillenwater for oral cavity lymph node resections. In addition, the author would like to thank Dr. Lezlee Coghlan for expertise in the hamster cheek pouch model. The author would also like to acknowledge Tom Collier for hamster imaging. Thanks also go to Dr. Anais Malpica, for pathological reading of cervical biopsies; as well as Ms. Nancy Abbey and Ms. Jimi Lynn Brandon, for histological staining. Finally, funding from NSF IGERT program as well as NCI Grant R01-CA103830 BRP is gratefully acknowledged.

CHAPTER 6

Magnetic Gold Multimodal Nanoparticles for EGFR Imaging*

6.1 ABSTRACT

It has been shown that molecular specific labeling of EGFR is possible in a range of increasingly complex biological models, often with quite high contrast. However, a multifaceted approach is clearly needed in many instances to increase the signal strength and specificity in cases where optimal delivery of contrast agents is difficult, or if there is a high concentration of endogenous scatterers. This chapter details a novel approach for optical imaging that combines the advantages of molecularly targeted plasmonic nanoparticles and harmonic magnetic actuation. This combination is achieved through hybrid nanoparticles with an iron oxide core surrounded by a gold layer. The nanoparticles are targeted *in-vitro* to epidermal growth factor receptor, a common cancer biomarker. The gold portion resonantly scatters visible light giving a strong optical signal and the superparamagnetic core provides a means to externally modulate the optical signal. The combination of bright plasmon resonance scattering and magnetic actuation produces a dramatic increase in contrast in optical imaging of cells labeled with hybrid gold/iron oxide nanoparticles.

6.2 INTRODUCTION

Exogenous contrast agents are widely used to increase signal intensity and specificity during optical interrogation of biological materials. Organic fluorescent dyes are traditional contrast enhancing molecules for in vitro and in vivo optical imaging [167-

* The contents of this chapter have been published in *Opt. Exp.* **14**(26) 12930-12943

170]. Recent advances in nanotechnology have led to the development of novel bright contrast agents, including quantum dots [23, 60, 180-182] and plasmonic nanoparticles [30, 70, 81, 195, 244, 245]. Progress in nanomaterial chemistry has allowed synthesis of semiconductor quantum dots with increased fluorescence efficiencies [306], tunable emission bands [56], and relatively slow photobleaching rates [23]. On the other hand, it was demonstrated that plasmonic metal nanoparticles offer additional advantages over luminescent quantum dots including significantly larger optical cross sections, complete resistance to photobleaching, and non-toxic constituent materials [30, 70, 81, 195, 244, 245, 265].

Strategies using antibody or aptamer targeting molecules provide molecular specificity to optical imaging [307, 308]. However, most biological systems are very complex both in composition and morphology. Thus, endogenous scatterers and fluorophors can account for a significant portion of the total signal intensity causing problems in molecular specific optical imaging, especially in vivo [180]. Molecular specific contrast agents would be better utilized if novel optical methods were employed that concurrently reduce or prevent unwanted background signal. It was demonstrated that contribution of the endogenous background signal can be reduced using the effect of plasmon resonance coupling between gold nanoparticles [195, 245]. The dipole-dipole coupling between closely spaced gold particles produces a red wavelength shift in their scattering and extinction cross sections [191, 309]. This property was exploited for development of ultrasensitive DNA assays in vitro [71, 310, 311]. Recently, we used 12 nm gold nanoparticles conjugated to monoclonal antibodies specific for epidermal growth factor receptor (EGFR) to label living cancer cells [195]. Although isolated nanoparticles

have a maximum scattering cross section in the green optical region, labeled cells exhibit a very strong scattering signal in the red. This red-shift behavior was attributed to the dipole-dipole coupling of gold bioconjugates bound to EGFR molecules on the cell surface [195]. The effect of plasmon resonance coupling affords an opportunity to spectrally reject the background associated with endogenous cellular scattering which is predominant in the blue spectral region.

Another effective strategy to reduce unwanted background signal has been demonstrated by Oldenburg, et al. [312] in optical coherence tomography (OCT) imaging of macrophages loaded with magnetic particles. The approach is based on inducing a magnetically actuated movement in cells containing magnetic iron oxide microparticles. Subsequent implementation of a simple frame subtraction algorithm reduces the background signal associated with the surrounding non-magnetic media. A similar approach was used by Anker et al. [313]. Polystyrene microbeads loaded with a dye and a ferromagnetic material were sputter-coated with aluminum or gold leaving a small uncoated area on the surface of the beads. Then, the microbeads were used for optical imaging and exhibited a bright fluorescence signal only when they were magnetically oriented with a metal coated side facing away from a detector. The metal coating blocked the fluorescent emission when the metal-coated side was oriented towards the detector, and image subtraction removed non-specific signals. In another study, superparamagnetic iron oxide nanoparticles (SPIO) have been magnetically actuated in mouse liver tissue and detected using ultrasound imaging [314].

Recently, a new type of nanomaterial - magnetic/gold composite nanoparticles have been synthesized by several different routes [64, 237, 315]. Lin et al. [315] utilized an

inverse micelle technique to form crystalline iron cores within micelles and subsequently adding chlorauric acid and sodium borohydride to obtain gold-coated iron. The inverse micelle technique creates particles with a narrow size distribution, but further steps must be taken to transfer them to aqueous solution for subsequent functionalization. The magnetic properties of these particles were further characterized in [316]. It is important to note that the gold coating does not prevent the iron core from oxidizing over a period of several weeks [317]. Stoeva et al. [318] synthesized ~200 nm diameter three-layer nanoparticles with a Fe2O3 layer between a SiO2 core and an outer gold shell in a two phase process. Once in aqueous phase, these particles were functionalized with oligonucleotides and shown to reversibly bind via DNA hybridization. Wang et al. [319] followed a similar synthesis route to produce iron oxide/gold core/shell nanorods with a final length of 250 nm. The synthesis developed by Lyon et al. [64] is entirely aqueous and was adapted from an iterative hydroxylamine seeding technique originally suggested in [320]. Jeong et al. [321] used the hydroxyl amine seeding protocol to produce a magnetic colloid suspension and then attached a functional enzyme to the nanoparticles to magnetically decant and recover the enzyme for reuse. Wang et al. [36] used an inverse micelle technique to synthesize magnetic gold particles that could be loaded into rat embryonic neural cells for *in-vivo* MRI imaging.

Here, we describe a new approach for molecular specific optical imaging *in-vitro* that combines the advantages of molecularly targeted plasmonic nanoparticles and magnetic actuation. This combination is achieved through hybrid nanoparticles with a superparamagnetic core surrounded by a gold layer. The nanoparticles were conjugated with monoclonal antibodies for molecular recognition. The hybrid nature of these

particles provides new opportunities for optical contrast enhancement. The addition of the gold layer leads to three important advantages: (1) strong optical signal that facilitates detection and digital processing; (2) tunable optical resonances; and (3) a convenient surface for conjugation of probe molecules [68, 322]. The iron oxide core provides a magnetically susceptible component which can be exploited to periodically actuate the magnetic particles attached to cells in the field of view and, therefore, allows use of an external magnetic field for modulation of the optical signal. We demonstrate that opto-magnetic hybrid nanoparticles can be used to increase optical contrast in cancer cell imaging. This report is focused on EGFR – one of the hallmarks of carcinogenesis. EGFR has been found to be over-expressed in many types of cancers including lung, breast, bladder, cervix, and oral cavity [7].

6.3 METHODS

6.3.1 Iron Oxide/Gold Hybrid Nanoparticles

Magnetically susceptible plasmonic nanoparticles were synthesized using the method described in [64]. Briefly, 9 nm magnetite (Fe_3O_4) particles were formed via co-reduction of $FeCl_2$ and $FeCl_3$ in an aqueous NaOH solution. The Fe_3O_4 cores were oxidized to primarily Fe_2O_3 by boiling in a 0.01M HNO_3 solution. X-ray diffraction measurements (not shown) of the prepared magnetic cores were characteristic for maghemite, or γ-Fe_2O_3. Subsequently, a *ca.* 20nm thick gold shell was deposited using the hydroxylamine seeding method [320]. This procedure involves sequential additions of $HAuCl_3$ in the presence of citrate and hydroxylamine. It was shown that hydroxylamine confines the reduction of Au^{3+} ions to the pre-existing surface of iron oxide particles, thereby largely preventing the nucleation of pure gold particles in

solution. The iron seeds and hybrid iron oxide/gold nanoparticles were characterized using a Philips EM 208 Transmission Electron Microscope (TEM) equipped with an AMT Advantage HR 1MB digital camera detector.

6.3.2 Antibody Conjugation

The hybrid nanoparticles were conjugated to anti-EGFR monoclonal antibodies (clone 29.1.1, Sigma) for molecular specific imaging. Antibodies were attached to gold nanoparticles via a conjugation linker that consists of a short polyethylene glycol (PEG) chain terminated at one end by a hydrazide moiety, and at the other end by two thiol groups. First, antibodies at a concentration of 1mg/mL were exposed to 10mM $NaIO_4$ in a 40mM HEPES pH 7.4 solution for 30-40 minutes at room temperature, thereby oxidizing the hydroxyl moieties on the antibodies' Fc region to aldehyde groups. The formation of the aldehyde groups was colorimetrically confirmed using a standard assay with an alkaline Purpald solution (Sigma). Then, excess hydrazide-PEG-thiol linker was added to the oxidized antibodies and allowed to react for 20 minutes. The hydrazide portion of the PEG linker interacts with aldehyde groups on the antibodies to form a stable linkage. In this procedure a potential loss of antibody function is avoided because the linker can not interact with the antibody's target-binding region, which contains no glycosylation. The unreacted linker was removed by filtration through a 100,000 MWCO filter (Millipore). After purification, the modified antibodies were mixed with gold nanoparticles in 40mM HEPES (pH 7.4) for 20 minutes at room temperature. During this step a stable bond is formed between the gold surface and the linker's thiol groups. Afterward, monofunctional PEG-thiol molecules were added to passivate the remaining

nanoparticle surface. Finally, the conjugates were centrifuged at 2800 rcf for 45 minutes and resuspended in 1x PBS.

6.3.3 Cell Culture Model

EGFR over-expressing A-431 cells [83] were used to demonstrate molecular specific imaging with hybrid iron oxide/gold nanoparticles. Cells were cultured in DMEM plus 10% FBS at 37°C in a 5% CO_2 environment. For labeling experiments, the cells were suspended in phenol-free DMEM, mixed with the nanoparticle-antibody conjugates, and allowed to react for 20-30 minutes under mild agitation at room temperature. Typically, 200-300μL of a cell suspension (~10^5 cells/mL) was mixed with an equal volume of nanoparticles suspended at approximately 10^{10} particles/mL. The labeled cells were washed in phenol-free DMEM and resuspended in an isotonic 1% gelatin solution. The gelatin provides a viscous environment that is more similar to *in vivo* conditions than pure tissue culture media and also prevents cells from electrostatically adhering to the glass coverslip during imaging. In addition to cells labeled with hybrid nanoparticles we included two internal negative controls: unlabeled A-431 cells and cells labeled with 40nm pure gold nanoparticles. Because of relatively small optical property differences between 40 nm pure gold and 50 nm magnetic gold nanoparticles (only *ca.* 10 nm separation in extinction spectra maxima) we conjugated pure gold particles with fluorescently labeled anti-EGFR monoclonal antibodies. Therefore, pure-gold particles exhibited a strong fluorescence signal, while the gold/iron oxide particles did not, allowing easy discrimination between the two populations of labeled cells. We used AlexaFluor 488 as the fluorescent tag and a standard labeling kit available from Molecular Probes to fluorescently label antibodies. The controls were prepared in the

same manner as cells labeled with hybrid nanoparticles and all three cell types were mixed together in 1:1:1 ratio. An aliquot of this mixture was placed on a microscope slide for optical measurements.

6.3.4 Imaging system

Samples were imaged using a Leica DM 6000 upright microscope in epi-illuminated darkfield mode. A 75W Xenon light source was used for illumination. Images were collected through a 20x darkfield/brightfield objective with a 0.5 collection NA, and detected using a Q-Imaging Retiga EXi ultra-sensitive 12-bit CCD camera. Time-course images of magnetically actuated cells were taken in monochrome mode at approximately 10 frames per second. Hyperspectral imaging was used to measure the spectral differences between labeled and unlabeled cells. The hyperspectral imaging system (PARISS, LightForm, Inc.) incorporates a slit and a prism dispersion configuration. In this scheme, the sample is laterally scanned using a piezoelectric stage, with the slit allowing a ~1μm wide portion of the image through the imaging system. Each line of the image is spectrally dispersed via the prism and projected onto a two dimensional CCD detector. The device allows for a spectral range of approximately 350-850nm, and 1 nm spectral resolution. A microscopically clean aluminum mirror was used to collect the spectral profile of the light source, which was used to normalize the spectra recorded from cells. Fluorescence imaging was performed in epi-mode using a 490nm excitation/510nm emission fluorescence filter cube (Chroma).

6.3.5 Statistical Image Analysis

For each type of cell (magnetically labeled, pure gold labeled, and unlabeled), as well as for each illumination condition (white light and 635nm band-pass illumination) and for

magnetically actuated and un-actuated, 10 cells or more were analyzed. To calculate average signal intensities each cell was manually segmented from the image, the signal background subtracted, and the average non-zero pixel intensity values were calculated. Then an average signal and standard deviation were determined for each cell type and illumination condition. A one-tailed, paired t-test (assuming unequal variances) was performed among the three cell populations. Then, the resulting T statistic then was used to calculate a p-value. Calculations were repeated in both Matlab and Excel for confirmation.

6.3.6 Magnetic actuation

Figure 6.1 outlines the experimental setup. A solenoid electromagnet (Ledex 6EC) with a cone shaped ferrite core was used to magnetically actuate the samples.

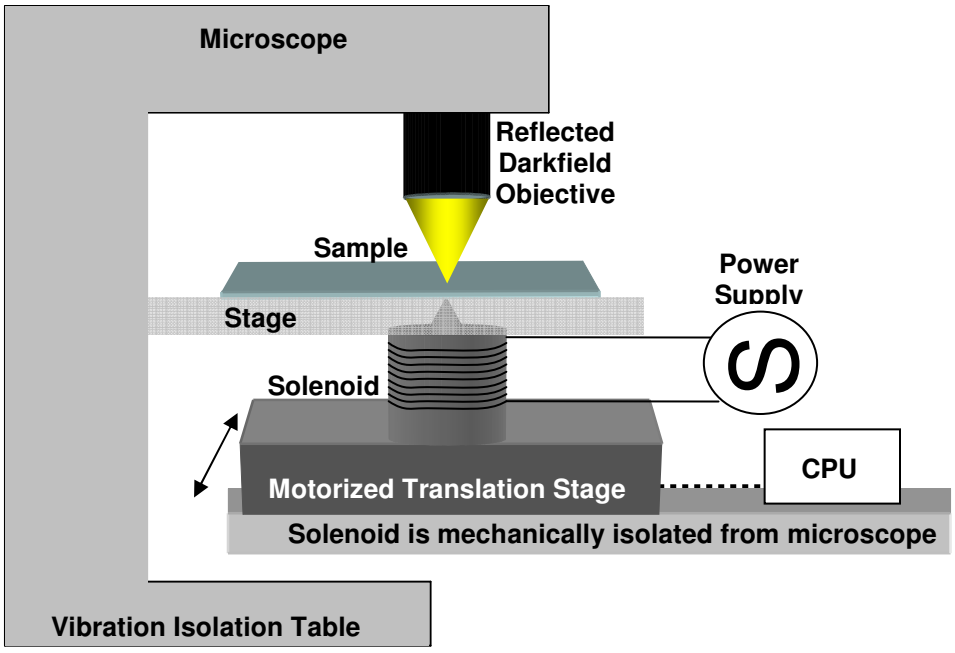

Figure 6.1 Experimental setup. Cells were mounted on a microscope slide and imaged in reflected darkfield mode using a Leica DM 6000 upright microscope. A solenoid electromagnet with a cone-shaped ferrite core was attached to a programmable piezoelectric translation stage, and placed beneath the sample stage. Translation stage motion oscillated in a sinusoidal fashion with a user-definable amplitude and frequency. The magnet was powered by a power supply and amplifier delivering up to 960 W. The solenoid and motorized translation stage assembly was mechanically isolated from the microscope, which sat on a vibration isolation table.

The electromagnet was driven by a power supply and current amplifier, which delivered up to 960W to the coil. The field strength at the tip of the magnet was 0.7 T and the field gradient in z-direction from the tip of the core extending 1 mm outward was 220 T/m. The electromagnet was attached to a motorized translation stage (Aerotech) and driven by a programmable controller that permitted sinusoidal movement with a user determined frequency and amplitude. The motion amplitude was adjusted to approximately one full field of view. Care was taken to ensure that the moving stage was mechanically-isolated from the microscope and its vibration isolation table. Any sample movements due to vibrations caused by the moving stage were minimized.

6.4 RESULTS

6.4.1 Characterization of Gold/Iron Oxide Multimodal Nanoparticles

Figures 6.2A shows transmission electron micrographs of the Fe2O3 core nanoparticles before the addition of gold and figure 6.2B reveals the morphology after deposition of the gold layer. The addition of gold results in an approximately 5-fold increase in particle diameter. Analysis of TEM images reveals that the average diameter of the iron oxide/gold nanoparticles was 50 nm with a standard deviation of 14 nm. The cause for the relatively large size distribution of the resulting nanoparticles is not very well understood and it presents a technical challenge that remains to be fully addressed. Possible aggregation of the iron oxide core particles before gold deposition might be part of the problem. The process of gold deposition was also monitored using an UV-Vis spectrophotometer (BioTek Synergy HT), as shown in figure 6.2C. Before the addition of the gold shell, the extinction properties of the superparamagnetic particles are consistent with sub-wavelength sized dielectric spheres. However, upon addition of the

gold layer onto the iron oxide core, the extinction spectrum changes markedly, displaying a plasmon resonance peak at 540nm. We also ran theoretical simulations to model the scattering and absorption properties of the gold/iron oxide nanoparticles (figure 6.2D). Core-shell composite particle simulations were implemented using custom Matlab/C++ codes based on the equations from [323]. Dielectric functions used are based on the experimental data from [324], with corrections for the effect of particle size as detailed in [325]. Results from these codes have been extensively compared to composite particle simulations in the literature. In order to simulate the effects of a statistical distribution of particle sizes, the output from the cross section codes was further integrated using a Gauss-Lobatto adaptive quadrature algorithm. The simulated extinction spectrum is in excellent agreement with our measurements (Fig 6.2C). The simulations showed that the peak absorption, extinction, and scattering wavelengths are 534nm, 537nm, and 550nm, respectively. The total scattering from the hybrid nanoparticles represents about 20% of the total integrated extinction.

6.4.2 Darkfield Imaging of Labeled Cells

Figure 6.3A shows a color dark-field reflectance image of the A-431 cell mixture which consists of unlabeled cells (indicated by blue arrows), cells labeled with 50nm gold/iron oxide nanoparticles (red arrows) and with 40nm pure gold nanoparticles (green arrows). Magnetic gold and pure gold labeled cells were differentiated from one another using a fluorescent tag (AlexaFluor 488, Molecular Probes) that was attached to the monoclonal antibodies conjugated with 40nm pure gold nanoparticles but was absent on the hybrid nanoparticles (see section 6.3.3).

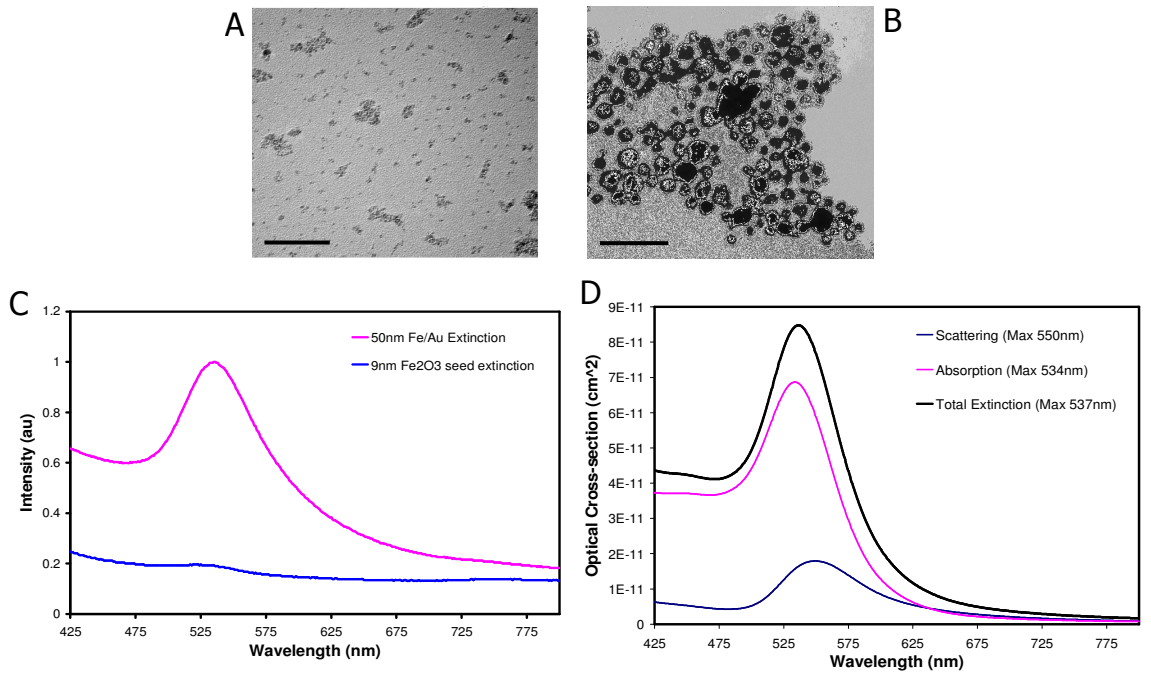

Figure 6.2 TEM images of 9nm Fe_2O_3 nanoparticles before (A) and after (B) deposition of the metallic gold layer. Images were collected at 80keV acceleration and 180,000x direct magnification. Scale bars are 200nm. In (C), UV-Vis extinction spectra are shown of a suspension of 9nm Fe_2O_3 nanoparticles (blue) and the same suspension after deposition of *ca.* 20nm gold layer (pink). Bare Fe_2O_3 particles show typical inverse-power law type extinction properties. The addition of gold to the surface results in the appearance of a characteristic plasmon resonance peak at *ca.* 540nm. In (D), theoretical simulations show the relative contribution of absorption (pink) and scattering (blue) to the total extinction (black) of the nanoparticles. The calculated maximum wavelengths for absorption, extinction, and scattering are 534nm, 537nm, and 550nm, respectively and include the effect of particle size distribution as determined by TEM.

The unlabeled cells appear blue due to the characteristic intrinsic cellular scattering. The labeled cells exhibit dim green regions and bright easily identifiable regions with different shades of orange. The green tinge is the color of the isolated nanoparticles and corresponds to regions with low density of the contrast agents. The orange color corresponds to the closely spaced assemblies of anti-EGFR gold conjugates which interact with EGFR receptors on the cytoplasmic membrane of A-431 cells. The intensity difference between the labeled and unlabeled cells which is achieved under white light illumination can be additionally improved if a 635±15nm band-pass filter is placed into

the illumination path (figure 6.3B). This is possible because the endogenous scattering of cells (Fig. 6.3C, blue line) is significantly reduced in the red optical region [326]. In addition, cells labeled with 50 nm hybrid particles display a prominent scattering peak in the red region at approximately 690 nm (Fig. 6.3C, red line). Similar behavior is observed with cells labeled with 40nm pure gold nanoparticles (Fig. 6.3C, green line).

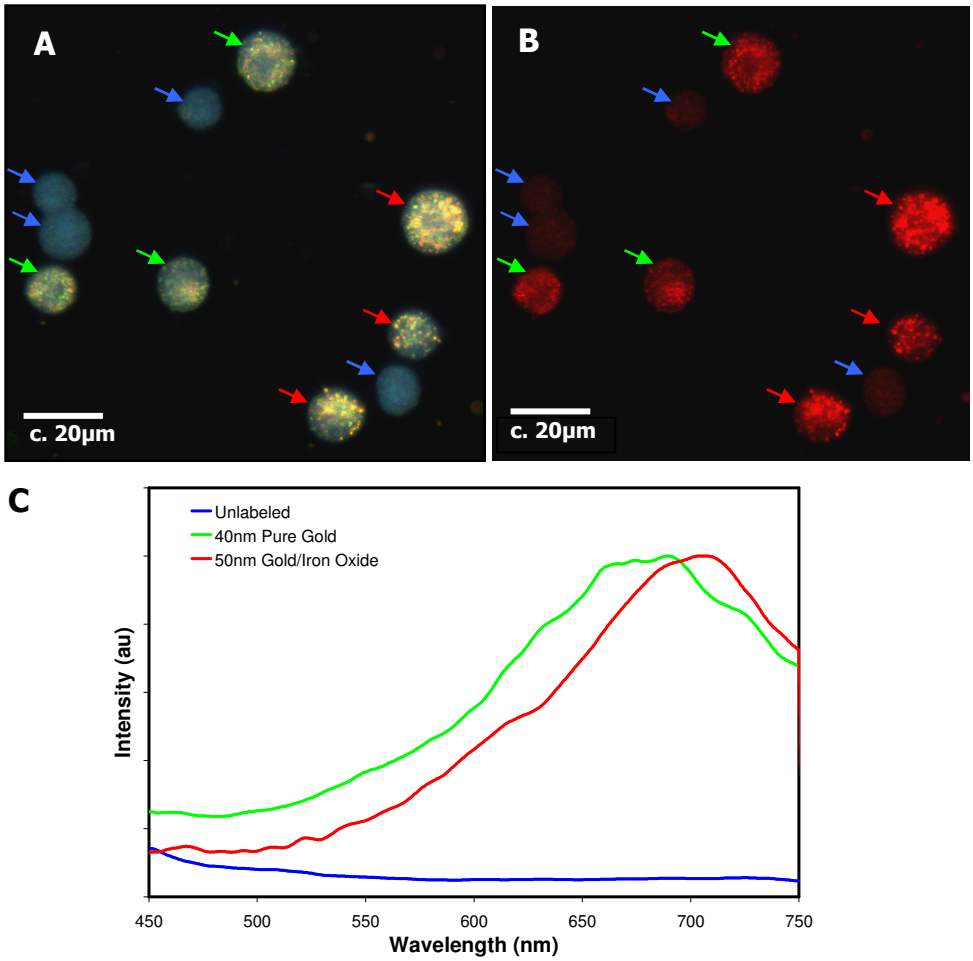

Figure 6.3 Darkfield images of a 1:1:1 mixture of A-431 cells labeled with 40nm anti-EGFR gold nanoparticles (indicated by green arrows), 50nm anti-EGFR gold/iron oxide nanoparticles (indicated by red arrows), and unlabeled cells (indicated by blue arrows) obtained using: (A) white light illumination; and (B) a 630±15nm bandpass filter. Images were acquired with a 20x darkfield/brightfield objective with a 0.5 collection NA. (C) Scattering spectra of cells labeled with 50 nm hybrid nanoparticles (red line), 40nm pure gold nanoparticles (green line) and of unlabeled cells (blue line). A fluorescent tag (AlexaFluor 488, Molecular Probes) was attached to the pure gold-antibody conjugates in order to differentiate between the two types of labeled cells.

6.4.3 Magnetic Actuation of Cells

Despite the unique contrast-enhancing mechanism afforded by the plasmon resonance coupling of gold nanoparticles, unlabeled cells can still be discerned in images obtained using both white light and red band-pass illumination (figures 6.3 A and B). To further increase contrast between labeled and unlabeled cells, we explored the magnetic component of the hybrid contrast agents. The experimental set-up for magnetic actuation of labeled cells (figure 6.2) is based on the following principles. The force exerted on the nanoparticles is proportional to the gradient of the square of the magnetic field magnitude [312], and acts in the direction of increasing gradient; thus the iron oxide nanoparticles tend to move towards the ferrite tip in the solenoid when current is applied. By oscillating the tip of the solenoid in a sinusoidal fashion in the horizontal or x-direction, the changing direction of force exerted on the nanoparticle-labeled cells causes an oscillating displacement in the cells' position. The magnitude of the oscillation was approximately 1 field of view, or 500 microns. Magnetically induced movement of cells labeled with iron-oxide/gold nanoparticles is shown in figure 6.4. Images were collected and replayed at 10 frames per second. As can be seen, the horizontal translation of the solenoid tip causes horizontal fluctuations in the cell position due to interaction between the electromagnet and the magnetic nanoparticles which are attached to EGFR molecules on cellular surface. In addition, however, there also exists a y-component of the magnetic force due to the fact that the ferrite tip is not positioned directly beneath the cell labeled with hybrid nanoparticles.

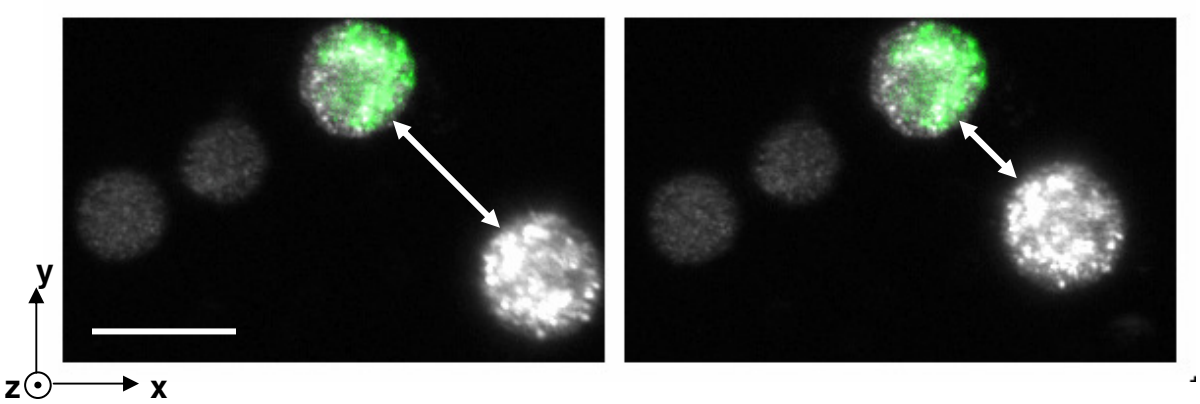

Figure 6.4. Two images, taken approximately 2 seconds apart, showing the magnetically induced movement of gold-iron oxide nanoparticle labeled A-431 cells captured under 20x magnification, and using a 635/15nm bandpass illumination filter. Note that there is no relative movement of unlabeled cells (which appear dim) and pure-gold labeled cells (identified by the overlaid green fluorescence signal). The magnetically labeled cell (bright with no overlaid green fluorescence) clearly responds to the oscillating magnetic by moving relative to the other cells, as indicated by the different sized arrows in both images. Scale bar is c. 20µm.

Cells that are not perfectly aligned in z-direction with the solenoid tip experience a non-oscillatory component in the y-direction. It is also important to note that the solenoid exerts the bulk of its force in the z-direction, parallel to the microscope's optical axis. While cell translation is confined in this direction due to the presence of the microscope slide and coverslip, it may produce an overall torque on cells that have an uneven angular distribution on particles on their surfaces. This will result in a torque, causing signal fluctuations at the same frequency as the solenoid oscillation, and thus will contribute to the overall magnetic actuation effect. Any significant signal fluctuations at the modulation frequency of the solenoid are absent in the case of unlabeled cells and cells labeled with pure gold nanoparticles or background.

6.4.4 Fourier Analysis of Cell Actuation Images

To analyze the specific frequency components of the acquired signals, a fast Fourier transform (FFT) was performed at each pixel of the acquired images in the time domain

and power spectra were calculated at each pixel position. Oscillation frequencies of the magnet and the total number of acquired images were chosen to avoid any aliasing effects. The precise sampling frequency was calculated via a time stamp generated in each image file that is accurate to 0.001 seconds. Figures 6.5(A) and (B) show monochrome darkfield images of a mixture of cells that are labeled with gold/iron oxide particles, with pure gold particles, as well as unlabeled cells, collected under 635/15nm bandpass illumination. The samples were subjected to a magnetic field oscillation with frequencies of 0.9Hz (A) and 1.9Hz (B). After data acquisition, images were analyzed in Matlab. Figures 6.5(C) and (D) show examples of frequency power spectra from magnetic gold labeled (red line), pure gold labeled (green line), and unlabeled cells (blue line), for magnetic oscillations with frequencies 0.9 and 1.9 Hz, respectively. Frequency spectra of signals recorded from cells labeled with the magnetic/gold nanoparticles display a prominent peak at the corresponding stage oscillation frequency. Such a peak is much less apparent in the case of unlabeled cells or cells labeled with pure gold nanoparticles, indicating that these cells are not displaced by the spatiotemporally oscillating magnetic field. These results also suggest that secondary effects such as localized temperature-induced convection currents within the gelatin matrix are minimal. Time-varying signal intensities are predominant in only those regions of interest which contain the magnetically labeled cells. To isolate magnetically modulated components in the acquired images, we used a Hanning window method implemented in Fourier space [327]. First, image series were subjected to the appropriate window function and, then, to an inverse Fourier transform at each pixel in the time-dimension. Finally, images were rescaled via a simple linear multiplier to maximize the pixel intensity range. It is

important to note that images were not subjected to any thresholding procedure (whereby a minimum pixel intensity is not displayed), which would artificially distort image contrast.

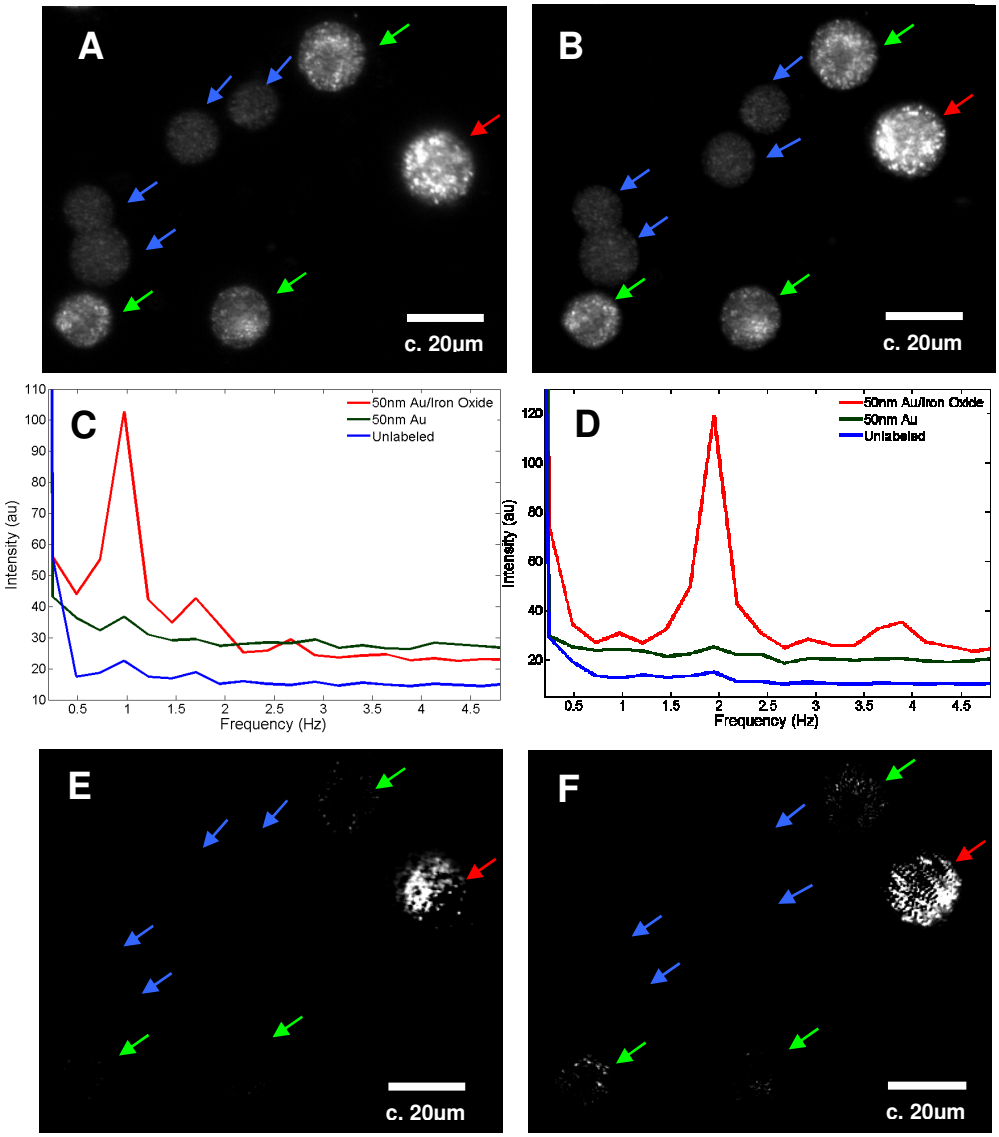

Figure 6.5 1:1:1 mixture of A-431 cells labeled with 40nm anti-EGFR gold nanoparticles (green arrows), 50nm anti-EGFR gold/iron oxide nanoparticles (red arrows), and unlabeled cells (blue arrows) that were magnetically actuated at 0.9Hz (A) and 1.9Hz (B) before application of a digital frequency filter. The images were obtained using a 635/15nm bandpass filter. Sections (C) and (D) show power spectra that are taken from the time-domain Fourier transform in the region containing a cell labeled with 50nm gold/iron oxide particles (red), 40nm pure gold particles (green) and an unlabeled cell (blue). Note the prominent peaks in the magnetically-labeled cells' frequency spectra that correspond to the translation stage oscillation frequencies of 0.9Hz (C) and 1.9Hz (D). Sections (E) and (F) show the same fields of view as sections (A) and (B), respectively, after digital filtering at 0.9Hz (E) and 1.9Hz (F) uses the Hanning function implementation. Only magnetically labeled cells are visible.

Figure 6.5(E) and (F) show the same fields of view as figure 6.5 (A) and (B), respectively, after digital filtering at the appropriate frequencies (0.9Hz and 1.9Hz) and rescaling. As a result of this treatment, signals associated with unlabeled cells, and pure gold-labeled cells are no longer apparent in images filtered at both 0.9Hz (figure 65 E) and 1.9Hz (figure 6.5 F).

6.4.5 Quantitation of Contrast Enhancement

The implementation of frequency domain filtering techniques results in greater contrast enhancement as compared to purely optical methods. To demonstrate this contrast enhancement quantitatively, pixel intensity profiles were drawn across images of magnetic gold-labeled (red line), pure-gold labeled (green line) and unlabeled cells (blue line) which were obtained under different illumination conditions and with the combination of the 635 nm illumination and frequency domain filtering (figure 6.6A). We also calculated the average signal intensities for each of the three cell populations in images that were acquired under four different acquisition and processing conditions: (1) white light illumination, (2) 635/15nm bandpass illumination, (3) white light illumination followed by magnetic actuation and frequency domain filtering, and (4) 635/15nm bandpass illumination followed by magnetic actuation and frequency domain filtering. Results of this analysis are shown in figures 6B and C. Under white light illumination, signal from cells labeled with magnetic and non-magnetic gold particles are statistically identical and the unlabeled cells are on average 2.5 times dimmer. Addition of the 635/15nm bandpass filter increases the intensity difference between labeled and unlabeled cells to approximately 4 (figure 6B). Interestingly, implementation of magnetic actuation and frequency domain filtering leads to statistically the same results

independent of which illumination condition is used, as shown in figure 6C. The average signal intensity ratio between gold/iron oxide and pure gold labeled cells increases from approximately 1 in the case of no magnetic actuation to about 3 with the magnetic actuation. At the same time, the intensity ratio between gold/iron oxide labeled cells and unlabeled cells increases from approximately 2.5-3 to *ca.* 10 under both illumination conditions. Asterisks in figure 6B and C indicate a statistically significant difference in the average signal values with $p<10^{-4}$ between the three cell types within each acquisition condition. These results demonstrate that frequency domain filtering is very sensitive to the magnetically controlled movement of cells.

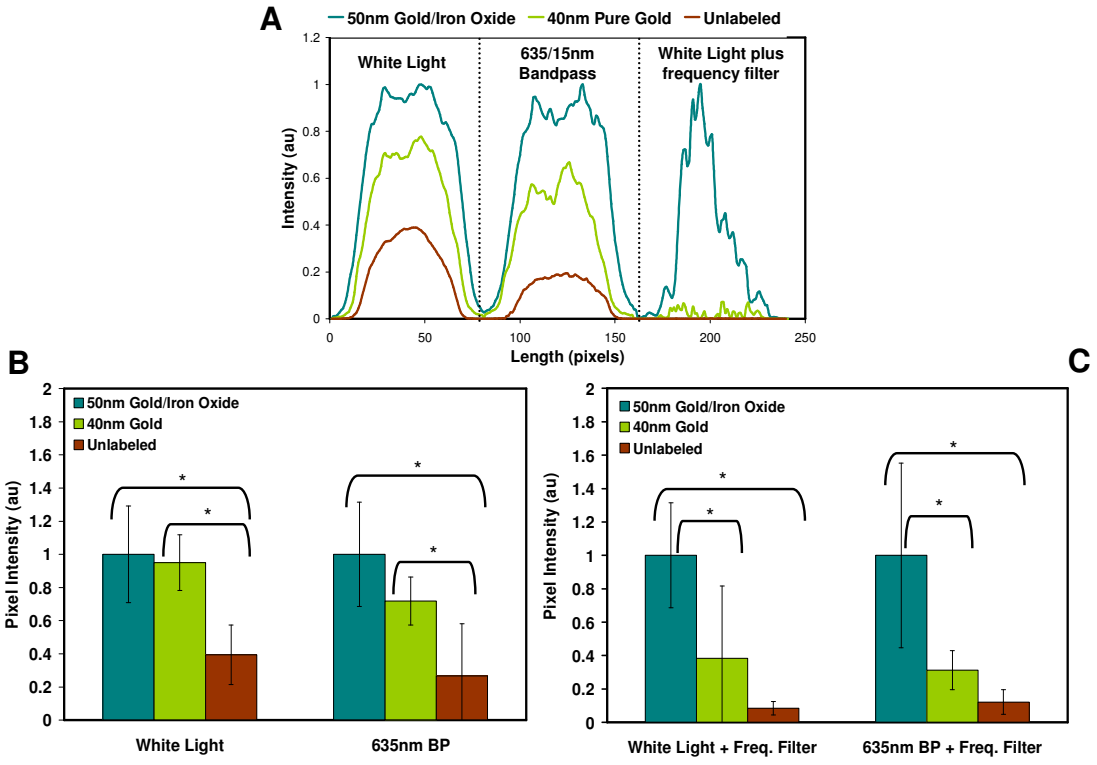

Figure 6.6 In (A), pixel intensity profiles are shown for the three cell types: 50nm gold/iron oxide labeled (red line), 40nm pure gold labeled (green line), and unlabeled (blue line). Profiles are drawn for the same three cells captured using white light illumination, 635/15nm bandpass illumination, as well as bandpass plus magnetic actuation and digital frequency filtering. In (B) and (C), the relative average pixel intensity from n>10 cells in each cell population and illumination/acquisition condition is compared. Asterisks and brackets in (B) and (C) indicate a statistical significant difference of the average signal values with $p<10^{-4}$.

6.5 DISCUSSION

The use of nanoparticle technology affords a flexible platform for interrogation of biological systems at the molecular level. Remaining barriers exist towards realizing a robust and generalized tool set that could potentially be used in molecular biology and healthcare settings. While issues such as biocompatibility and toxicity are of paramount importance, the ability of nanoparticle-based exogenous contrast agents to generate strong easily detectable signals which are above the endogenous background requires further investigation. For example, in fluorescence imaging techniques, background autofluorescence can present a difficult barrier to overcome [180]. Further, photobleaching can drastically reduce the ability to monitor longer-term molecular processes or response to therapies.

High background scattering from various tissue architecture can make the isolation of molecular specific signals difficult in reflected/scattered light imaging modalities such as reflectance confocal microscopy and OCT. Therefore, the development of multi-faceted approaches is essential to improve the sensitivity of molecular imaging techniques. Here we demonstrate that the combination of plasmon resonance scattering inherent in gold nanoparticles with magnetic actuation results in ca. 10 fold intensity ratio between the labeled and unlabeled cells under white light illumination; this is almost a four times increase over the same ratio for the pure gold nanoparticles. Also, under optimized bandpass illumination the magnetically actuated cells appear 3 times brighter than cells labeled with pure gold nanoparticles after application of the digital filtering (figure 6.6C). We demonstrate this new approach in A-431 skin cancer cells. These cells are keratinocytes which produce massive amounts of cytokeratin and, therefore, strongly scatter visible light. We chose this less than deal biological model because of the very

high endogenous scattering in order to evaluate the new approach in the presence of a high background signal. Our results indicate that magnetic actuation of these hybrid nanoparticles may be used to drastically reduce signals from non-magnetically susceptible background sources. This ability may be vital in potential future *in-vivo* molecular imaging applications, where it is crucial to isolate the distribution of molecules of interest from a dense, highly complex background. Interestingly we note that our results also showed that hybrid magnetic gold nanoparticles can be easily distinguished from pure gold nanoparticles using magnetic actuation. This opens the possibility of a multiplexing approach that uses combinations of magnetic and non-magnetic gold particles in molecularly labeling distinct sub-populations of cells. Further, the analysis algorithm can potentially be incorporated such that Fourier-based filtering can be accomplished in near-real time. There are a number of other potential applications whereby magnetically actuated hybrid particles may be applied. The ability to both magnetically manipulate and monitor cells on the nano-scale with molecular specificity is an exciting direction for further research. For example, pure magnetic nanoparticles (MNPs) were used to probe the mechanical properties of proteins both separately and inside cells [328-330]. However, these studies are still limited by micron size of these particles and their relatively low brightness. The magnetically actuated plasmonic nanoparticles can drastically improve the spatial resolution of these studies and signal-to-noise ratio in monitoring of a mechanical response. Further, the field of molecular-specific mechanotransduction may greatly benefit from the ability to both mechanically manipulate cells using an external magnetic field and monitor cellular response in real time with a single agent.

6.6 ACKNOWLEDGEMENTS

The author would like to thank Dr. Junghwan Oh for fabrication, testing, and operation of the magnetic solenoid. Also, thanks go to Dr. Tom Milner for support and valuable discussions. Funding from the NSF IGERT program, as well as support from the NCI is gratefully acknowledged.

CHAPTER 7:

Conclusions and Future Directions

7.1 CONCLUSIONS

As was shown in Chapter 3, cells labeled with anti-EGFR gold nanoparticles display a plasmon resonance peak that can be shifted over 100nm from that seen in solution, into the red and near infrared spectral regions. This, in combination with coherent back scattering effects that non-linearly increase the overall optical cross section of the system, produce a bright characteristic scattering signal from EGFR over-expressing cells. The red shifting and coherent back scattering effects were shown independently via hyperspectral imaging, and bi-functional fluorescence/reflectance contrast agents, respectively. Red shifting of the plasmon resonance is an active area of theoretical investigation. From a simplified point of view, it can be seen that a particle pair whose longitudinal axis is parallel to the electric field polarization experiences a relaxation in the energy required to initiate the conduction band electron oscillation – thus producing a red shift in their collective resonance. It has been shown that this dipole-dipole coupling depends on the cube of the interparticle distance [197] . Subsequent examination of labeled cells in electron microscopy images shows that these inter-particle distances are well within the range where plasmon coupling is prominent, deemed to be less than three times the diameter [197].

Further investigations in Chapter 4 indicate that the degree of plasmon coupling is intimately intertwined with the trafficking events that are a part of the EGFR life cycle within the cell. Cells labeled at low temperatures, where endocytosis is inhibited, show far less red-shifting than those labeled at higher temperatures. Further electron

microscopy investigations confirm that the these spectral changes are a result of the increase in inter-particle spacing, as well as a shift into three dimensional organization due to endocytosis. These studies showed conclusively that metal nanoparticles are sensitive to the nanoscale arrangement of EGFR molecules. However, a unified view that relates the degree of plasmon coupling to specific molecular events such as receptor dimerization [331], clustering in clathrin coated pits [134], as well as endosomal fusion and degradation is still an ongoing process [137].

When this technology is applied to more complex biological models, a system of delivery becomes a major factor of consideration. Adjuvants such as DMSO may play a critical role in aiding the delivery of nanoparticles topically, and experimentation with various complex pre-clinical models bears this out, as shown in Chapter 5. Large differences in signal are seen between normal and abnormal cervical biopsies, and this contrast monotonically increases with the severity of the neoplastic growth. Critical questions remain, however, as to the eventual adoption of such a strategy into clinical use. Questions remain as to whether effects such disease-modulated increases in tissue permeability translate into an additional reliable means to target abnormal cells *in-vivo*, or whether it will result in highly variable and unpredictable results from patient to patient. Certainly, a more thorough investigation is needed in this regard. In addition, exploring the use of metal nanoparticles in cases of advanced metastatic disease has certainly been encouraged from the initial results seen in Chapter 5. However, there remains much further work in identifying strategies and limitations for sentinel lymph node detection.

As was shown in chapter 5, as well, was the tendency of some tissues to exhibit less than ideal morphology and organization. This might include high keratin expression which seems to block delivery of nanoparticles as well as light, as well as other endogenous sources of signal such as immuno-induced fibrotic encapsulation. These few examples demonstrate the nature of biological tissue as being highly complex, heterogeneous, and often difficult environments in which to image. As such, a multifaceted approach may be necessary to extract the requisite amount of information from a sample. Chapter 6 outlines an example of such an approach, whereby molecular specific signal is modulated by means of an oscillating magnetic field and a plasmonic/magnetically susceptible nanoparticle. This provides an "encoding" mechanism that allows extraction of the signal of interest from a noisy or large background.

The overriding aim of the studies presented in this dissertation is to establish paradigms for future work to continue evaluating the use of immuno-targeted gold nanoparticles for optical molecular imaging. In particular, this work demonstrates the importance of the concept of plasmon coupling as a valuable and unique mechanism for optical molecular imaging. As evidenced by the number of publications that have appeared in the last 4-6 years, optical molecular imaging is fast becoming a major field in biomedicine [60, 144, 171, 245, 332-334]. From these studies and others, plasmonics certainly has a vital role to play in these efforts [264, 280, 335, 336]. Their strong signal due to large electromagnetic enhancement, resistance to photobleaching, and straightforward conjugation to targeting moieties makes these types of nanomaterials very attractive for biological interfacing devices. Surface plasmon coupling, while

recognized as a physical phenomenon for some time [74, 191], has not until recently been shown to be useful in a biological sensing arena [71], albeit so far in the simplest form of a single pair of interacting particles isolated *in-vitro* for detection of DNA behavior. While exciting, we believe the studies described in this dissertation serve to vastly expand the feasibility of this concept to reliably sense protein assemblies *in-situ*, and *in-vivo*, thereby making this technology much more widely applicable and useful.

7.2 FUTURE DIRECTIONS

The future opportunities for further development of this technology are wide ranging., as evidenced by the number of new avenues of research that are being put forth. As was briefly mentioned in the previous section, there are two main areas which certainly deserve further examination. First is development of a better understanding of the biomolecular trafficking and activation events incorporated into the EGFR life cycle, and how these affect plasmon coupling. Or, conversely, to what extent can plasmon coupling be used to image and understand the nanoscale relationship of molecules such as EGFR in and on the cell? The second main area would be to further explore and develop delivery mechanisms for eventual adoption of plasmonic nanoparticles into clinical practice. While data have been encouraging, the effects of cancer on tissue permeability and biomarker access are still largely unknown. There certainly may be alternative delivery strategies and techniques that may increase the overall clinical applicability and performance, such as systemic delivery, or more bio-specific delivery strategies such as viral or other pathogenically derived strategies.

In the longer term, there are potential expansions of the current state of the art that will make plasmonics even more attractive from both a clinical and biological

perspective. Firstly, the use of hybrid nanoparticles was demonstrated in Chapter 6. Similar particles may be used as dual imaging contrast agents in both MRI and optical measurements. This has the distinct advantage of exploiting the large imaging volumes inherent in MRI, and the high resolving power using optics, and again underscores the need for multifaceted approaches in molecular imaging. Finally, plasmonic devices can act as both passive reporters, as well active agents of intervention in cells. Synthesizing optical diagnostics and photothermal treatment of diseased tissue, or magnetically induced mechanotransduction may open up nearly limitless applications. In short, it is not likely that potential new applications of plasmonics in biology will be exhausted in the near term.

APPENDIX

Imaging Chamber Design: Top Clamp

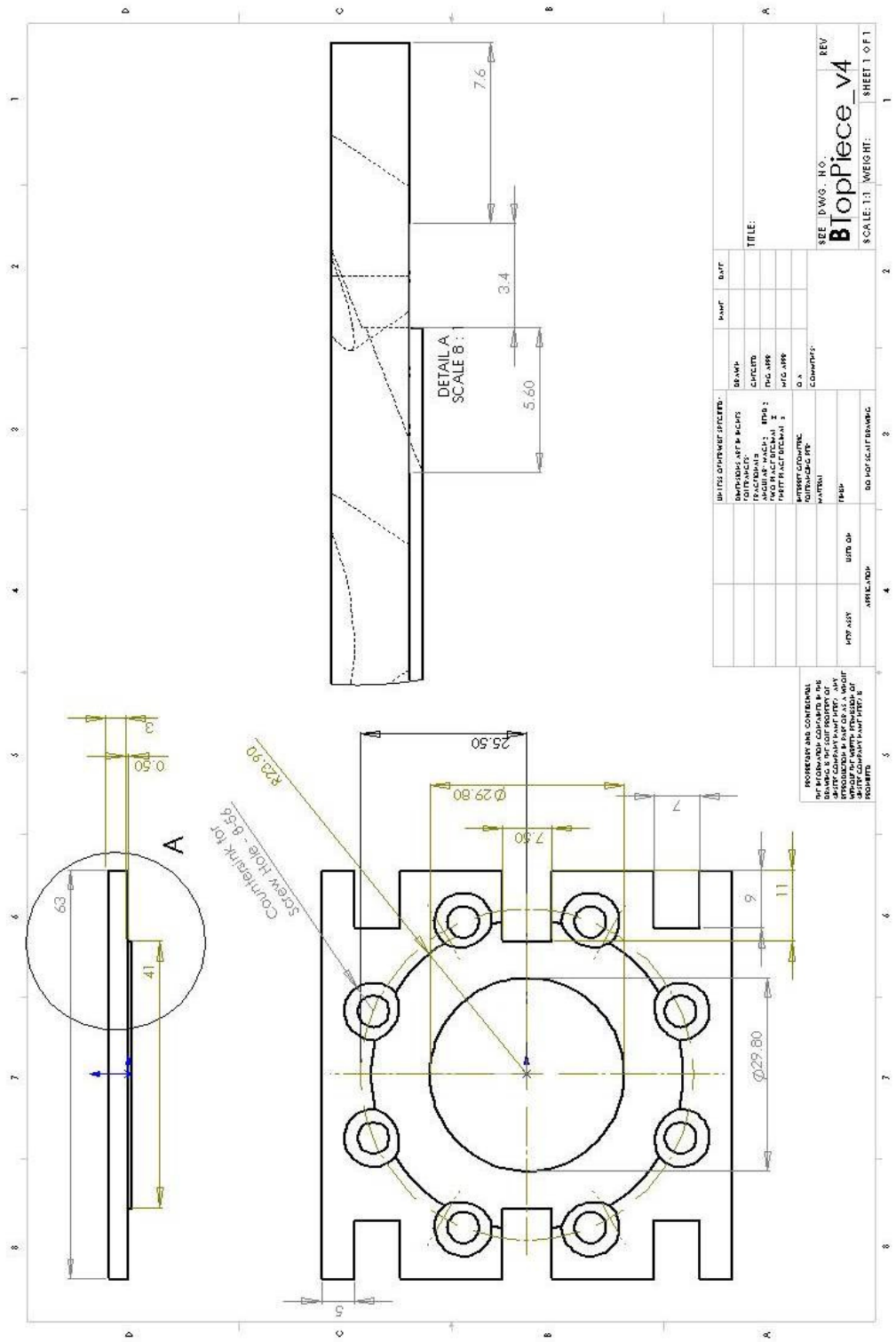

Imaging Chamber Design: Bottom Clamp

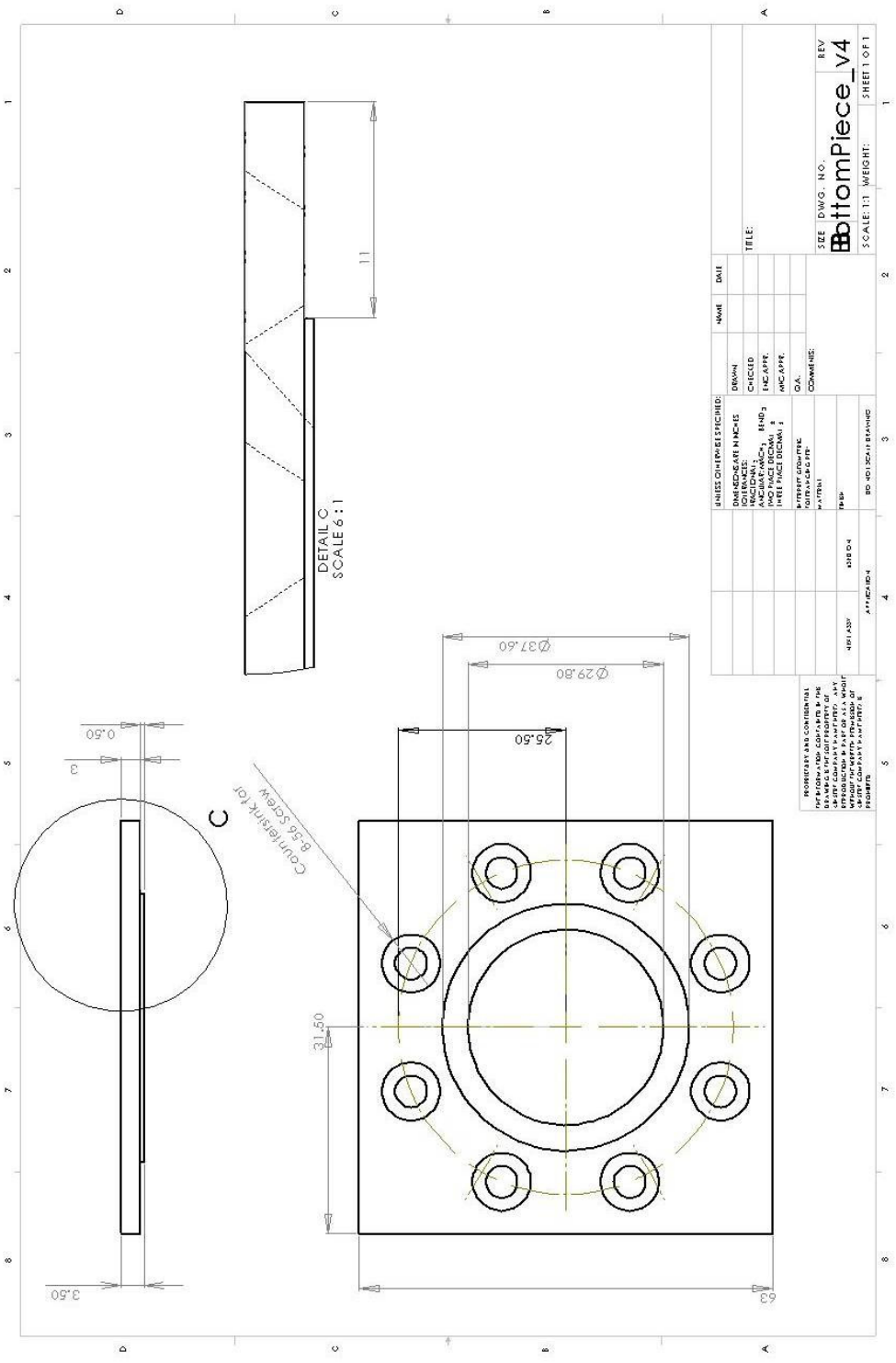

Imaging Chamber Design: Central Chamber

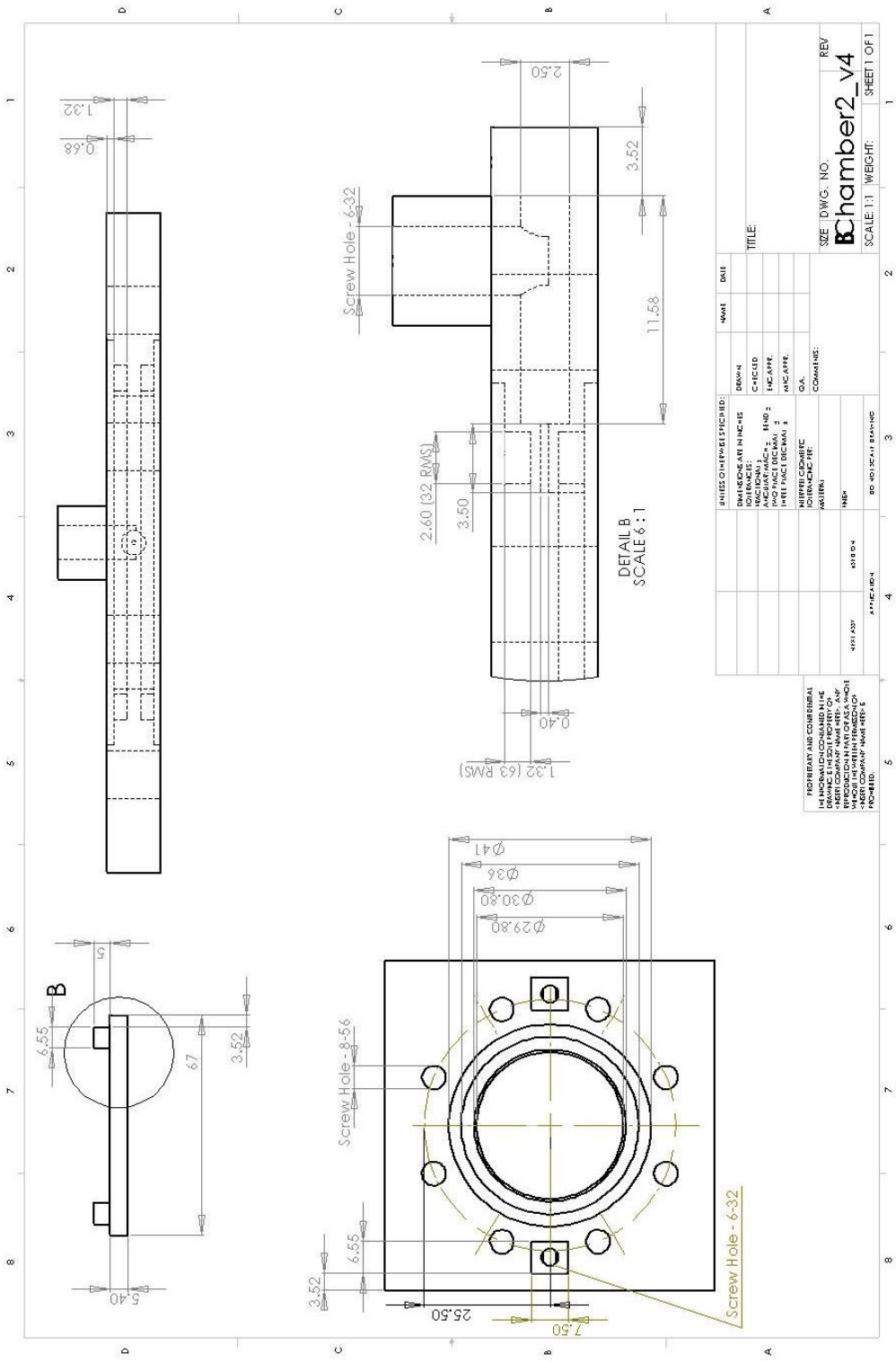

```
%PARISS hyperspectral data cube builder
%by Jesse Aaron
%Last Update Feb. 2007
%_____________________________________________________________________
%
%This program will import PARISS hyperspectral data to a .mat file.  The
%data must be fist converted from .prs to .txt format using Jeremy's LabView
%conversion utility before running this m-file.  This program prompts user
%for a Sample data directory and a Normalization data directory (they must
%be different).  If the data does not require normalization, press cancel
%when prompted for the normalization image.
%
%The program outputs are p (the hyperspectral data cube), lam (the
%wavelength vector), and date (the date/time the data was acquired).

clear all; close all; home
datapath = uigetdir('C:','Select Directory Containing Sample Data .txt Files');
whitepath = uigetdir(datapath,'Select Directory Containing Mirror Spectra .txt File.
Press Cancel If None');
stdpath = uigetdir(datapath,'Select Directory Containing Mirror Standard .txt File.
Press Cancel If None');
filelist = dir(fullfile(datapath,'*.txt'));

%Import & normalize using a "perfect" substrate (such as labsphere or Al mirror)
if (whitepath(1) ~= 0) & (stdpath(1) == 0)
    white = dir(fullfile(whitepath,'*.txt'));
    numw = textread(fullfile(whitepath,white.name),'%f','headerlines',1);
    numw = reshape(numw,241,1,length(numw)/241);
    pw = numw(2:size(numw,1),1,:);
    clear numw
%Import and normalize using a "standard" substrate (such as gold mirror)
elseif (whitepath(1) ~= 0) & (stdpath(1) ~= 0)
    white = dir(fullfile(whitepath,'*.txt'));
    numw = textread(fullfile(whitepath,white.name),'%f','headerlines',1);
    numw = reshape(numw,241,1,length(numw)/241);
    stand = dir(fullfile(stdpath,'*.txt'));
    nums = textread(fullfile(stdpath,stand.name),'%f','headerlines',1);
    nums = reshape(nums,241,1,length(nums)/241);
    pw = numw(2:size(numw,1),1,:)./nums(2:size(nums,1),1,:);
    clear numw nums
%Import without any normalization (such as fluorescence or raw spectra)
elseif (whitepath(1) == 0) & (stdpath(1) == 0)
    pw = 1;
end

%Copy and read .txt files (must be in their own directory)
for a = 1:length(filelist)
    num = textread(fullfile(datapath,filelist(a).name),'%f','headerlines',1);
    num = reshape(num,241,1,length(num)/241);
    rawdata = num(2:size(num,1),1,:);
    warning('off');
    normdata = rawdata./pw;
    clear rawdata
    p(:,a,:) = normdata;
    clear normdata
    progress = round(a/length(filelist)*1000)/10;
    home
    disp(strcat('progress:',num2str(progress),'%'));
end

%Pre-processing of data
p = p(:,:,46:446); %only consider data from 400-800nm (outside this range is too noisy)
p(isnan(p) == 1) = 0; p(isinf(p) == 1) = 0; %get rid of any divide-by-zero errors
lam = num(1,1,:); lam = reshape(lam,1,size(lam,3)); %construct wavelength vector
lam = lam(46:446); %make wavelength vector match cropped data (400-800nm)
date = filelist(a).date; %provide acquisition time
clear num pw filelist %clean up memory
pack %clean up memory
```

```
%Wavelength intensity plot
%By Jesse Aaron
%Last update Oct. 2006
%_____________________________________________________________________________
%
%[IMG] = INTPLOT(P,LAM,LAMBDA,CLIM)
%
%This function plots the intensity of a hyperspectral image at given
%wavelength.
%
%The inputs are:
%
%p: The hyperspectral data as generated by hyperspec.m
%
%lam:  The wavelength vector as generated by hyperspec.m
%
%lambda: The approximate wavelength or wavelength range at which to view
%        the intensity.  In the case of a range of wavelengths, input the first and
%        last wavelengths to consider in vector form.  The image will show the integrated
%        signal over this range.
%
%clim: A 2-element vector that gives the min and max values to display in
%      the image.  If clim is set to zero, the limits will automatically
%      be set to the min and max of the image.
%
%The output is:
%
%A image that contains the intensity image.  This can be saved as a
%.fig file or exported as a .tif file.

function [img] = intplot(p,lam,lambda,clim)
%find nearest wavelength point to input
mindiff = abs(lam - min(lambda));
maxdiff = abs(lam - max(lambda));

%single wavelength case
if  mindiff(1) == maxdiff(1)
    diff = mindiff;
    index = find(diff == min(diff));
    img = p(:,:,index);

%wavelength range case
else
    index1 = find(mindiff == min(mindiff));
    index2 = find(maxdiff == min(maxdiff));
    pimg1 = p(:,:,min(index1,index2):max(index1,index2));
    img = sum(pimg1,3);
end

%default setting if clim = 0
if clim == 0
    clim = [min(min(pimg)) max(max(pimg))];
else
end

%create image
figure
imagesc(img,clim); hold on
colorbar
axis image
axis off
if mindiff(1) == maxdiff(1)
    ttl = ['Intensity at ',num2str(round(lam(index))),' nm'];
else
    ttl = ['Integrated intensity from ' num2str(round(lam(index1))) ' to '
num2str(round(lam(index2))) ' nm'];
end
title(ttl)
hold off
clear pimg1
```

```
%Spectra plot for PARISS(R)
%By Jesse Aaron
%Last update Oct. 2006
%_____________________________________________________________________
%
%[IMG,INT,LAM] = SPECTRAPLOT(P,LAM,COORDX,COORDY,SMOOTHING)
%
%This function plots the spectra from within a given ROI in a hyperspectral
%image.  The inputs are:
%
%p:  The hyperspectra data as generated by hyperspec.m
%
%lam: The wavelength vector as generated by hyperspec.m
%
%coordx:  The x-coordinate of the ROI.  It can be a single value, or a range
%         covering more than one pixel in the x (horizontal) direction.  If
%         set to zero, it will allow user to select a ROI using a mouse.
%
%coordy:  The y-coordinate of the ROI. It can be a single value, or a range
%         covering more than one pixel in they y (vertical) direction. If
%         set to zero, it will allow user to select a ROI using a mouse.
%
%smoothing:  Set to zero for no smoothing, set to 1 for moving average or
%            "boxcar" smoothing.  Default window size is 5nm.
%
%The outputs are:
%
%A matlab figure showing the Intensity vs. wavlength plot.
%
%A .xls file containing the data for later plotting.  Int is the intensity,
%lam is the wavelength vector.
%
function [img,Int,lam] = spectraplot(p,lam,coordx,coordy,smoothing);
p2 = reshape(p(:,:,151),size(p,1),size(p,2)); %show intensity image at 550nm
if (coordx == 0) & (coordy == 0)
    imagesc(p2,[0 2]); hold on; axis image; colorbar
    rect = getrect(gcf); x = round([rect(1) rect(1)+rect(3)]); y = round([rect(2)
rect(2)+rect(4)]);
else
    x = [min(coordx) max(coordx)]; y = [min(coordy) max(coordy)];
end

spx = p(y(1):y(2),x(1):x(2),:);
spx_ave = mean(mean(spx,1),2);
spec = reshape(spx_ave,1,size(p,3));

if smoothing == 1
    spec = moving_average(spec,5);
else
end

figure; plot(lam,spec); hold on
xlabel('Wavelength (nm)'); ylabel('Intensity (au)');
xlim([400 800]); ylim('auto');
hold off

data = [lam' spec'];
xlswrite('spectraplot.xls',data);
[filename path] = uiputfile('.xls','Save Spectral Data in .xls File');
Int = spec;
if filename ~= 0
    movefile('spectraplot.xls',filename);
else
end

if (path ~= 0) & (strcmp(cd,path) ~= 1)
    movefile(filename,path,'f');
else
end
```

```
function [maxtab, mintab]=peakdet(v, delta)
%PEAKDET Detect peaks in a vector
%        [MAXTAB, MINTAB] = PEAKDET(V, DELTA) finds the local
%        maxima and minima ("peaks") in the vector V.
%        A point is considered a maximum peak if it has the maximal
%        value, and was preceded (to the left) by a value lower by
%        DELTA. MAXTAB and MINTAB consists of two columns. Column 1
%        contains indices in V, and column 2 the found values.

% Eli Billauer, 3.4.05 (Explicitly not copyrighted).
% This function is released to the public domain; Any use is allowed.

maxtab = [];
mintab = [];

v = v(:); % Just in case this wasn't a proper vector

if (length(delta(:)))>1
  error('Input argument DELTA must be a scalar');
end

if delta <= 0
  error('Input argument DELTA must be positive');
end

mn = Inf; mx = -Inf;
mnpos = NaN; mxpos = NaN;

lookformax = 1;

for i=1:length(v)
  this = v(i);
  if this > mx, mx = this; mxpos = i; end
  if this < mn, mn = this; mnpos = i; end

  if lookformax
    if this < mx-delta
      maxtab = [maxtab ; mxpos mx];
      mn = this; mnpos = i;
      lookformax = 0;
    end
  else
    if this > mn+delta
      mintab = [mintab ; mnpos mn];
      mx = this; mxpos = i;
      lookformax = 1;
    end
  end
end
```

```
%Maximum wavelength plot
%By Jesse Aaron
%Last update Feb. 2007
%_____________________________________________________________________________
%
%[IMG2] = MAXLAM(P,LAM,THRESHL,THRESHU,CLIM)
%
%This function finds the highest peak (local maximum) in each spectrum (within a range of
wavelengths)
%and plots an image of the peak wavelengths at each pixel, represented by a RGB color
map.
%
%The inputs are:
%
%p:  The hyperspectra data cube as generated by hyperspec.m
%
%lam:  The wavelength vector as generated by hyperspec.m
%
%threshl:  The lower signal threshold that will be considered.
%
%threshu:  The upper signal threshold that will be considered.
%
%clim:  The wavelength range over which to look for peaks.
%
%delta:  The sensitivity of the peak detection (0.1 is a good value).
%
%The output is:
%
%An image that contains the maximum wavelength image.  This can be saved as a
%.fig file or exported as a .tif file.

function [img2] = maxlam(p,lam,threshl,threshu,clim,delta);

diff1 = abs(lam - min(clim));
diff2 = abs(lam - max(clim));
index1 = find(diff1 == min(diff1));
index2 = find(diff2 == min(diff2));

%threshold image
maxpthresh = p(:,:,151).*(p(:,:,151) < threshu).*(p(:,:,151) > threshl);

%find pixel positions of non-zero results
[x1 y1] = find(maxpthresh ~= 0);

%skeleton image
img2 = zeros(size(p,1),size(p,2));

for a = 1:length(x1)
   spec = reshape(p(x1(a),y1(a),:),1,length(lam)); %1D spectrum
   spec = moving_average(spec,5);
   [maxtab] = peakdet(spec,delta);
   peaktab = [lam(maxtab(:,1))' maxtab(:,2)];
   inrange = find(peaktab(:,1) > lam(index1) & peaktab(:,1) < lam(index2));
   peaktab = peaktab(inrange,:);
   if isempty(inrange) == 1
       peak = lam(1);
   else
       highest = find(peaktab(:,1) == max(peaktab(:,1)));
       peak = peaktab(highest,1);
   end
   img2(x1(a),y1(a)) = peak;
end

cmap = colormap;
cmap(1,:) = [0 0 0];

imagesc(img2,[min(lam)-10 max(lam)]); hold on
colormap(cmap); colorbar('horiz');
axis image
axis off
```

```
%Maximum wavelength histogram maker
%By Jesse Aaron
%Last update Feb. 2007
%_____________________________________________________________________________
%
%[N,X] = MAXHIST(P,LAM,THRESH,CLIM)
%
%This function generates a histogram of wavelengths corresponding to
%maximum signal intensities in an image.  The histogram can be generated
%for a user-selectable ROI in the image using the mouse.
%
%The inputs are:
%
%p:  The hyperspectral data cube as generated by hyperspec.m
%
%lam:  The wavelength vector as generated by hyperspec.m
%
%threshl:  Lower signal threshold to consider
%
%
%clim:  Wavelength range to plot in the histogram.  If clim is set to zero,
%       the the limits will automatically be set to the min and max of the image.
%
%delta:  The sensitivity of the peak detection. (0.1 is a good value)
%
%bin:  The histogram bin size (in nm).
%
%The outputs are:
%
%A .fig file that shows the frequency histogram of the maximum intensity
%wavelengths.
%
%A .xls file which can be saved containing the wavelength vs. frequency
%data. N is the frequencies, x is the bin center values.

function [N,x,stats] = maxhist(p,lam,threshl,threshu,clim,delta,bin);

img2 = maxlam(p,lam,threshl,threshu,clim,delta);

rect = round(getrect(gcf));
x = [rect(1) rect(1)+rect(3)]; y = [rect(2) rect(2)+rect(4)];
roi = img2(y(1):y(2),x(1):x(2));
list = reshape(roi,size(roi,1)*size(roi,2),1);
zeroind = find(list == 0); list(zeroind) = [];%get rid of zeros
climind = find(list < min(clim) | list > max(clim));%get rid of peaks outside range
list(climind) = [];
[N,x] = hist(list,[min(clim):bin:max(clim)]);
ave = mean(list);
medianval = mode(list);
stdev = std(list);
stats = {'Average' ave; 'Sigma' stdev; 'Median' medianval};

figure; hist(list,[min(clim):bin:max(clim)]); hold on
title(['Mean = ' num2str(round(ave)) '  Stdev = ' num2str(round(stdev*100)/100) ' Median
= ' num2str(round(medianval))]);
xlabel('Peak Wavelength (nm)'); ylabel('Frequency');
hold off;
data = [N' x'];
xlswrite('histogram.xls',stats);
xlswrite('histogram.xls',data,1,'A5');
[filename pathname] = uiputfile('*.xls','Save Histogram Data');
if filename ~= 0
    movefile('histogram.xls',filename);
else
end

if (pathname ~= 0) & (strcmp(cd,pathname) ~= 1)
    movefile(filename,pathname,'f');
else
    end
```

REFERENCES:

1. "Cancer Statistics 2006: A presentation from the American Cancer Society," (2006), www.cancer.org/downloads/STT/Cancer_Statistics_2006_Presentation.ppt, Accessed March 19th, 2007.
2. A. Mezzogiorno, and V. Mezzogiorno, "Marcello Malpighi (1628-1694)." American Journal of nephrology **17**, 269-273 (1997).
3. M. Pines, *Inside the Cell* (DIANE Publishing - U.S. Dept. HHS, Washington, DC, 1993).
4. J. M. Fenster, *Mavericks, Miracles, and Medicine: The pioneers who risked their lives to bring medicine into the modern age* (Carroll & Graf, New York, NY, 2003).
5. J. D. Bancroft, and M. Gamble, *Theory and Practice of Histological Techniques* (Elsevier, Amsterdam, The Netherlands, 2001).
6. J. L. Prince, and J. M. Links, *Medical Imaging Singals and Systems* (Pearson Prentice Hall, Upper Saddle River, NJ, 2006).
7. D. Hanahan, and R. A. Weinberg, "The hallmarks of cancer," Cell (Cambridge, Massachusetts) **100**, 57-70 (2000).
8. S. Sevush, and L. J. Turkewitz, "Brain biopsy: risks, benefits, and indications," Mt Sinai J Med FIELD Full Journal Title:The Mount Sinai journal of medicine, New York **52**, 380-383. (1985).
9. A. Hengerer, and J. Grimm, "Molecular magnetic resonance imaging," Biomedical Imaging and Intervention Journal **2**, No pp. given (2006).
10. A. P. Pathak, "Magnetic resonance imaging of tumor physiology," Methods in Molecular Medicine **124**, 279-297 (2006).
11. U. Mahmood, and L. Josephson, "Molecular MR imaging probes," Proceedings of the IEEE **93**, 800-808 (2005).
12. G. Rajendran Joseph, and E. Greer Benjamin, "Expanding role of positron emission tomography in cancer of the uterine cervix," J Natl Compr Canc Netw FIELD Full Journal Title:Journal of the National Comprehensive Cancer Network : JNCCN **4**, 463-469. (2006).
13. J. Manyak Michael, M. Javitt, S. Kang Pil, R. Kreuger William, and S. Storm Erik, "The evolution of imaging in advanced prostate cancer," Urol Clin North Am FIELD Full Journal Title:The Urologic clinics of North America **33**, 133-146, v. (2006).
14. E. Heron Dwight, P. Smith Ryan, and S. Andrade Regiane, "Advances in image-guided radiation therapy--the role of PET-CT," Med Dosim FIELD Full Journal Title:Medical dosimetry : official journal of the American Association of Medical Dosimetrists **31**, 3-11. (2006).
15. P. Shreve, "Establishing a PET/CT practice," AJR Am J Roentgenol FIELD Full Journal Title:AJR. American journal of roentgenology **184**, S146-151. (2005).
16. S. V. Egerev, O. B. Ovchinnikov, A. V. Fokin, V. V. Klimov, D. Huzatau, A. P. Kanavin, and A. A. Oraevsky, "Pulsed optoacoustic interaction in suspension of gold nanoparticles: detection sensitivity based on laser-induced nanobubbles," Proceedings of SPIE-The International Society for Optical Engineering **5697**, 73-81 (2005).
17. A. Briel, M. Reinhardt, M. Maeurer, and P. Hauff, "Ultrasound theranostics: antibody-based microbubble conjugates as targeted in vivo contrast agents and advanced drug delivery systems," (2005), pp. 1301-1324.
18. J. P. Christiansen, and J. R. Lindner, "Molecular and cellular imaging with targeted contrast ultrasound," Proceedings of the IEEE **93**, 809-818 (2005).
19. A. L. Klibanov, "Ligand-Carrying Gas-Filled Microbubbles: Ultrasound Contrast Agents for Targeted Molecular Imaging," Bioconjugate Chemistry **16**, 9-17 (2005).
20. P. Heppner, and R. Lindner Jonathan, "Contrast ultrasound assessment of angiogenesis by perfusion and molecular imaging," Expert Rev Mol Diagn FIELD Full Journal Title:Expert review of molecular diagnostics **5**, 447-455. (2005).
21. S. M. Moghimi, "Particulate Nanomedicines," Advanced Drug Delivery Reviews **58**, 1451-1455 (2006).
22. A. P. Alivisatos, "Semiconductor clusters, nanocrystals, and quantum dots," Science (Washington, D. C.) **271**, 933-937 (1996).
23. W. C. Chan, and S. Nie, "Quantum dot bioconjugates for ultrasensitive nonisotopic detection," Science **281**, 2016-2018. (1998).
24. X. Gao, W. C. W. Chan, and S. Nie, "Quantum-dot nanocrystals for ultrasensitive biological labeling and multicolor optical encoding," Journal of Biomedical Optics **7**, 532-537 (2002).

25. Y. Zhu, J. Shi, W. Shen, H. Chen, X. Dong, and M. Ruan, "Preparation of novel hollow mesoporous silica spheres and their sustained-release property," Nanotechnology **16**, 2633-2638 (2005).
26. L.-X. Wen, H.-M. Ding, J.-X. Wang, and J.-F. Chen, "Porous hollow silica nanoparticles as carriers for controlled delivery of ibuprofen to small intestine," Journal of Nanoscience and Nanotechnology **6**, 3139-3144 (2006).
27. F. Balas, M. Manzano, P. Horcajada, and M. Vallet-Regi, "Confinement and Controlled Release of Bisphosphonates on Ordered Mesoporous Silica-Based Materials," Journal of the American Chemical Society **128**, 8116-8117 (2006).
28. S. Giri, B. G. Trewyn, and V. S. Y. Lin, "Mesoporous silica nanomaterial-based biotechnological and biomedical delivery systems," Nanomedicine (London, United Kingdom) **2**, 99-111 (2007).
29. N. Gharbi, M. Pressac, M. Hadchouel, H. Szwarc, S. R. Wilson, and F. Moussa, "[60]Fullerene is a Powerful Antioxidant in Vivo with No Acute or Subacute Toxicity," Nano Letters **5**, 2578-2585 (2005).
30. S. J. Oldenburg, R. D. Averitt, S. L. Westcott, and N. J. Halas, "Nanoengineering of optical resonances," Chemical Physics Letters **288**, 243-247 (1998).
31. S. J. Oldenburg, G. D. Hale, J. B. Jackson, and N. J. Halas, "Light scattering from dipole and quadrupole nanoshell antennas," Applied Physics Letters **75**, 1063-1065 (1999).
32. C. Loo, A. Lin, L. Hirsch, M.-H. Lee, J. Barton, N. Halas, J. West, and R. Drezek, "Nanoshell-enabled photonics-based imaging and therapy of cancer," Technology in Cancer Research & Treatment **3**, 33-40 (2004).
33. C. H. Loo, M.-H. Lee, L. R. Hirsch, J. L. West, N. J. Halas, and R. A. Drezek, "Nanoshell bioconjugates for integrated imaging and therapy of cancer," Proceedings of SPIE-The International Society for Optical Engineering **5327**, 1-4 (2004).
34. C. Loo, A. Lowery, N. Halas, J. West, and R. Drezek, "Immunotargeted Nanoshells for Integrated Cancer Imaging and Therapy," Nano Letters **5**, 709-711 (2005).
35. R. Hirsch Leon, M. Gobin Andre, R. Lowery Amanda, F. Tam, A. Drezek Rebekah, J. Halas Naomi, and L. West Jennifer, "Metal nanoshells," Annals of biomedical engineering **34**, 15-22. (2006).
36. F. H. Wang, I. H. Lee, N. Holmstroem, T. Yoshitake, D. K. Kim, M. Muhammed, J. Frisen, L. Olson, C. Spenger, and J. Kehr, "Magnetic resonance tracking of nanoparticle labelled neural stem cells in a rat's spinal cord," Nanotechnology **17**, 1911-1915 (2006).
37. E. Taboada, E. Rodriguez, A. Roig, J. Oro, A. Roch, and R. N. Muller, "New ultrasmall iron-oxide nanoparticles with high magnetisation as potential T1-MRI contrast agents for molecular imaging," in *Los Alamos National Laboratory, Preprint Archive, Condensed Matter*(2006), pp. 1-27, arXiv:cond-mat/0611243.
38. T. Atanasijevic, M. Shusteff, P. Fam, and A. Jasanoff, "Calcium-sensitive MRI contrast agents based on superparamagnetic iron oxide nanoparticles and calmodulin," Proceedings of the National Academy of Sciences of the United States of America **103**, 14707-14712 (2006).
39. P. Smirnov, E. Lavergne, F. Gazeau, M. Lewin, A. Boissonnas, B.-T. Doan, B. Gillet, C. Combadiere, B. Combadiere, and O. Clement, "In vivo cellular imaging of lymphocyte trafficking by MRI: a tumor model approach to cell-based anticancer therapy," Magnetic Resonance in Medicine **56**, 498-508 (2006).
40. C. Sun, R. Sze, and M. Zhang, "Folic acid-PEG conjugated superparamagnetic nanoparticles for targeted cellular uptake and detection by MRI," Journal of Biomedical Materials Research, Part A **78A**, 550-557 (2006).
41. O. A. Garden, P. R. Reynolds, J. Yates, D. J. Larkman, F. M. Marelli-Berg, D. O. Haskard, A. D. Edwards, and A. J. T. George, "A rapid method for labeling CD4+ T cells with ultrasmall paramagnetic iron oxide nanoparticles for magnetic resonance imaging that preserves proliferative, regulatory and migratory behaviour in vitro," Journal of Immunological Methods **314**, 123-133 (2006).
42. T. Tallheden, U. Nannmark, M. Lorentzon, O. Rakotonirainy, B. Soussi, F. Waagstein, A. Jeppsson, E. Sjoegren-Jansson, A. Lindahl, and E. Omerovic, "In vivo MR imaging of magnetically labeled human embryonic stem cells," Life Sciences **79**, 999-1006 (2006).
43. T. S. Huang, Y. Tzeng, Y. K. Liu, Y. C. Chen, K. R. Walker, R. Guntupalli, and C. Liu, "Immobilization of antibodies and bacterial binding on nanodiamond and carbon nanotubes for biosensor applications," Diamond and Related Materials **13**, 1098-1102 (2004).
44. V. P. Grichko, and O. A. Shenderova, "Nanodiamond: designing the bio-platform," (2006), pp. 529-557.
45. S. C. Hens, G. B. Cunningham, V. Grichko, and O. Shenderova, "Protein capture and detection with bioconjugate nanodiamond probes," (2007), pp. COLL-308.

46. D. A. Heller, S. Baik, T. E. Eurell, and M. S. Strano, "Single-walled carbon nanotube spectroscopy in live cells: Towards long-term labels and optical sensors," Advanced Materials (Weinheim, Germany) **17**, 2793-2799 (2005).
47. P. W. Barone, R. S. Parker, and M. S. Strano, "In Vivo Fluorescence Detection of Glucose Using a Single-Walled Carbon Nanotube Optical Sensor: Design, Fluorophore Properties, Advantages, and Disadvantages," Analytical Chemistry **77**, 7556-7562 (2005).
48. D. A. Heller, E. S. Jeng, T.-K. Yeung, B. M. Martinez, A. E. Moll, J. B. Gastala, and M. S. Strano, "Optical Detection of DNA Conformational Polymorphism on Single-Walled Carbon Nanotubes," Science (Washington, DC, United States) **311**, 508-511 (2006).
49. N. W. S. Kam, M. O'Connell, J. A. Wisdom, and H. Dai, "Carbon nanotubes as multifunctional biological transporters and near-infrared agents for selective cancer cell destruction," Proceedings of the National Academy of Sciences of the United States of America **102**, 11600-11605 (2005).
50. Z. Liu, W. Cai, L. He, N. Nakayama, K. Chen, X. Sun, X. Chen, and H. Dai, "In vivo biodistribution and highly efficient tumour targeting of carbon nanotubes in mice," Nature Nanotechnology **2**, 47-52 (2007).
51. K. Carlson, M. Chidley, K.-B. Sung, M. Descour, A. Gillenwater, M. Follen, and R. Richards-Kortum, "In vivo fiber-optic confocal reflectance microscope with an injection-molded plastic miniature objective lens," Applied optics **44**, 1792-1797. (2005).
52. M. Minsky, "Memoir on inventing the confocal microscope," Scanning **10**, 128-138 (1988).
53. D. Huang, E. A. Swanson, C. P. Lin, J. S. Schuman, W. G. Stinson, W. Chang, M. R. Hee, T. Flotte, K. Gregory, and C. A. Puliafito, "Optical coherence tomography," Science FIELD Full Journal Title:Science **254**, 1178-1181. (1991).
54. J. Eichler, J. Knof, and J. Lenz, "Measurements on the depth of penetration of light (0.35–1.0 µm) in tissue," Radiation and Environmental Biophysics **14**, 239-242 (1977).
55. S. V. Patwardhan, S. R. Bloch, S. Achilefu, and J. P. Culver, "Time-dependent whole-body fluorescence tomography of probe bio-distributions in mice," Optics Express **13**, 2564-2577 (2005).
56. M. Han, X. Gao, J. Z. Su, and S. Nie, "Quantum-dot-tagged microbeads for multiplexed optical coding of biomolecules," Nature Biotechnology **19**, 631-635 (2001).
57. W. C. W. Chan, D. J. Maxwell, X. Gao, R. E. Bailey, M. Han, and S. Nie, "Luminescent quantum dots for multiplexed biological detection and imaging," Current Opinion in Biotechnology **13**, 40-46 (2002).
58. X. Gao, and S. Nie, "Doping Mesoporous Materials with Multicolor Quantum Dots," Journal of Physical Chemistry B **107**, 11575-11578 (2003).
59. X. Gao, and S. Nie, "Semiconductor quantum dots and optically encoded microbeads for gene expression analysis," (2003), pp. 433-447,A438-A439, 432 Plates.
60. X. Gao, L. Yang, J. A. Petros, F. F. Marshall, J. W. Simons, and S. Nie, "In vivo molecular and cellular imaging with quantum dots," Current Opinion in Biotechnology **16**, 63-72 (2005).
61. S. Ohnishi, J. Lomnes Stephen, G. Laurence Rita, A. Gogbashian, G. Mariani, and V. Frangioni John, "Organic alternatives to quantum dots for intraoperative near-infrared fluorescent sentinel lymph node mapping," Mol Imaging FIELD Full Journal Title:Molecular imaging : official journal of the Society for Molecular Imaging **4**, 172-181. (2005).
62. W. W. Yu, E. Chang, R. Drezek, and V. L. Colvin, "Water-soluble quantum dots for biomedical applications," Biochemical and Biophysical Research Communications **348**, 781-786 (2006).
63. S. Schultz, D. R. Smith, J. J. Mock, and D. A. Schultz, "Single-target molecule detection with nonbleaching multicolor optical immunolabels," Proceedings of the National Academy of Sciences of the United States of America **97**, 996-1001 (2000).
64. J. L. Lyon, D. A. Fleming, M. B. Stone, P. Schiffer, and M. E. Williams, "Synthesis of Fe Oxide Core/Au Shell Nanoparticles by Iterative Hydroxylamine Seeding," Nano Letters **4**, 719-723 (2004).
65. R. Shukla, V. Bansal, M. Chaudhary, A. Basu, R. R. Bhonde, and M. Sastry, "Biocompatibility of Gold Nanoparticles and Their Endocytotic Fate Inside the Cellular Compartment: A Microscopic Overview," Langmuir **21**, 10644-10654 (2005).
66. C. Woffendin, U. Ranga, Z.-y. Yang, L. Xu, and G. J. Nabel, "Expression of a protective gene prolongs survival of T cells in human immunodeficiency virus-infected patients," Proceedings of the National Academy of Sciences of the United States of America **93**, 2889-2894 (1996).
67. M. Horisberger, J. Rosset, and H. Bauer, "Colloidal gold granules as markers for cell surface receptors in the scanning electron microscope," Experientia **31**, 1147-1149. (1975).
68. W. D. Geoghegan, and G. A. Ackerman, "Adsorption of horseradish peroxidase, ovomucoid and antiimmunoglobulin to colloidal gold for the indirect detection of concanavalin A, wheat germ agglutinin

and goat antihuman immunoglobulin G on cell surfaces at the electron microscopic level: a new method, theory and application," Journal of Histochemistry and Cytochemistry **25**, 1187-1200 (1977).
69. E. Chang, J. S. Miller, J. Sun, W. W. Yu, V. L. Colvin, R. Drezek, and J. L. West, "Protease-activated quantum dot probes," Biochemical and Biophysical Research Communications **334**, 1317-1321 (2005).
70. J. Yguerabide, and E. E. Yguerabide, "Resonance light scattering particles as ultrasensitive labels for detection of analytes in a wide range of applications," Journal of Cellular Biochemistry, 71-81 (2001).
71. C. Soennichsen, B. M. Reinhard, J. Liphardt, and A. P. Alivisatos, "A molecular ruler based on plasmon coupling of single gold and silver nanoparticles," Nature Biotechnology **23**, 741-745 (2005).
72. B. M. Reinhard, M. Siu, H. Agarwal, A. P. Alivisatos, and J. Liphardt, "Calibration of Dynamic Molecular Rulers Based on Plasmon Coupling between Gold Nanoparticles," Nano Letters **5**, 2246-2252 (2005).
73. R. Elghanian, J. J. Storhoff, R. C. Mucic, R. L. Letsinger, and C. A. Mirkin, "Selective colorimetric detection of polynucleotides based on the distance-dependent optical properties of gold nanoparticles," Science (Washington, D. C.) **277**, 1078-1080 (1997).
74. J. R. Krenn, J. C. Weeber, A. Dereux, E. Bourillot, J. P. Goudonnet, B. Schider, A. Leitner, F. R. Aussenegg, and C. Girard, "Direct observation of localized surface plasmon coupling," Physical Review B: Condensed Matter and Materials Physics **60**, 5029-5033 (1999).
75. E. A. Jares-Erijman, and T. M. Jovin, "Imaging molecular interactions in living cells by FRET microscopy," Current Opinion in Chemical Biology **10**, 409-416 (2006).
76. C. J. Barnes, and R. Kumar, "Biology of the epidermal growth factor receptor family," Cancer Treatment and Research **119**, 1-13 (2004).
77. I. H. El-Sayed, X. Huang, and M. A. El-Sayed, "Selective laser photo-thermal therapy of epithelial carcinoma using anti-EGFR antibody conjugated gold nanoparticles," Cancer Letters (Amsterdam, Netherlands) **239**, 129-135 (2006).
78. X. Huang, P. K. Jain, I. H. El-Sayed, and M. A. El-Saved, "Determination of the minimum temperature required for selective photothermal destruction of cancer cells with the use of immunotargeted gold nanoparticles," Photochemistry and Photobiology **82**, 412-417 (2006).
79. J. C. Y. Kah, C. J. R. Sheppard, C. G. L. Lee, and M. C. Olivo, "Application of antibody-conjugated gold nanoparticles for optical molecular imaging of epithelial carcinoma cells," Proceedings of SPIE-The International Society for Optical Engineering **6095**, 609503/609501-609503/609506 (2006).
80. M. Rahman, M. Abd-El-Barr, V. Mack, T. Tkaczyk, K. Sokolov, R. Richards-Kortum, and M. Descour, "Optical imaging of cervical pre-cancers with structured illumination: an integrated approach," Gynecologic oncology **99**, S112-115. (2005).
81. I. H. El-Sayed, X. Huang, and M. A. El-Sayed, "Surface plasmon resonance scattering and absorption of anti-EGFR antibody conjugated gold nanoparticles in cancer diagnostics: Applications in oral cancer," Nano Letters **5**, 829-834 (2005).
82. D. L. Nida, M. S. Rahman, K. D. Carlson, R. Richards-Kortum, and M. Follen, "Fluorescent nanocrystals for use in early cervical cancer detection," Gynecologic Oncology **99**, S89-S94 (2005).
83. D. S. Lidke, P. Nagy, R. Heintzmann, D. J. Arndt-Jovin, J. N. Post, H. E. Grecco, E. A. Jares-Erijman, and T. M. Jovin, "Quantum dot ligands provide new insights into erbB/HER receptor-mediated signal transduction," Nature Biotechnology **22**, 198-203 (2004).
84. A. Kriete, E. Papazoglou, B. Edrissi, H. Pais, and K. Pourrezaei, "Automated quantification of quantum-dot-labelled epidermal growth factor receptor internalization via multiscale image segmentation," J Microsc FIELD Full Journal Title:Journal of microscopy **222**, 22-27. (2006).
85. J. Wang, P. T. Vernier, Y. Sun, M. A. Gundersen, and L. Marcu, "A fluorescence microscopy study of quantum dots as fluorescent probes for brain tumor diagnosis," Proceedings of SPIE-The International Society for Optical Engineering **5703**, 127-134 (2005).
86. V. S. Contran, V. Kumar, and T. Collins, *Pathologic basis of disease.* (Saunders, Philadelphia, PA, 1999).
87. "National Cervical Cancer Coalition," (2007), http://www.nccc-online.org/, Accessed March 19th, 2007.
88. R. Kooijman, "Regulation of apoptosis by insulin-like growth factor (IGF)-I," Cytokine & Growth Factor Reviews **17**, 305-323 (2006).
89. A. Sanchez-Capelo, "Dual role for TGF-b1 in apoptosis," Cytokine & Growth Factor Reviews **16**, 15-34 (2005).
90. M. J. E. M. F. Mabruk, and C. O'Flatharta, "Telomerase: is it the future diagnostic and prognostic tool in human cancer?," Expert Review of Molecular Diagnostics **5**, 907-916 (2005).
91. P. Carmeliet, "VEGF gene therapy: stimulating angiogenesis or angioma-genesis?," in *Nature medicine*(United States, 2000), pp. 1102-1103.

92. T. Turpeenniemi-Hujanen, "Gelatinases (MMP-2 and -9) and their natural inhibitors as prognostic indicators in solid cancers," Biochimie **87**, 287-297 (2005).
93. J. E. Sprague, W. P. Li, K. Liang, S. Achilefu, and C. J. Anderson, "In vitro and in vivo investigation of matrix metalloproteinase expression in metastatic tumor models," Nuclear Medicine and Biology **33**, 227-237 (2006).
94. C. J. Malemud, "Matrix metalloproteinases (MMPs) in health and disease: an overview," Frontiers in Bioscience **11**, 1696-1701 (2006).
95. C. J. Gruss, K. Satyamoorthy, C. Berking, J. Lininger, M. Nesbit, H. Schaider, Z.-J. Liu, M. Oka, M.-Y. Hsu, T. Shirakawa, G. Li, T. Bogenrieder, P. Carmeliet, W. S. El-Deiry, S. L. Eck, J. S. Rao, A. H. Baker, J. T. Bennet, T. M. Crombleholme, O. Velazquez, J. Karmacharya, D. J. Margolis, J. M. Wilson, M. Detmar, M. Skobe, P. D. Robbins, C. Buck, and M. Herlyn, "Stroma formation and angiogenesis by overexpression of growth factors, cytokines, and proteolytic enzymes in human skin grafted to SCID mice," Journal of Investigative Dermatology **120**, 683-692 (2003).
96. J. Schlessinger, A. B. Schreiber, A. Levi, I. Lax, T. Libermann, and Y. Yarden, "Regulation of cell proliferation by epidermal growth factor," Critical Reviews in Biochemistry **14**, 93-111 (1983).
97. K. Miller, J. Beardmore, H. Kanety, J. Schlessinger, and C. R. Hopkins, "Localization of the epidermal growth factor (EGF) receptor within the endosome of EGF-stimulated epidermoid carcinoma (A431) cells," Journal of Cell Biology **102**, 500-509 (1986).
98. H. Riedel, T. J. Dull, A. M. Honegger, J. Schlessinger, and A. Ullrich, "Cytoplasmic domains determine signal specificity, cellular routing characteristics and influence ligand binding of epidermal growth factor and insulin receptors," EMBO Journal **8**, 2943-2954 (1989).
99. M. Zhou, S. Felder, M. Rubinstein, D. R. Hurwitz, A. Ullrich, I. Lax, and J. Schlessinger, "Real-time measurements of kinetics of EGF binding to soluble EGF receptor monomers and dimers support the dimerization model for receptor activation," Biochemistry **32**, 8193-8198 (1993).
100. R. Perez-Soler, N. J. Donato, D. M. Shin, M. G. Rosenblum, H. Z. Zhang, C. Tornos, H. Brewer, J. C. Chan, J. S. Lee, and W. K. Hong, "Tumor epidermal growth factor receptor studies in patients with non-small-cell lung cancer or head and neck cancer treated with monoclonal antibody RG 83852," Journal of clinical oncology : official journal of the American Society of Clinical Oncology **12**, 730-739. (1994).
101. W. S. Katz, G. M. Lesa, D. Yannoukakos, T. R. Clandinin, J. Schlessinger, and P. W. Sternberg, "A point mutation in the extracellular domain activates LET-23, the Caenorhabditis elegans epidermal growth factor receptor homolog," Molecular and Cellular Biology **16**, 529-537 (1996).
102. I. V. Boiko, M. F. Mitchell, W. Hu, D. K. Pandey, P. Mathevet, A. Malpica, and W. N. Hittelman, "Epidermal growth factor receptor expression in cervical intraepithelial neoplasia and its modulation during an a-difluoromethylornithine chemoprevention trial," Clinical Cancer Research **4**, 1383-1391 (1998).
103. R. Todd, and D. T. W. Wong, "Epidermal growth factor receptor (EGFR) biology and human oral cancer," Histology and Histopathology **14**, 491-500 (1999).
104. Z. Yang, C. J. Barnes, and R. Kumar, "Human Epidermal Growth Factor Receptor 2 Status Modulates Subcellular Localization of and Interaction with Estrogen Receptor a in Breast Cancer Cells," Clinical Cancer Research **10**, 3621-3628 (2004).
105. P. Klein, D. Mattoon, M. A. Lemmon, and J. Schlessinger, "A structure-based model for ligand binding and dimerization of EGF receptors," Proceedings of the National Academy of Sciences of the United States of America **101**, 929-934 (2004).
106. D. Mattoon, P. Klein, M. A. Lemmon, I. Lax, and J. Schlessinger, "The tethered configuration of the EGF receptor extracellular domain exerts only a limited control of receptor function," Proceedings of the National Academy of Sciences of the United States of America **101**, 923-928 (2004).
107. A. Zaczek, B. Brandt, and K. P. Bielawski, "The diverse signaling network of EGFR, HER2, HER3 and HER4 tyrosine kinase receptors and the consequences for therapeutic approaches," Histology and Histopathology **20**, 1005-1015 (2005).
108. C. J. Barnes, and R. Kumar, "Epidermal growth factor receptor family tyrosine kinases as signal integrators and therapeutic targets," Cancer and Metastasis Reviews **22**, 301-307 (2003).
109. M. A. Lemmon, Z. Bu, J. E. Ladbury, M. Zhou, D. Pinchasi, I. Lax, D. M. Engelman, and J. Schlessinger, "Two EGF molecules contribute additively to stabilization of the EGFR dimer," EMBO Journal **16**, 281-294 (1997).
110. T. Spivak-Kroizman, D. Rotin, D. Pinchasi, A. Ullrich, J. Schlessinger, and I. Lax, "Heterodimerization of c-erbB2 with different epidermal growth factor receptor mutants elicits stimulatory or inhibitory responses," Journal of Biological Chemistry **267**, 8056-8063 (1992).

111. N. Normanno, C. Bianco, L. Strizzi, M. Mancino, M. R. Maiello, A. De Luca, F. Caponigro, and D. S. Salomon, "The ErbB receptors and their ligands in cancer: An overview," Current Drug Targets **6**, 243-257 (2005).
112. C. Barnes, J., R. Bagheri-Yarmand, M. Mandal, Z. Yang, L. Clayman Gary, K. Hong Waun, and R. Kumar, "Suppression of epidermal growth factor receptor, mitogen-activated protein kinase, and Pak1 pathways and invasiveness of human cutaneous squamous cancer cells by the tyrosine kinase inhibitor ZD1839 (Iressa)," Molecular cancer therapeutics **2**, 345-351. (2003).
113. M. Sibilia, A. Fleischmann, A. Behrens, L. Stingl, J. Carroll, F. M. Watt, J. Schlessinger, and E. F. Wagner, "The EGF receptor provides an essential survival signal for SOS-dependent skin tumor development," Cell (Cambridge, Massachusetts) **102**, 211-220 (2000).
114. S. Tsuchiya, K. Ogura, H. Hatanaka, K. Nagata, H. Terasawa, V. Mandivan, J. Schlessinger, S. Aimoto, H. Ohta, and F. Inagaki, "Solution structure of the SH2 domain of Grb2/Ash complexed with EGF receptor-derived phosphotyrosine-containing peptide," Journal of Biochemistry (Tokyo) **125**, 1151-1159 (1999).
115. G. A. Rodrigues, M. Falasca, Z. Zhang, S. H. Ong, and J. Schlessinger, "A novel positive feedback loop mediated by the docking protein Gab1 and phosphatidylinositol 3-kinase in epidermal growth factor receptor signaling," Molecular and Cellular Biology **20**, 1448-1459 (2000).
116. J. Andreev, M. L. Galisteo, O. Kranenburg, S. K. Logan, E. S. Chiu, M. Okigaki, L. A. Cary, W. H. Moolenaar, and J. Schlessinger, "Src and Pyk2 mediate G-protein-coupled receptor activation of epidermal growth factor receptor (EGFR) but are not required for coupling to the mitogen-activated protein (MAP) kinase signaling cascade," Journal of Biological Chemistry **276**, 20130-20135 (2001).
117. R. Mattoon Dawn, B. Lamothe, I. Lax, and J. Schlessinger, "The docking protein Gab1 is the primary mediator of EGF-stimulated activation of the PI-3K/Akt cell survival pathway," BMC biology [electronic resource] **2**, 24. (2004).
118. M. D. Hollenberg, and P. Cuatrecasas, "Epidermal growth factor. Receptors in human fibroblasts and modulation of action by cholera toxin," Proceedings of the National Academy of Sciences of the United States of America **70**, 2964-2968 (1973).
119. M. M. Wrann, and C. F. Fox, "Identification of epidermal growth factor receptors in a hyperproducing human epidermoid carcinoma cell line," Journal of Biological Chemistry **254**, 8083-8086 (1979).
120. P. S. Linsley, "Structural studies of the membrane receptors for epidermal growth factor," (1980), p. 199 pp.
121. J. Schlessinger, Y. Shechter, P. Cuatrecasas, M. C. Willingham, and I. Pastan, "Quantitative determination of the lateral diffusion coefficients of the hormone-receptor complexes of insulin and epidermal growth factor on the plasma membrane of cultured fibroblasts," Proceedings of the National Academy of Sciences of the United States of America **75**, 5353-5357 (1978).
122. J. Schlessinger, "Lateral and rotational diffusion of EGF-receptor complex: relationship to receptor-mediated endocytosis," Biopolymers **22**, 347-353 (1983).
123. B. Westermark, "Local starvation for epidermal growth factor cannot explain density-dependent inhibition of normal human glial cells," Proceedings of the National Academy of Sciences of the United States of America **74**, 1619-1621 (1977).
124. A. M. Jetten, "Retinoids specifically enhance the number of epidermal growth factor receptors," Nature (London, United Kingdom) **284**, 626-629 (1980).
125. M. Wrann, C. F. Fox, and R. Ross, "Modulation of epidermal growth factor receptors on 3T3 cells by platelet-derived growth factor," Science (Washington, DC, United States) **210**, 1363-1365 (1980).
126. H. T. Haigler, M. C. Willingham, and I. Pastan, "Inhibitors of [125I]-epidermal growth factor internalization," Biochemical and Biophysical Research Communications **94**, 630-637 (1980).
127. J. Schlessinger, "Receptor aggregation as a mechanism for transmembrane signalling: models for hormone action," Developments in Cell Biology (Amsterdam) **4**, 89-118 (1979).
128. Y. Schechter, L. Hernaez, J. Schlessinger, and P. Cuatrecasas, "Local aggregation of hormone-receptor complexes is required for activation by epidermal growth factor," Nature (London, United Kingdom) **278**, 835-838 (1979).
129. A. B. Schreiber, T. A. Libermann, I. Lax, Y. Yarden, and J. Schlessinger, "Biological role of epidermal growth factor-receptor clustering. Investigation with monoclonal anti-receptor antibodies," Journal of Biological Chemistry **258**, 846-853 (1983).
130. J. Schlessinger, A. B. Schreiber, T. A. Libermann, I. Lax, A. Avivi, and Y. Yarden, "Polypeptide-hormone-induced receptor clustering and internalization," Cell Membranes (New York) **1**, 117-149 (1983).

131. R. Zidovetzki, Y. Yarden, J. Schlessinger, and T. M. Jovin, "Microaggregation of hormone-occupied epidermal growth factor receptors on plasma membrane preparations," EMBO Journal **5**, 247-250 (1986).
132. Y. Yarden, and J. Schlessinger, "Epidermal growth factor induces rapid, reversible aggregation of the purified epidermal growth factor receptor," Biochemistry **26**, 1443-1451 (1987).
133. C. Cochet, O. Kashles, E. M. Chambaz, I. Borrello, C. R. King, and J. Schlessinger, "Demonstration of epidermal growth factor-induced receptor dimerization in living cells using a chemical covalent cross-linking agent," Journal of Biological Chemistry **263**, 3290-3295 (1988).
134. A. Vieira, C. Lamaze, and S. L. Schmid, "Control of EGF receptor signaling by clathrin-mediated endocytosis," Science (Washington, D. C.) **274**, 2086-2089 (1996).
135. R. E. Carter, and A. Sorkin, "Endocytosis of functional epidermal growth factor receptor-green fluorescent protein chimera," Journal of Biological Chemistry **273**, 35000-35007 (1998).
136. S. Martinez-Arca, J. Bech-Serra Joan, M. Hurtado-Kuttner, A. Borroto, and J. Arribas, "Recycling of cell surface pro-transforming growth factor-{alpha} regulates epidermal growth factor receptor activation," The Journal of biological chemistry **280**, 36970-36977. (2005).
137. P. Burke, K. Schooler, and H. S. Wiley, "Regulation of epidermal growth factor receptor signaling by endocytosis and intracellular trafficking," Molecular Biology of the Cell **12**, 1897-1910 (2001).
138. M. P. Oksvold, E. Skarpen, L. Wierod, R. E. Paulsen, and H. S. Huitfeldt, "Re-localization of activated EGF receptor and its signal transducers to multivesicular compartments downstream of early endosomes in response to EGF," European Journal of Cell Biology **80**, 285-294 (2001).
139. B. P. Ceresa, "Regulation of EGFR endocytic trafficking by rab proteins," Histology and Histopathology **21**, 987-993 (2006).
140. E. B. Leof, "Growth factor receptor signalling: location, location, location," Trends in Cell Biology **10**, 343-348 (2000).
141. F. Aniento, N. Emans, G. Griffiths, and J. Gruenberg, "Cytoplasmic dynein-dependent vesicular transport from early to late endosomes," Journal of Cell Biology **123**, 1373-1387 (1993).
142. D. D. Tran, H. R. Russell, S. L. Sutor, J. van Deursen, and R. J. Bram, "CAML is required for efficient EGF receptor recycling," Developmental Cell **5**, 245-256 (2003).
143. M. L. Martin-Fernandez, D. T. Clarke, M. J. Tobin, and G. R. Jones, "Real-time studies of the interactions between epidermal growth factor and its receptor during endocytic trafficking," Cellular and Molecular Biology (Paris) **46**, 1103-1112 (2000).
144. K. Sokolov, K.-B. Sung, T. Collier, A. Clark, D. Arifler, A. Lacy, M. Descour, and R. Richards-Kortum, "Endoscopic microscopy," Disease markers **18**, 269-291. (2002).
145. M. Rajadhyaksha, M. Grossman, D. Esterowitz, R. H. Webb, and R. R. Anderson, "In vivo confocal scanning laser microscopy of human skin: melanin provides strong contrast," J Invest Dermatol FIELD Full Journal Title:The Journal of investigative dermatology **104**, 946-952. (1995).
146. T. Collier, D. Arifler, A. Malpica, M. Follen, and R. Richards-kortum, "Determination of epithelial tissue scattering coefficient using confocal microscopy," IEEE Journal of Selected Topics in Quantum Electronics **9**, 307-313 (2003).
147. F. Zuluaga Andres, M. Follen, I. Boiko, A. Malpica, and R. Richards-Kortum, "Optical coherence tomography: a pilot study of a new imaging technique for noninvasive examination of cervical tissue," American journal of obstetrics and gynecology **193**, 83-88. (2005).
148. R. Schwarz, A., D. Arifler, K. Chang Sung, I. Pavlova, A. Hussain Insiya, V. Mack, B. Knight, R. Richards-Kortum, and M. Gillenwater Ann, "Ball lens coupled fiber-optic probe for depth-resolved spectroscopy of epithelial tissue," Optics letters **30**, 1159-1161. (2005).
149. T. Collier, A. Lacy, R. Richards-Kortum, A. Malpica, and M. Follen, "Near real-time confocal microscopy of amelanotic tissue: detection of dysplasia in ex vivo cervical tissue," Academic radiology **9**, 504-512. (2002).
150. "Evaluation of Cervical Cytology," (Agency for Health Care Policy and Research, 1999).
151. W. Luo, T. Nguyen Freddy, M. Zysk Adam, S. Ralston Tyler, J. Brockenbrough, L. Marks Daniel, L. Oldenburg Amy, and A. Boppart Stephen, "Optical biopsy of lymph node morphology using optical coherence tomography," Technology in cancer research & treatment **4**, 539-548. (2005).
152. L. T. Perelman, V. Backman, M. Wallace, G. Zonios, R. Manoharan, A. Nusrat, S. Shields, M. Seiler, C. Lima, T. Hamano, I. Itzkan, J. Van Dam, J. M. Crawford, and M. S. Feld, "Observation of Periodic Fine Structure in Reflectance from Biological Tissue: A New Technique for Measuring Nuclear Size Distribution," Physical Review Letters **80**, 627-630 (1998).

153. A. Gillenwater, R. Jacob, R. Ganeshappa, B. Kemp, A. K. El-Naggar, J. L. Palmer, G. Clayman, M. F. Mitchell, and R. Richards-Kortum, "Noninvasive diagnosis of oral neoplasia based on fluorescence spectroscopy and native tissue autofluorescence," Archives of otolaryngology--head & neck surgery **124**, 1251-1258. (1998).
154. C. K. Brookner, M. Follen, I. Boiko, J. Galvan, S. Thomsen, A. Malpica, S. Suzuki, R. Lotan, and R. Richards-Kortum, "Autofluorescence patterns in short-term cultures of normal cervical tissue," Photochemistry and Photobiology **71**, 730-736 (2000).
155. D. L. Heintzelman, R. Lotan, and R. R. Richards-Kortum, "Characterization of the autofluorescence of polymorphonuclear leukocytes, mononuclear leukocytes and cervical epithelial cancer cells for improved spectroscopic discrimination of inflammation from dysplasia," Photochemistry and Photobiology **71**, 327-332 (2000).
156. R. Drezek, C. Brookner, I. Pavlova, I. Boiko, A. Malpica, R. Lotan, M. Follen, and R. Richards-Kortum, "Autofluorescence microscopy of fresh cervical-tissue sections reveals alterations in tissue biochemistry with dysplasia," Photochemistry and Photobiology **73**, 636-641 (2001).
157. L. Coghlan, U. Utzinger, R. Richards-Kortum, C. Brookner, A. Zuluaga, I. Gimenez-Conti, and M. Follen, "Fluorescence spectroscopy of epithelial tissue throughout the dysplasia-carcinoma sequence in an animal model: spectroscopic changes precede morphologic changes," Lasers in surgery and medicine **29**, 1-10. (2001).
158. E. M. Gill, A. Malpica, R. E. Alford, A. R. Nath, M. Follen, R. R. Richards-Kortum, and N. Ramanujam, "Relationship between collagen autofluorescence of the human cervix and menopausal status," Photochemistry and Photobiology **77**, 653-658 (2003).
159. H. C. van de Hulst, *Light Scattering By Small Particles* (Dover, Mineola, NY, 1981).
160. A. F. Zuluaga, U. Utzinger, A. Durkin, H. Fuchs, A. Gillenwater, R. Jacob, B. Kemp, J. Fan, and R. Richards-Kortum, "Fluorescence excitation emission matrixes of human tissue: a system for in vivo measurement and method of data analysis," Applied Spectroscopy **53**, 302-311 (1999).
161. R. Richards-Kortum, R. Drezek, K. Sokolov, I. Pavlova, and M. Follen, "Survey of endogenous biological fluorophores," (2003), pp. 237-264.
162. M.-A. Mycek, and B. Pogue, *Handbook of Biomedical Fluorescence* (Marcel Dekker, Inc., New York, NY, 2003).
163. K. Konig, "Multiphoton microscopy in life sciences," Journal of Microscopy (Oxford) **200**, 83-104 (2000).
164. I. Pavlova, K. Sokolov, R. Drezek, A. Malpica, M. Follen, and R. Richards-Kortum, "Microanatomical and biochemical origins of normal and precancerous cervical autofluorescence using laser-scanning fluorescence confocal microscopy," Photochemistry and Photobiology **77**, 550-555 (2003).
165. A. Mahadevan-Jansen, M. F. Mitchell, N. Ramanujam, A. Malpica, S. Thomsen, U. Utzinger, and R. Richards-Kortum, "Near-infrared Raman spectroscopy for in vitro detection of cervical precancers," Photochemistry and Photobiology **68**, 123-132 (1998).
166. U. Utzinger, D. L. Heintzelman, A. Mahadevan-Jansen, A. Malpica, M. Follen, and R. Richards-Kortum, "Near-infrared Raman spectroscopy for in vivo detection of cervical precancers," Applied Spectroscopy **55**, 955-959 (2001).
167. B. N. G. Giepmans, S. R. Adams, M. H. Ellisman, and R. Y. Tsien, "The Fluorescent Toolbox for Assessing Protein Location and Function," Science (Washington, DC, United States) **312**, 217-224 (2006).
168. D. J. Bornhop, C. H. Contag, K. Licha, and C. J. Murphy, "Advance in contrast agents, reporters, and detection," Journal of biomedical optics **6**, 106-110. (2001).
169. J. Malicka, I. Gryczynski, J. Fang, and R. Lakowicz Joseph, "Fluorescence spectral properties of cyanine dye-labeled DNA oligomers on surfaces coated with silver particles," Analytical biochemistry **317**, 136-146. (2003).
170. V. Ntziachristos, C.-H. Tung, C. Bremer, and R. Weissleder, "Fluorescence molecular tomography resolves protease activity in vivo," Nature Medicine (New York, NY, United States) **8**, 757-761 (2002).
171. B. Bednar, G.-J. Zhang, D. L. Williams, Jr., R. Hargreaves, and C. Sur, "Optical molecular imaging in drug discovery and clinical development," Expert Opinion on Drug Discovery **2**, 65-85 (2007).
172. A. Keppler, C. Arrivoli, L. Sironi, and J. Ellenberg, "Fluorophores for live cell imaging of AGT fusion proteins across the visible spectrum," BioTechniques **41**, 167-170,172,174-175 (2006).
173. T. Y. Ohulchanskyy, H. E. Pudavar, S. M. Yarmoluk, V. M. Yashchuk, E. J. Bergey, and P. N. Prasad, "A monomethine cyanine dye cyan 40 for two-photon-excited fluorescence detection of nucleic acids and their visualization in live cells," Photochemistry and Photobiology **77**, 138-145 (2003).

174. D. M. Plank, and M. A. Sussman, "Impaired intracellular Ca2+ dynamics in live cardiomyocytes revealed by rapid line scan confocal microscopy," Microscopy and Microanalysis **11**, 235-243 (2005).
175. A. Toutchkine, V. Kraynov, and K. Hahn, "Solvent-sensitive dyes to report protein conformational changes in living cells," J Am Chem Soc FIELD Full Journal Title:Journal of the American Chemical Society **125**, 4132-4145. (2003).
176. E. R. Hsu, E. V. Anslyn, S. Dharmawardhane, R. Alizadeh-Naderi, J. S. Aaron, K. V. Sokolov, A. K. El-Naggar, A. M. Gillenwater, and R. R. Richards-Kortum, "A far-red fluorescent contrast agent to image epidermal growth factor receptor expression," Photochemistry and Photobiology **79**, 272-279 (2004).
177. Z. Zhang, and S. Achilefu, "Design, synthesis and evaluation of near-infrared fluorescent pH indicators in a physiologically relevant range," Chemical Communications (Cambridge, United Kingdom), 5887-5889 (2005).
178. G. G. Blasdel, and G. Salama, "Voltage-sensitive dyes reveal a modular organization in monkey striate cortex," Nature **321**, 579-585 (1986).
179. M. J. O'Donovan, S. Ho, G. Sholomenko, and W. Yee, "Real-time imaging of neurons retrogradely and anterogradely labelled with calcium-sensitive dyes.," J Neurosci Methods. **46**, 91-106 (1993).
180. X. Gao, Y. Cui, R. M. Levenson, L. W. K. Chung, and S. Nie, "In vivo cancer targeting and imaging with semiconductor quantum dots," Nature Biotechnology **22**, 969-976 (2004).
181. X. Michalet, F. F. Pinaud, L. A. Bentolila, J. M. Tsay, S. Doose, J. J. Li, G. Sundaresan, A. M. Wu, S. S. Gambhir, and S. Weiss, "Quantum Dots for Live Cells, in Vivo Imaging, and Diagnostics," Science (Washington, DC, United States) **307**, 538-544 (2005).
182. A. P. Alivisatos, W. Gu, and C. Larabell, "Quantum Dots as Cellular Probes," in *Annual Review of Biomedical Engineering*(2005), pp. 55-76.
183. M. A. Reed, J. N. Randall, R. J. Aggarwal, R. J. Matyi, T. M. Moore, and A. E. Wetsel, "Observation of Discrete electronic States in a Zero-Dimensional Semiconductor Nanostructure," Phyical Review Letters **60**, 535-537 (1988).
184. D. J. Arndt-Jovin, M. A. Lopez-Quintela, D. S. Lidke, M. J. Rodriguez, F. Martinez Santos, K. A. Lidke, G. M. Hagen, and T. M. Jovin, "In vivo cell imaging with semiconductor quantum dots and noble metal nanodots," Proceedings of SPIE-The International Society for Optical Engineering **6096**, 60960P/60961-60960P/60910 (2006).
185. H. E. Grecco, K. A. Lidke, R. Heintzmann, D. S. Lidke, C. Spagnuolo, O. E. Martinez, E. A. Jares-Erijman, and T. M. Jovin, "Ensemble and single particle photophysical properties (two-photon excitation, anisotropy, FRET, lifetime, spectral conversion) of commercial quantum dots in solution and in live cells," Microscopy Research and Technique **65**, 169-179 (2004).
186. C.-H. Tung, U. Mahmood, S. Bredow, and R. Weissleder, "In vivo imaging of proteolytic enzyme activity using a novel molecular reporter," Cancer Research **60**, 4953-4958 (2000).
187. J. H. Kim, D. Morikis, and M. Ozkan, "Adaptation of inorganic quantum dots for stable molecular beacons," Sensors and Actuators, B: Chemical **B102**, 315-319 (2004).
188. M. Faraday, "Experimental Relations of Gold (and Other Metals) to Light," Philosophical Transactions of the Royal Society of London **147**, 145-181 (1857).
189. J. Yguerabide, and E. E. Yguerabide, "Light-scattering submicroscopic particles as highly fluorescent analogs and their use as tracer labels in clinical and biological applications. II. Experimental characterization," Analytical Biochemistry **262**, 157-176 (1998).
190. C. L. Nehl, N. K. Grady, G. P. Goodrich, F. Tam, N. J. Halas, and J. H. Hafner, "Scattering Spectra of Single Gold Nanoshells," Nano Letters **4**, 2355-2359 (2004).
191. W. Rechberger, A. Hohenau, A. Leitner, J. R. Krenn, B. Lamprecht, and F. R. Aussenegg, "Optical properties of two interacting gold nanoparticles," Optics Communications **220**, 137-141 (2003).
192. M. Salerno, J. R. Krenn, A. Hohenau, H. Ditlbacher, G. Schider, A. Leitner, and F. R. Aussenegg, "The optical near-field of gold nanoparticle chains," Optics Communications **248**, 543-549 (2005).
193. L. Stepanov Andrey, R. Krenn Joachim, H. Ditlbacher, A. Hohenau, A. Drezet, B. Steinberger, A. Leitner, and R. Aussenegg Franz, "Quantitative analysis of surface plasmon interaction with silver nanoparticles," Optics letters **30**, 1524-1526. (2005).
194. K. Travis, "Optical scattering from nanoparticle aggregates," in *Physics*(University of Texas at Austin, Austin, 2004).
195. K. Sokolov, M. Follen, J. Aaron, I. Pavlova, A. Malpica, R. Lotan, and R. Richards-Kortum, "Real-time vital optical imaging of precancer using anti-epidermal growth factor receptor antibodies conjugated to gold nanoparticles," Cancer Research **63**, 1999-2004 (2003).

196. J. R. Krenn, A. Dereux, J. C. Weeber, E. Bourillot, Y. Lacroute, J. P. Goudonnet, G. Schider, W. Gotschy, A. Leitner, F. R. Aussenegg, and C. Girard, "Squeezing the Optical Near-Field Zone by Plasmon Coupling of Metallic Nanoparticles," Physical Review Letters **82**, 2590-2593 (1999).
197. U. Kreibig, and M. Volmer, *Optical Properties of Metal Clusters* (Springer, Berlin, Germany, 1995).
198. B. T. Draine, and P. J. Flatau, "Discrete-dipole approximation for scattering calculations," Journal of the Optical Society of America A: Optics, Image Science, and Vision **11**, 1491- (1994).
199. M. I. Mishchenko, and L. D. Travis, "T-matrix computations of light scattering by large spheroidal particles," Optics Communications **109**, 16-21 (1994).
200. M. Rosenbluh, I. Edrei, M. Kaveh, and I. Freund, "Precision determination of the line shape for coherently backscattered light from disordered solids: Comparison of vector and scalar theories," Physical Review A: Atomic, Molecular, and Optical Physics **35**, 4458-4460 (1987).
201. G. Frens, "Controlled nucleation for the regulation of the particle size in monodisperse gold suspensions," Nature (London), Physical Science **241**, 20-22 (1973).
202. T. K. Sau, A. Pal, N. R. Jana, Z. L. Wang, and T. Pal, "Size controlled synthesis of gold nanoparticles using photochemically prepared seed particles," Journal of Nanoparticle Research **3**, 257-261 (2001).
203. R. G. DiScipio, " Preparation of Colloidal Gold Particles of Various Sizes Using Sodium Borohydride and Sodium Cyanoborohydride," Analytical Biochemistry **236**, 3 (1996).
204. Y. Nagata, Y. Mizukoshi, K. Okitsu, and Y. Maeda, "Sonochemical formation of gold particles in aqueous solution," Radiat Res FIELD Full Journal Title:Radiation research **146**, 333-338. (1996).
205. S. Huang, H. Ma, X. Zhang, F. Yong, X. Feng, W. Pan, X. Wang, Y. Wang, and S. Chen, "Electrochemical Synthesis of Gold Nanocrystals and Their 1D and 2D Organization," Journal of Physical Chemistry B **109**, 19823-19830 (2005).
206. M. K. Corbierre, J. Beerens, and R. B. Lennox, "Gold Nanoparticles Generated by Electron Beam Lithography of Gold(I)-Thiolate Thin Films," Chemistry of Materials **17**, 5774-5779 (2005).
207. J. Perez-Juste, I. Pastoriza-Santos, L. M. Liz-Marzan, and P. Mulvaney, "Gold nanorods: Synthesis, characterization and applicatons," Coord. Chem. Rev **249** (2005).
208. W. Frey, C. K. Woods, and A. Chilkoti, "Ultraflat nanosphere lithography: a new method to fabricate flat nanostructures," Advanced Materials (Weinheim, Germany) **12**, 1515-1519 (2000).
209. L. M. Liz-Marzan, M. Giersig, and P. Mulvaney, "Synthesis of Nanosized Gold-Silica Core-Shell Particles," Langmuir **12**, 4329-4335 (1996).
210. R. D. Averitt, D. Sarkar, and N. J. Halas, "Plasmon resonance shifts of Au-coated Au2S nanoshells: insight into multicomponent nanoparticle growth," Physical Review Letters **78**, 4217-4220 (1997).
211. J. Chen, F. Saeki, B. J. Wiley, H. Cang, M. J. Cobb, Z.-Y. Li, L. Au, H. Zhang, M. B. Kimmey, X. Li, and Y. Xia, "Gold Nanocages: Bioconjugation and Their Potential Use as Optical Imaging Contrast Agents," Nano Letters **5**, 5 (2005).
212. J. L. Rodríguez-López, J. M. Montejano-Carrizales, and M. José-Yacamán, "Low Dimensional Non-Crystallographic Metallic Nanostructures:. HRTEM Simulation, Models and Experimental Results," Modern Physics Letters B **20** (2006).
213. M. Horisberger, J. Rosset, and H. Bauer, "Localization of mannan at the surface of yeast protoplasts by scanning electron microscopy," Archives of Microbiology **109**, 9-14 (1976).
214. M. Horisberger, and J. Rosset, "Colloidal gold, a useful marker for transmission and scanning electron microscopy," Journal of Histochemistry and Cytochemistry **25**, 295-305 (1977).
215. M. Horisberger, and M. Vonlanthen, "Multiple marking of cell surface receptors by gold granules: simultaneous localization of three lectin receptors on human erythrocytes," Journal of microscopy **115**, 97-102. (1979).
216. C. D. Bain, and G. M. Whitesides, "Modeling organic surfaces with self-assembled monolayers," Angewandte Chemie **101**, 522-528 (1989).
217. L. Pasquato, P. Pengo, and P. Scrimin, "Functional gold nanoparticles for recognition and catalysis," Journal of Materials Chemistry **14**, 3481-3487 (2004).
218. T. Wilson, and B. R. Masters, "Confocal Microscopy," Applied Optics **33**, 565 (1994).
219. J. B. Pawley, and R. M. Barry, "Handbook of Biological Confocal Microscopy, Second Edition," (SPIE, 1996), pp. 2765-2766.
220. T. N. J. R. Z. R. R. R. W. H. R. G. Roger A. Schultz, "Hyperspectral imaging: A novel approach for microscopic analysis," **43**, 239-247 (2001).

221. E. Schrock, S. du Manoir, T. Veldman, B. Schoell, J. Wienberg, M. A. Ferguson-Smith, Y. Ning, D. H. Ledbetter, I. Bar-Am, D. Soenksen, Y. Garini, and T. Ried, "Multicolor Spectral Karyotyping of Human Chromosomes," (1996), pp. 494-497.
222. J. M. Lerner, "Imaging Spectrometer Fundamentals for Researchers in the Biosciences—A Tutorial," Cytometry Part A **69A**, 712-734 (2006).
223. M. B. Sinclair, D. M. Haaland, J. A. Timlin, and H. D. T. Jones, "Hyperspectral confocal microscope," Applied Optics **45**, 6283-6291 (2006).
224. M. Horisberger, "Colloidal gold: a cytochemical marker for light and fluorescent microscopy and for transmission and scanning electron microscopy," Scanning Electron Microscopy, 9-31 (1981).
225. S. Nie, and S. R. Emory, "Probing Single Molecules and Single Nanoparticles by Surface-Enhanced Raman Scattering," (1997), pp. 1102-1106.
226. J. Yguerabide, and E. E. Yguerabide, "Light-scattering submicroscopic particles as highly fluorescent analogs and their use as tracer labels in clinical and biological applications. I. Theory," Analytical Biochemistry **262**, 137-156 (1998).
227. C. A. Mirkin, R. L. Letsinger, R. C. Mucic, and J. J. Storhoff, "A DNA-based method for rationally assembling nanoparticles into macroscopic materials," Nature (London) **382**, 607-609 (1996).
228. G. Viswanadham, R. Elghanian, C. A. Mirkin, and R. L. Letsinger, "Colorimetric detection of PCR amplicons using gold nanoparticle oligonucleotide probes," (1999), pp. ORGN-370.
229. C. A. Mirkin, R. L. Letsinger, J. J. Storhoff, R. Elghanian, and R. C. Mucic, "Ultraselective nanoparticle-based detection of PCR-amplified DNA," (1999), pp. COLL-038.
230. S.-J. Park, A. A. Lazarides, C. A. Mirkin, P. W. Brazis, C. R. Kannewurf, and R. L. Letsinger, "The electrical properties of gold nanoparticle assemblies linked by DNA," Angewandte Chemie, International Edition **39**, 3845-3848 (2000).
231. T. A. Taton, R. C. Mucic, C. A. Mirkin, and R. L. Letsinger, "The DNA-Mediated Formation of Supramolecular Mono- and Multilayered Nanoparticle Structures," Journal of the American Chemical Society **122**, 6305-6306 (2000).
232. J. J. Storhoff, A. A. Lazarides, R. C. Mucic, C. A. Mirkin, R. L. Letsinger, and G. C. Schatz, "What Controls the Optical Properties of DNA-Linked Gold Nanoparticle Assemblies?," Journal of the American Chemical Society **122**, 4640-4650 (2000).
233. B. Dubertret, M. Calame, and A. J. Libchaber, "Single-mismatch detection using gold-quenched fluorescent oligonucleotides," Nature Biotechnology **19**, 365-370 (2001).
234. Z. Li, R. Jin, C. A. Mirkin, and R. L. Letsinger, "Oligonucleotide-nanoparticle conjugates with multiple anchor groups," (2001), pp. COLL-191.
235. J.-M. Nam, S.-J. Park, and C. A. Mirkin, "Bio-barcodes based on oligonucleotide-modified nanoparticles," Journal of the American Chemical Society **124**, 3820-3821 (2002).
236. C. Sonnichsen, M. Reinhard Bjorn, J. Liphardt, and A. P. Alivisatos, "A molecular ruler based on plasmon coupling of single gold and silver nanoparticles," Nature biotechnology **23**, 741-745. (2005).
237. I. Stoeva Savka, F. Huo, J.-S. Lee, and A. Mirkin Chad, "Three-layer composite magnetic nanoparticle probes for DNA," Journal of the American Chemical Society **127**, 15362-15363. (2005).
238. J.-S. Lee, S. I. Stoeva, and C. A. Mirkin, "DNA-Induced Size-Selective Separation of Mixtures of Gold Nanoparticles," Journal of the American Chemical Society **128**, 8899-8903 (2006).
239. S. I. Stoeva, J.-S. Lee, C. S. Thaxton, and C. A. Mirkin, "Multiplexed DNA detection with biobarcoded nanoparticle probes," Angewandte Chemie, International Edition **45**, 3303-3306 (2006).
240. M. S. Han, A. K. R. Lytton-Jean, and C. A. Mirkin, "A Gold Nanoparticle Based Approach for Screening Triplex DNA Binders," Journal of the American Chemical Society **128**, 4954-4955 (2006).
241. C. S. Thaxton, D. G. Georganopoulou, and C. A. Mirkin, "Gold nanoparticle probes for the detection of nucleic acid targets," Clinica Chimica Acta **363**, 120-126 (2006).
242. L. R. Hirsch, R. J. Stafford, J. A. Bankson, S. R. Sershen, B. Rivera, R. E. Price, J. D. Hazle, N. J. Halas, and J. L. West, "Nanoshell-mediated near-infrared thermal therapy of tumors under magnetic resonance guidance," Proceedings of the National Academy of Sciences of the United States of America **100**, 13549-13554 (2003).
243. P. K. Jain, K. S. Lee, I. H. El-Sayed, and M. A. El-Sayed, "Calculated Absorption and Scattering Properties of Gold Nanoparticles of Different Size, Shape, and Composition: Applications in Biological Imaging and Biomedicine," Journal of Physical Chemistry B **110**, 7238-7248 (2006).
244. C. Loo, L. Hirsch, M.-H. Lee, E. Chang, J. West, N. Halas, and R. Drezek, "Gold nanoshell bioconjugates for molecular imaging in living cells," Optics Letters **30**, 1012-1014 (2005).

245. K. Sokolov, J. Aaron, B. Hsu, D. Nida, A. Gillenwater, M. Follen, C. MacAulay, K. Adler-Storthz, B. Korgel, M. Descour, R. Pasqualini, W. Arap, W. Lam, and R. Richards-Kortum, "Optical systems for in vivo molecular imaging of cancer," Technology in Cancer Research & Treatment **2**, 491-504 (2003).
246. T. Yoneda, M. M. Alsina, K. Watatani, F. Bellot, J. Schlessinger, and G. R. Mundy, "Dependence of a human squamous carcinoma and associated paraneoplastic syndromes on the epidermal growth factor receptor pathway in nude mice," Cancer Research **51**, 2438-2443 (1991).
247. D. M. Shin, J. Y. Ro, W. K. Hong, and W. N. Hittelman, "Dysregulation of epidermal growth factor receptor expression in premalignant lesions during head and neck tumorigenesis," Cancer research **54**, 3153-3159. (1994).
248. D. M. Shin, R. Perez-Soler, W. N. Hittelman, and W. K. Hong, "Epidermal growth factor receptor expression in head and neck tumorigenesis and saturation of EGFR with monoclonal antibody RG83852," Ernst Schering Research Foundation Workshop **19**, 65-87 (1997).
249. A. Kiyota, S. Shintani, M. Mihara, Y. Nakahara, Y. Ueyama, T. Matsumura, R. Todd, and D. T. W. Wong, "Expression of a truncated epidermal growth factor receptor in oral squamous cell carcinomas," Cancer Letters (Shannon, Ireland) **161**, 9-15 (2000).
250. N. S. Soukos, M. R. Hamblin, S. Keel, R. L. Fabian, T. F. Deutsch, and T. Hasan, "Epidermal growth factor receptor-targeted immunophotodiagnosis and photoimmunotherapy of oral precancer in vivo," Cancer Research **61**, 4490-4496 (2001).
251. M. Y. Khalil, J. R. Grandis, and D. M. Shin, "Targeting epidermal growth factor receptor: novel therapeutics in the management of cancer," Expert Review of Anticancer Therapy **3**, 367-380 (2003).
252. K. K. Ang, B. A. Berkey, X. Tu, H.-Z. Zhang, R. Katz, E. H. Hammond, K. K. Fu, and L. Milas, "Impact of epidermal growth factor receptor expression on survival and pattern of relapse in patients with advanced head and neck carcinoma," Cancer Research **62**, 7350-7356 (2002).
253. C. Xue, J. Wyckoff, F. Liang, M. Sidani, S. Violini, K.-L. Tsai, Z.-Y. Zhang, E. Sahai, J. Condeelis, and J. E. Segall, "Epidermal Growth Factor Receptor Overexpression Results in Increased Tumor Cell Motility In vivo Coordinately with Enhanced Intravasation and Metastasis," Cancer Research **66**, 192-197 (2006).
254. B. W. Ennis, E. M. Valverius, S. E. Bates, M. E. Lippman, F. Bellot, R. Kris, J. Schlessinger, H. Masui, A. Goldenberg, and et al., "Anti-epidermal growth factor receptor antibodies inhibit the autocrine-stimulated growth of MDA-468 human breast cancer cells," Molecular Endocrinology **3**, 1830-1838 (1989).
255. H. C. Gooi, E. F. Hounsell, I. Lax, R. M. Kris, T. A. Libermann, J. Schlessinger, J. D. Sato, T. Kawamoto, J. Mendelsohn, and T. Feizi, "The carbohydrate specificities of the monoclonal antibodies 29.1, 455 and 3C1B12 to the epidermal growth factor receptor of A431 cells," Bioscience Reports **5**, 83-94 (1985).
256. A. Ulman, "Formation and Structure of Self-Assembled Monolayers," Chemical Reviews (Washington, D. C.) **96**, 1533-1554 (1996).
257. J. I. Goldstein, D. E. Newbury, P. Echlin, D. C. Joy, A. D. Romig, C. E. Lyman, and E. L. C. Fiori, *Scanning Electron Microscopy and X-Ray Microanalysis* (Plenum, New York, NY, 1992).
258. P. M. Conn, and Editor, *Methods in Enzymology, Volume 307: Confocal Microscopy* (1999).
259. A. R. Hibbs, and Editor, *Confocal Microscopy for Biologists* (2004).
260. B. Matsumoto, *Cell Biological Applications of Confocal Microscopy, Second Edition* (2002).
261. T. Wilson, and C. Sheppard, "Theory and practive of scanning optical microscopy," Journal of the Optical Society of America A: Optics, Image Science, and Vision **4**, 551-560
(1987).
262. K. Travis, "Optical scattering from nanoparticle aggregates," in *Department of Physics*(University of Texas at Austin, Austin, 2004).
263. D. Garcia-Gutierrez, C. Gutierrez-Wing, M. Miki-Yoshida, and M. Jose-Yacaman, "HAADF study of Au-Pt core-shell bimetallic nanoparticles," Applied Physics A: Materials Science & Processing **79**, 481-487 (2004).
264. K. Aslan, J. R. Lakowicz, and C. D. Geddes, "Plasmon light scattering in biology and medicine: new sensing approaches, visions and perspectives," Current Opinion in Chemical Biology **9**, 538-544 (2005).
265. P. Alivisatos, "The use of nanocrystals in biological detection," Nature Biotechnology **22**, 47-52 (2004).
266. J. J. Storhoff, A. D. Lucas, V. Garimella, Y. P. Bao, and U. R. Mueller, "Homogeneous detection of unamplified genomic DNA sequences based on colorimetric scatter of gold nanoparticle probes," Nature Biotechnology **22**, 883-887 (2004).
267. V. P. Zharov, E. N. Galitovskaya, C. Johnson, and T. Kelly, "Synergistic enhancement of selective nanophotothermolysis with gold nanoclusters: Potential for cancer therapy," Lasers in surgery and medicine **37**, 219-226 (2005).

268. M. Mohammadi, A. Honegger, A. Sorokin, A. Ullrich, J. Schlessinger, and D. R. Hurwitz, "Aggregation-induced activation of the epidermal growth factor receptor protein tyrosine kinase," Biochemistry **32**, 8742-8748 (1993).
269. M. L. Sandrock, and C. A. Foss, Jr., "Synthesis and Linear Optical Properties of Nanoscopic Gold Particle Pair Structures," Journal of Physical Chemistry B **103**, 11398-11406 (1999).
270. M. Benveniste, J. Schlessinger, and Z. Kam, "Characterization of internalization and endosome formation of epidermal growth factor in transfected NIH-3T3 cells by computerized image-intensified three-dimensional fluorescence microscopy," Journal of Cell Biology **109**, 2105-2115 (1989).
271. H. Resat, J. A. Ewald, D. A. Dixon, and H. S. Wiley, "An integrated model of epidermal growth factor receptor trafficking and signal transduction," Biophysical Journal **85**, 730-743 (2003).
272. H. S. Wiley, "Trafficking of the ErbB receptors and its influence on signaling," Experimental Cell Research **284**, 78-88 (2003).
273. A. H. A. Clayton, F. Walker, S. G. Orchard, C. Henderson, D. Fuchs, J. Rothacker, E. C. Nice, and A. W. Burgess, "Ligand-induced Dimer-Tetramer Transition during the Activation of the Cell Surface Epidermal Growth Factor Receptor-A Multidimensional Microscopy Analysis," Journal of Biological Chemistry **280**, 30392-30399 (2005).
274. Y. H. Xu, N. Richert, S. Ito, G. T. Merlino, and I. Pastan, "Characterization of epidermal growth factor receptor gene expression in malignant and normal human cell lines.," Proceedings of the National Academy of Sciences of the United States of America **81**, 7308-7312. (1984).
275. W. E. Evans, and M. V. Relling, "Moving towards individualized medicine with pharmacogenomics," Nature **429**, 464-468 (2004).
276. S. Achilefu, "Lighting up tumors with receptor-specific optical molecular probes," Technology in Cancer Research & Treatment **3**, 393-409 (2004).
277. S. Kumar, K. Sokolov, and R. Richards-Kortum, "In-vivo optical detection of intracellular cancer biomarkers using gold nanoparticles," Proceedings of SPIE-The International Society for Optical Engineering **6095**, 609504/609501-609504/609510 (2006).
278. N. G. Portney, and M. Ozkan, "Nano-oncology: drug delivery, imaging, and sensing," Analytical and Bioanalytical Chemistry **384**, 620-630 (2006).
279. T. Liu, B. Liu, H. Zhang, and Y. Wang, "The fluorescence bioassay platforms on quantum dots nanoparticles," Journal of Fluorescence **15**, 729-733 (2005).
280. K. Sokolov, D. Nida, M. Descour, A. Lacy, M. Levy, B. Hall, S. Dharmawardhane, A. Ellington, B. Korgel, and R. Richards-Kortum, "Molecular optical imaging of therapeutic targets of cancer," Adv Cancer Res FIELD Full Journal Title:Advances in cancer research **96**, 299-344 (2007).
281. C. A. Mirkin, R. C. Mucic, J. J. Storhoff, and R. L. Letsinger, "DNA-induced assembly of gold nanoparticles: A method for rationally organizing colloidal particles into ordered macroscopic materials," (1996), pp. INOR-249.
282. W. D. Geoghegan, "The effect of three variables on adsorption of rabbit IgG to colloidal gold," Journal of Histochemistry and Cytochemistry **36**, 401-407 (1988).
283. W. M. Saltzman, M. R. Parkhurst, P. Parsons-Wingerter, and W. H. Zhu, "Three-dimensional cell cultures mimic tissues," (1992), pp. 259-273.
284. K. Sokolov, J. Galvan, A. Myakov, A. Lacy, R. Lotan, and R. Richards-Kortum, "Realistic three-dimensional epithelial tissue phantoms for biomedical optics," Journal of biomedical optics **7**, 148-156. (2002).
285. L. B. Lachman, X.-M. Rao, R. H. Kremer, B. Ozpolat, G. Kiriakova, and J. E. Price, "DNA vaccination against neu reduces breast cancer incidence and metastasis in mice," Cancer Gene Therapy **8**, 259-268 (2001).
286. D. M. Shin, I. B. Gimenez, J. S. Lee, K. Nishioka, M. J. Wargovich, S. Thacher, R. Lotan, T. J. Slaga, and W. K. Hong, "Expression of epidermal growth factor receptor, polyamine levels, ornithine decarboxylase activity, micronuclei, and transglutaminase I in a 7,12-diemthylbenz(a)anthracene-induced hamster buccal pouch carcinogenesis model," Cancer Research **50**, 2505-2510 (1990).
287. J. R. Dell, and C. L. Parsons, "Multimodal therapy for interstitial cystitis," Journal of Reproductive Medicine **49**, 243-252 (2004).
288. A. P. Kyriazis, L. DiPersio, G. J. Michael, A. J. Pesce, and J. D. Stinnett, "Growth Patterns and Metastatic Behavior of Human Tumors Growing in Athymic Mice," (1978), pp. 3186-3190.
289. H. Shiozaki, H. Oka, I. M., S. Tamura, and M. Monden, "E-cadherin mediated adhesion system in cancer cells.," Cancer **77**, 1605-1613 (1996).

290. A. Ferrari, F. Rovera, P. Dionigi, G. Limonta, M. Marelli, I. Besana Ciani, V. Bianchi, C. Vanoli, and R. Dionigi, "Sentinel lymph node biopsy as the new standard of care in the surgical treatment for breast cancer," Expert Rev Anticancer Ther FIELD Full Journal Title:Expert review of anticancer therapy **6**, 1503-1515. (2006).
291. J. Liptay Michael, "Sentinel lymph node mapping in lung cancer," Cancer Treat Res FIELD Full Journal Title:Cancer treatment and research **127**, 141-150. (2005).
292. A. Eicher Susan, L. Clayman Gary, N. Myers Jeffrey, and M. Gillenwater Ann, "A prospective study of intraoperative lymphatic mapping for head and neck cutaneous melanoma," Arch Otolaryngol Head Neck Surg FIELD Full Journal Title:Archives of otolaryngology--head & neck surgery **128**, 241-246. (2002).
293. V. S. Talanov, C. A. S. Regino, H. Kobayashi, M. Bernardo, P. L. Choyke, and M. W. Brechbiel, "Dendrimer-Based Nanoprobe for Dual Modality Magnetic Resonance and Fluorescence Imaging," Nano Letters **6**, 1459-1463 (2006).
294. G. Soltesz Edward, S. Kim, S.-W. Kim, G. Laurence Rita, M. De Grand Alec, P. Parungo Cherie, H. Cohn Lawrence, G. Bawendi Mounqi, and V. Frangioni John, "Sentinel lymph node mapping of the gastrointestinal tract by using invisible light," Ann Surg Oncol FIELD Full Journal Title:Annals of surgical oncology : the official journal of the Society of Surgical Oncology **13**, 386-396. (2006).
295. S. Kim, Y. T. Lim, E. G. Soltesz, A. M. De Grand, J. Lee, A. Nakayama, J. A. Parker, T. Mihaljevic, R. G. Laurence, D. M. Dor, L. H. Cohn, M. G. Bawendi, and J. V. Frangioni, "Near-infrared fluorescent type II quantum dots for sentinel lymph node mapping," Nature Biotechnology **22**, 93-97 (2004).
296. J. Hihara, H. Ueno, and T. Toge, "A new tracer for sentinel node detection in esophageal and lung cancer--fluorescent microspheres," Nippon Geka Gakkai Zasshi FIELD Full Journal Title:Nippon Geka Gakkai zasshi **104**, 762-764. (2003).
297. H. Gray, *Anatomy of the human body* (Lea & Febiger, Philadelphia, 1918).
298. N. S. Soukos, M. R. Hamblin, T. F. Deutsch, and T. Hasan, "Monoclonal antibody-tagged receptor-targeted contrast agents for detection of cancers," Proceedings of SPIE-The International Society for Optical Engineering **4259**, 115-128 (2001).
299. L. M. Grovdal, E. Stang, A. Sorkin, and I. H. Madshus, "Direct interaction of Cbl with pTyr 1045 of the EGF receptor (EGFR) is required to sort the EGFR to lysosomes for degradation," Experimental Cell Research **300**, 388-395 (2004).
300. K. Roy, H. Q. Mao, S. K. Huang, and K. W. Leong, "Oral gene delivery with chitosan--DNA nanoparticles generates immunologic protection in a murine model of peanut allergy," Nature medicine **5**, 387-391. (1999).
301. S. D. Larson, C. G. Plopper, G. Baker, B. K. Tarkington, K. C. Decile, K. Pinkerton, J. K. Mansoor, D. M. Hyde, and E. S. Schelegle, "Proximal airway mucous cells of ovalbumin-sensitized and -challenged Brown Norway rats accumulate the neuropeptide calcitonin gene-related peptide," American Journal of Physiology **287**, L286-L295 (2004).
302. W. A. See, and Q. Xia, "Regional chemotherapy for bladder neoplasms using continuous intravesical infusion of doxorubicin: impact of concomitant administration of dimethyl sulfoxide on drug absorption and antitumor activity," Journal of the National Cancer Institute **84**, 510-515 (1992).
303. F. S. De Rosa, J. M. Marchetti, J. A. Thomazini, A. C. Tedesco, and M. V. L. B. Bentley, "A vehicle for photodynamic therapy of skin cancer: influence of dimethylsulfoxide on 5-aminolevulinic acid in vitro cutaneous permeation and in vivo protoporphyrin IX accumulation determined by confocal microscopy," Journal of Controlled Release **65**, 359-366 (2000).
304. D. Sharma, T. P. Chelvi, J. Kaur, K. Chakravorty, T. K. De, A. Maitra, and R. Ralhan, "Novel Taxol formulation: polyvinylpyrrolidone nanoparticle-encapsulated Taxol for drug delivery in cancer therapy," Oncology Research **8**, 281-286 (1996).
305. N. S. Templeton, D. D. Lasic, P. M. Frederik, H. H. Strey, D. D. Roberts, and G. N. Pavlakis, "Improved DNA: liposome complexes for increased systemic delivery and gene expression," Nature Biotechnology **15**, 647-652 (1997).
306. S. V. Kershaw, M. Burt, M. Harrison, A. Rogach, H. Weller, and A. Eychmuller, "Colloidal CdTe/HgTe quantum dots with high photoluminescence quantum efficiency at room temperature," Applied Physics Letters **75**, 1694-1696 (1999).
307. C. F. Meares, A. J. Chmura, M. S. Orton, T. M. Corneillie, and P. A. Whetstone, "Molecular tools for targeted imaging and therapy of cancer," Journal of Molecular Recognition **16**, 255-259 (2003).
308. R. Pasqualini, and E. Ruoslahti, "Organ targeting in vivo using phage display peptide libraries," Nature (London) **380**, 364-366 (1996).

309. P. K. Aravind, A. Nitzan, and H. Metiu, "The interaction between electromagnetic resonances and its role in spectroscopic studies of molecules adsorbed on colloidal particles or metal spheres," Surface Science **110**, 189-204 (1981).
310. R. Elghanian, J. J. Storhoff, R. C. Mucic, R. L. Letsinger, and C. A. Mirkin, "Selective colorimetric detection of polynucleotides based on the distance-dependent optical properties of gold nanoparticles," Science **277**, 1078-1080 (1997).
311. J. J. Storhoff, A. D. Lucas, V. Garimella, P. Y. Bao, and U. R. Mueller, "Homogeneous detection of unamplified genomic DNA sequences based on colorimetric scatter of gold nanoparticle probes," Nature Biotech. **22**, 883-887 (2004).
312. L. Oldenburg Amy, R. Gunther Jillian, and A. Boppart Stephen, "Imaging magnetically labeled cells with magnetomotive optical coherence tomography," Optics letters **30**, 747-749. (2005).
313. J. N. Anker, and R. Kopelman, "Magnetically modulated optical nanoprobes," Applied Physics Letters **82**, 1102-1104 (2003).
314. J. Oh, M. Feldman, J. Kim, C. Condit, S. Emelianov, and T. E. Milner, "Detection of magnetic nanoparticles in tissue using magneto-motive ultrasound " Nanotechnology **17**, 8 (2006).
315. J. Lin, W. Zhou, A. Kumbhar, J. Wiemann, J. Fang, E. E. Carpenter, and C. J. O'Connor, "Gold-Coated Iron (Fe@Au) Nanoparticles: Synthesis, Characterization, and Magnetic Field-Induced Self-Assembly," Journal of Solid State Chemistry **159**, 26-31 (2001).
316. S.-J. Cho, B. R. Jarrett, A. Y. Louie, and S. M. Kauzlarich, "Gold-coated iron nanoparticles: a novel magnetic resonance agent for T1 and T2 weighted imaging," Nanotechnology **17**, 640-644 (2006).
317. S.-J. Cho, A. M. Shahin, G. J. Long, J. E. Davies, K. Liu, F. Grandjean, and S. M. Kauzlarich, "Magnetic and Moessbauer Spectral Study of Core/Shell Structured Fe/Au Nanoparticles," Chemistry of Materials **18**, 960-967 (2006).
318. S. I. Stoeva, F. Huo, J.-S. Lee, and C. A. Mirkin, "Three-Layer Composite Magnetic Nanoparticle Probes for DNA," Journal of the American Chemical Society **127**, 15362-15363 (2005).
319. H. Wang, D. W. Brandl, F. Le, P. Nordlander, and N. J. Halas, "Nanorice: A Hybrid Plasmonic Nanostructure," Nano Letters **6**, 827-832 (2006).
320. K. R. Brown, and M. J. Natan, "Hydroxylamine Seeding of Colloidal Au Nanoparticles in Solution and on Surfaces," Langmuir **14**, 726-728 (1998).
321. J. Jeong, T. H. Ha, and B. H. Chung, "Enhanced reusability of hexa-arginine-tagged esterase immobilized on gold-coated magnetic nanoparticles," Analytica Chimica Acta **569**, 203-209 (2006).
322. L. Liu, and H. Elwing, "Complement activation on thiol-modified gold surfaces," Journal of Biomedical Materials Research **30**, 535-541 (1996).
323. A. L. Aden, and M. Kerker, "Scattering of Electromagnetic Waves from Two Concentric Spheres," Journal of Applied Physics **22**, 1242-1246 (1951).
324. P. B. Johnson, and R. W. Christy, "Optical constants of the noble metals," Physical Review B: Solid State **6**, 4370-4379 (1972).
325. U. Kreibig, "Properties of Small Particles in Insulating Matrices," in *Contribution of Clusters Physics to Material Science and Technology From Isolated Clusters to Aggregated Materials*, J. Davenas, and P. M. Rabette, eds. (Klewer Academic Publishers, New York, NY, 1986), pp. 373-423.
326. V. Backman, V. Gopal, M. Kalashnikov, K. Badizadegan, R. Gurjar, A. Wax, I. Georgakoudi, M. Mueller, C. W. Boone, R. R. Dasari, and M. S. Feld, "Measuring cellular structure at submicrometer scale with light scattering spectroscopy," IEEE Journal of Selected Topics in Quantum Electronics **7**, 887-893 (2001).
327. F. J. Harris, "On the Use of Windows for Harmonic Analysis with the Discrete Fourier Transform," Proceedings of the IEEE **66**, 33 (1978).
328. T. R. Strick, J. F. Allemand, D. Bensimon, A. Bensimon, and V. Croquette, "The elasticity of a single supercoiled DNA molecule," Science (Washington, D. C.) **271**, 1835-1837 (1996).
329. C. Wilhelm, F. Gazeau, and J. C. Bacri, "Rotational magnetic endosome microrheology: Viscoelastic architecture inside living cells," Physical Review E: Statistical, Nonlinear, and Soft Matter Physics **67**, 061908/061901-061908/061912 (2003).
330. H. Huang, J. Sylvan, M. Jonas, R. Barresi, P. T. C. So, K. P. Campbell, and R. T. Lee, "Cell stiffness and receptors: Evidence for cytoskeletal subnetworks," American Journal of Physiology **288**, C72-C80 (2005).
331. J. P. Dawson, M. B. Berger, C.-C. Lin, J. Schlessinger, M. A. Lemmon, and K. M. Ferguson, "Epidermal growth factor receptor dimerization and activation require ligand-induced conformational changes in the dimer interface," Molecular and Cellular Biology **25**, 7734-7742 (2005).

332. A. Boppart Stephen, L. Oldenburg Amy, C. Xu, and L. Marks Daniel, "Optical probes and techniques for molecular contrast enhancement in coherence imaging," Journal of biomedical optics **10**, 41208. (2005).
333. T. C. Doyle, S. M. Burns, and C. H. Contag, "In vivo bioluminescence imaging for integrated studies of infection," Cellular Microbiology **6**, 303-317 (2004).
334. Y. Liu, K. Chen, Y. L. Kim, G. Ameer, and V. Backman, "Multilayer resonant light scattering nanoshells as a novel class of nonbleaching labels for multimarker molecular imaging," Proceedings of SPIE-The International Society for Optical Engineering **5326**, 73-81 (2004).
335. A. L. Oldenburg, M. N. Hansen, D. A. Zweifel, A. Wei, and S. A. Boppart, "Plasmon-resonant gold nanorods as low backscattering albedo contrast agents for optical coherence tomography," Optics Express **14**, 6724-6738 (2006).
336. J. S. Aaron, J. Oh, T. A. Larson, S. Kumar, T. E. Milner, and K. V. Sokolov, "Increased optical contrast in imaging of epidermal growth factor receptor using magnetically actuated hybrid gold/iron oxide nanoparticles," Optics Express **14**, 12930-12943 (2006).

VITA

Jesse Aaron was born in Albuquerque, New Mexico on June 16, 1979 to Robert and Elaine Aaron. After graduating from La Cueva High School in May of 1997, Jesse enrolled in the Department of Chemical Engineering at the University of Texas at Austin the following fall. During this time, Jesse also undertook various research internships at the University, as well as at Sandia National Laboratories and the Southwest Research Institute in San Antonio, TX. He completed his B.S. degree in Chemical Engineering in 2001, and in 2003, again enrolled at the University of Texas at Austin as a graduate student in the newly formed Department of Biomedical Engineering under his supervisors Drs. Konstantin Sokolov and Rebecca Richards-Kortum.

Permanent Address: 12000B Commonwealth Way; Austin, TX 78759

This dissertation was typed by the author.